







A Zn-dependent structural transition of SOD1 modulates its ability to undergo phase separation

Bidisha Das^{1,2,†} , Sumangal Roychowdhury^{1,†} , Priyesh Mohanty³ , Azamat Rizuan³ , Joy Chakraborty⁴, Jeetain Mittal^{3,*}  & Krishnananda Chattopadhyay^{1,2,**} 

Abstract

The misfolding and mutation of Cu/Zn superoxide dismutase (SOD1) is commonly associated with amyotrophic lateral sclerosis (ALS). SOD1 can accumulate within stress granules (SGs), a type of membraneless organelle, which is believed to form via liquid–liquid phase separation (LLPS). Using wild-type, metal-deficient, and different ALS disease mutants of SOD1 and computer simulations, we report here that the absence of Zn leads to structural disorder within two loop regions of SOD1, triggering SOD1 LLPS and amyloid formation. The addition of exogenous Zn to either metal-free SOD1 or to the severe ALS mutation I113T leads to the stabilization of the loops and impairs SOD1 LLPS and aggregation. Moreover, partial Zn-mediated inhibition of LLPS was observed for another severe ALS mutant, G85R, which shows perturbed Zn-binding. By contrast, the ALS mutant G37R, which shows reduced Cu-binding, does not undergo LLPS. In addition, SOD1 condensates induced by Zn-depletion exhibit greater cellular toxicity than aggregates formed by prolonged incubation under aggregating conditions. Overall, our work establishes a role for Zn-dependent modulation of SOD1 conformation and LLPS properties that may contribute to amyloid formation.

Keywords aggregation; amyotrophic lateral sclerosis (ALS); liquid–liquid phase separation (LLPS); molecular dynamics (MD) simulation; SOD1

Subject Categories Neuroscience; Organelles

DOI 10.15252/embj.2022111185 | Received 16 March 2022 | Revised 26 October 2022 | Accepted 31 October 2022 | Published online 23 November 2022

The EMBO Journal (2023) 42: e111185

Introduction

Amyotrophic lateral sclerosis (ALS) is an adult-onset progressive neurodegenerative disease that affects motor neurons of the brain and spinal cord, resulting in loss of control over voluntary muscle, paralysis, and death, often by respiratory failure (Rowland &

Shneider, 2001). About 8–10% of ALS cases are familial (fALS; Rosen *et al*, 1993), while the rest occur sporadically (sALS). There are more than 140 point mutations of human Cu/Zn superoxide dismutase (SOD1), which are associated with fALS (Andersen, 2006). Cu/Zn SOD1 is a highly conserved 153 amino acids (aa) long metalloenzyme, encoded by the SOD1 gene located on chromosome 21 (Rosen *et al*, 1993). It is the primary scavenger of reactive oxygen species, catalyzing the conversion of superoxide radicals to hydrogen peroxide and water in a two-step reaction.

Each SOD1 monomer consists of eight anti-parallel β strands arranged in a β -barrel structure. Extensive structural and biophysical experiments (Furukawa *et al*, 2016) have previously established that the immature, monomeric state of SOD1 contains two disordered regions (Fig 1A–C, Appendix Fig S1A–C). The first region corresponds to loop IV (aa:49–83) and is also referred to as the “Zn-binding” loop. The second region corresponds to loop VII (aa:121–142) and is commonly referred to as the “electrostatic loop”. SOD1 matures through three sequential steps, namely zinc (Zn) binding, copper (Cu) insertion via Cu chaperone protein (CCS), and disulfide bond formation (Culotta *et al*, 1997; Furukawa *et al*, 2004; Zittin Potter *et al*, 2007). While Cu is responsible for the activity of the enzyme, Zn binding to loop IV decreases the disorder by guarding the electrostatic loop and structuring the Cu insertion site (Furukawa *et al*, 2016). In the early steps of SOD1 maturation and its intracellular transport to mitochondrial inter-membrane space, the protein in its monomeric metal-free state is highly disordered in solution, and prone to misfolding and subsequent aggregation (Mojumdar *et al*, 2017).

The assembly and aggregation of SOD1 ALS mutants have been shown in cytosolic SGs (Mateju *et al*, 2017; Ros *et al*, 2020; Samanta *et al*, 2021). SGs are membraneless organelles composed of proteins and nucleic acids, possessing liquid-like properties (Boundedjah *et al*, 2012). They originate as a response to intracellular stress through a process called liquid–liquid phase separation (LLPS; Hyman & Simons, 2012; Brangwynne, 2013; Hyman *et al*, 2014; Brangwynne *et al*, 2015; Boeynaems *et al*, 2018; Dignon *et al*, 2020; Mohanty *et al*, 2022) and may revert to their nondroplet state once

1 Structural Biology and Bioinformatics Division, CSIR-Indian Institute of Chemical Biology, Kolkata, India

2 Academy of Scientific and Innovative Research (AcSIR), Ghaziabad, India

3 Artie McFerrin Department of Chemical Engineering, Texas A&M University, College Station, TX, USA

4 Cell Biology and Physiology Division, CSIR-Indian Institute of Chemical Biology, Kolkata, India

*Corresponding author. Tel: +1 (979) 862 1920; E-mail: jeetain@tamu.edu

**Corresponding author. Tel: +91 33 24995843; E-mail: krishn@iicb.res.in

†These authors contributed equally to this work as co-first authors

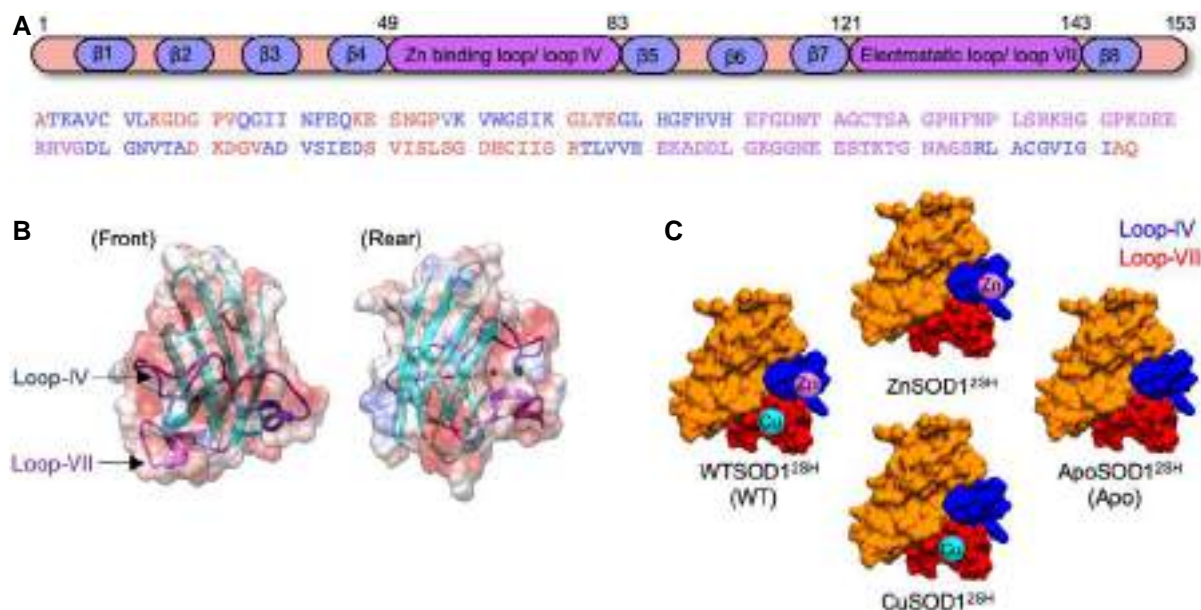


Figure 1. The structure of SOD1.

- A Human SOD1 amino acid sequence comprised 8-beta sheets (highlighted in blue) connected by seven loop regions (in red); Zn-binding loop IV and electrostatic loop VII highlighted in purple.
- B Cartoon representation of SOD1 monomer highlighting loops IV and VII (Coulombic surface coloring: red = negative, white = neutral, blue = positive).
- C Schematic representation of SOD1 variants used in the study. WTSOD1^{2SH} is the disulfide-reduced holo form with both metal ion cofactors Zn and Cu. ApoSOD1^{2SH} is the disulfide-reduced de-metalated form of WTSOD1^{2SH} lacking both metal cofactors. ZnSOD1^{2SH} and CuSOD1^{2SH} are the only Zn- and Cu-bound forms of the disulfide-reduced monomer.

the stress is dissipated. The presence of SGs comprising of SOD1, TAR DNA-binding protein 43 (TDP-43), and FUS forms the central pathogenic hallmark of ALS (Pokrishevsky *et al*, 2012; Farrarwell *et al*, 2015; Kang *et al*, 2018). Previous studies have demonstrated the phase separation of other intrinsically disordered proteins (IDPs) involved in the formation of SGs like FUS and TDP-43. It is hence important to investigate whether SOD1, which is also a component of SGs, would phase separate under suitable conditions. It may also be noted that while a recent study reports that Zn promotes LLPS of tau protein (Singh *et al*, 2020), the phase behavior of metal-containing proteins has been relatively unexplored.

In this study, we observed that disulfide-reduced, metal-free SOD1 (ApoSOD1^{2SH}) forms liquid droplets, which can be reversed by Zn addition, whereas the fully metalated WT protein (WTSOD1^{2SH}) does not undergo LLPS (Fig 2A). We then show that two severe ALS mutants, namely I113T SOD1^{2SH} and G85R SOD1^{2SH} with a low affinity towards Zn, also undergo LLPS, while another mutant G37R SOD1^{2SH} (with less disease severity and strong binding to Zn) does not. For ApoSOD1^{2SH}, I113T SOD1^{2SH}, and G85R SOD1^{2SH} variants, LLPS is followed by aggregation—although, unlike the liquid droplets, the aggregated state could not be reversed by the addition of Zn. Interestingly, Cu, which is primarily responsible for dismutase activity, does not have any effect on LLPS and/or aggregation. Using Fluorescence Correlation Spectroscopy (FCS) and Fourier-transform infrared spectroscopy (FTIR), we find that the LLPS and subsequent aggregation are regulated by the conformational transition between a disordered and a relatively compact folded state. The extent of intrinsic disorder in various SOD1

monomeric states was further characterized using all-atom molecular dynamics (AAMD) simulations. In addition, coarse-grained (CG), phase coexistence simulations were used to characterize the role of loop-IV/VII regions in stabilizing the condensed phase of ApoSOD1^{2SH}. Using multiple toxicity and flow cytometric assays, we showed that the condensates promoted greater cytotoxicity than aggregates. Overall, the cofactor Zn, by virtue of its efficient shielding (Rotunno & Bosco, 2013) of loops IV and VII, acts as a switch to control conformational disorder and the phase separation propensity of SOD1.

Results

SOD1 is different from other SG proteins that are implicated in ALS such as FUS and TDP-43 as it lacks long intrinsically disordered regions (IDRs), which are known to drive the LLPS. It is also much smaller (153 aa) than these other proteins (FUS: 526 aa, TDP-43: 414 aa) thereby reducing its ability to form comparable, multivalent interactions. As SOD1 has been found to be associated with SGs in ALS pathology, it is important to determine whether it can undergo LLPS without the presence of other SG proteins. To answer this question, we conducted several biophysical measurements to check whether the SOD1 phase separates *in vitro*. All experiments mentioned in this paper were carried out using reduced monomeric protein variants using 20 mM HEPES buffer, pH 7.4 in presence of 100 mM NaCl, and temperature 37°C, unless explicitly noted otherwise.

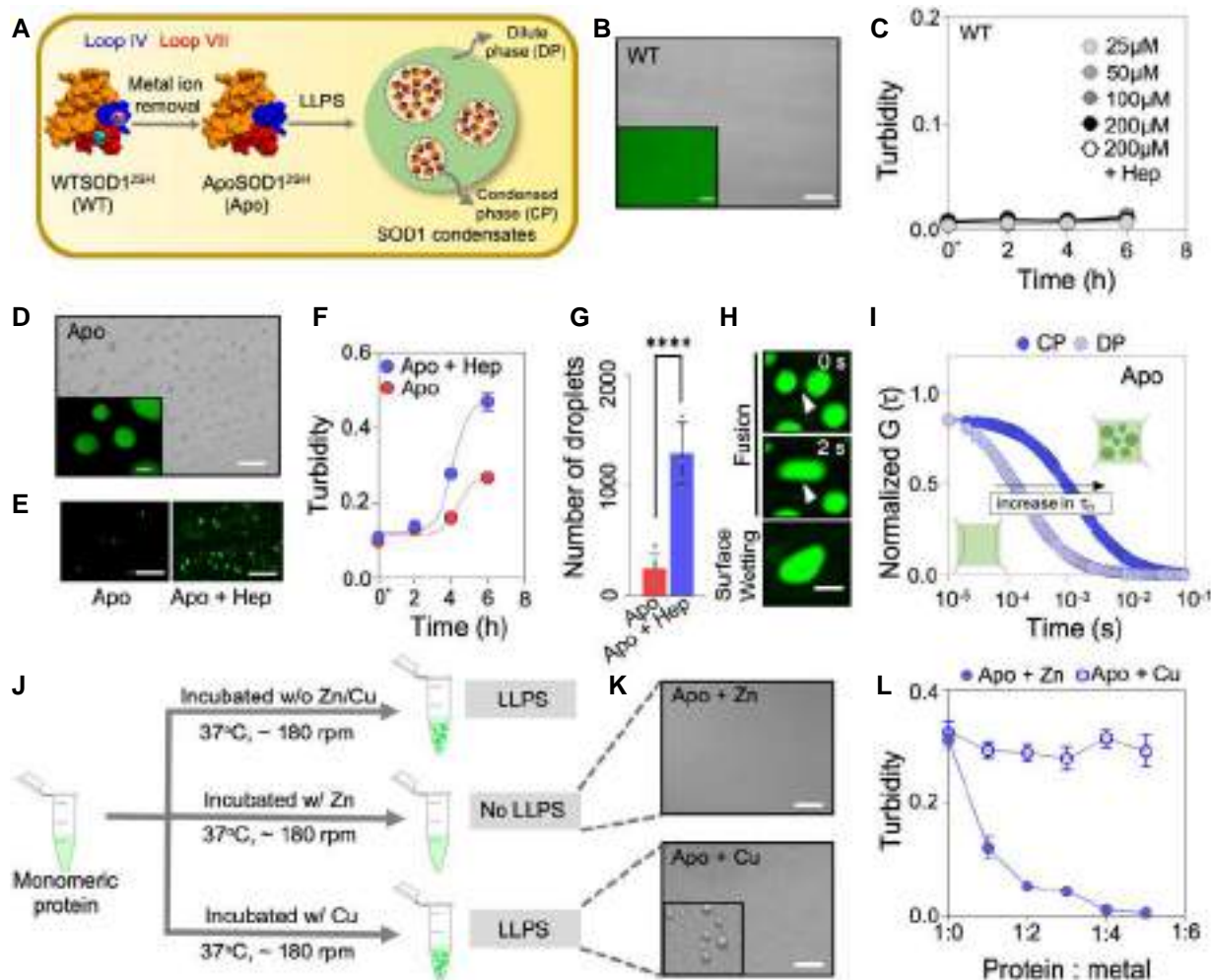


Figure 2. ApoSOD1^{2SH} undergoes liquid-liquid phase separation.

- A SOD1^{2SH} undergoes LLPS on the removal of metal ion cofactors.
- B DIC microscopic image of WT SOD1^{2SH} diluted to 100 μ M in HEPES buffer, pH 7.4 and 100 mM NaCl, and incubated 37°C, 180 RPM for 30 min shows no droplet formation; scale bar: 100 μ m; inset shows Alexa Fluor 488 maleimide-labeled WT SOD1^{2SH}; scale bar: 5 μ m.
- C Solution turbidity plot (absorbance at 600 nm) shows that WT SOD1^{2SH} (at concentrations ranging from 25 to 200 μ M) does not undergo LLPS in the presence or absence of heparin, LLPS inducer; data are represented as mean \pm SD (from three biological replicates).
- D DIC microscopic image of Apo SOD1^{2SH} under condensate inducing conditions (37°C, 180 RPM) at a concentration of 100 μ M incubated 100 mM NaCl; scale bar: 100 μ m (inset on bottom left shows Alexa Fluor 488 maleimide-labeled protein condensates; scale bar: 5 μ m).
- E Fluorescent microscopic images of Alexa Fluor 488 maleimide-labeled Apo SOD1^{2SH} condensates diluted in HEPES buffer, pH 7.4 and 100 mM NaCl and incubated (180 RPM, 37°C) in the absence (left) and presence (right) of heparin at 30 min time point; scale bar: 100 μ m.
- F Solution turbidity measurements with Apo SOD1^{2SH} (absorbance at 600 nm) show that while in the absence of heparin the turbidity increases with time, the presence of heparin results in faster LLPS; data are represented as mean \pm SD (from three biological replicates).
- G Comparison of Apo SOD1^{2SH} droplet numbers per microscopic field of view (view area 0.001963 mm²) calculated from five different images of droplets incubated with and without heparin at 2 h time point. Data are represented as mean \pm SD. Statistical significance was established using an unpaired nonparametric t-test (**** $p < 0.0001$).
- H Liquid nature of Apo SOD1^{2SH} showing droplet fusion and surface wetting; scale bar: 5 μ m.
- I Amplitude normalized FCS curves of Apo SOD1^{2SH} (in blue) of dilute phase (DP) and condensed phase (CP). Intense color indicates CP and light variant indicates DP. The increase in τ_D (as shown by the arrow) translates to a decrease in $\langle D \rangle$; please refer to equation (2) in Materials and Methods section).
- J Scheme depicting that presence of Zn and not Cu in a preincubation mixture inhibits LLPS.
- K DIC microscopic images of Apo SOD1^{2SH} in presence of Zn (top) showing no droplet formation and Cu (below) showing the presence of droplets; scale bar: 100 μ m.
- L Solution turbidity plot (absorbance at 600 nm) of Apo SOD1^{2SH} subjected to increasing concentrations of Cu and Zn; turbidity decreases in a dose-dependent manner for Zn while no significant change is observed in presence of Cu; data are represented as mean \pm SD (from three biological replicates).

Source data are available online for this figure.

ApoSOD1^{2SH} undergoes liquid–liquid phase separation

Using phase contrast microscopy (Fig 2B and C, Appendix Fig S2A), we did not observe the formation of condensates for different concentrations (25, 50, 100, and 200 μ M) of WTSOD1^{2SH}. We then used three co-solvents: a neutral molecular crowder polyethylene glycol 8000 (PEG), a positively charged polymer (polyethylenimine, PEI), and a negatively charged polysaccharide (heparin) to check whether these could induce the formation of WTSOD1^{2SH} condensates. Neutral crowders like PEG have been found to facilitate condensate formation for other proteins, presumably by increasing their local concentrations (Annunziata *et al*, 2002; Wegmann *et al*, 2018; Park *et al*, 2020). The idea of PEI has originated from the fact that SOD1 has a net negative charge, and hence the use of cationic PEI (Pullara *et al*, 2022) would facilitate LLPS in SOD1. By contrast, heparin—a polyanionic glycosaminoglycan known to be an aggregation-inducing agent (Vilasi *et al*, 2011; Maïza *et al*, 2018), has also been shown to drive the phase separation of low complexity regions (LCRs) or IDRs like Tau (Ambadipudi *et al*, 2017), C-terminal low complexity domain of TDP43 (Babinchak *et al*, 2020) and SH₃-PRM₅ (Ghosh *et al*, 2019). Notably, we did not observe any condensate formation for WTSOD1^{2SH} in the presence of different concentrations of any of these above crowding agents (Appendix Fig S2B–D).

Since immature SOD1^{2SH} exhibits a conformational disorder that is known to promote LLPS, we next chose the metal-free Apo variant (ApoSOD1^{2SH}) for further investigation (See Materials and Methods). Interestingly, ApoSOD1^{2SH} formed spherical droplets in HEPES buffer at 37°C at concentrations greater than 2 μ M (Fig 2D). Fluorescence imaging of Alexa-488 Maleimide-labeled protein (15 nM-labeled protein in the presence of 100 μ M of unlabelled protein) showed that the protein molecules were distributed throughout the liquid droplets (Fig 2D inset). While ApoSOD1^{2SH} formed droplets in the absence of co-solvents (heparin, PEG8000, and PEI as mentioned above), the process was accelerated in the presence of all three (Fig 2E–G, Appendix Fig S2E–G). We used 7% heparin for all our studies described henceforth. With time, the droplets in proximity underwent fusion events forming larger droplets and surface wetting that could be monitored using fluorescence microscopy, exhibiting the liquid-like nature of these SOD1 condensates (Fig 2H), like other proteins undergoing LLPS (Molliex *et al*, 2015; Kanaan *et al*, 2020; Ray *et al*, 2020; Bhandari *et al*, 2021; Krainer *et al*, 2021; Siegert *et al*, 2021).

Next, we used Fluorescence Correlation Spectroscopy (FCS) to monitor the change in the diffusional dynamics of protein variants outside (dilute phase) and inside (condensed phase) droplets. FCS probes the fluctuations in fluorescence intensity arising out of the diffusion of labeled protein molecules inside an approximate femto-liter confocal volume. Analyses of the correlation functions using a suitable model provide information about the diffusion coefficient (D) of the molecule. The advantage of FCS comes from its application to probe a selected region inside a microscopic image, and its ability to provide single-molecule resolution using diffusing molecules. From the value of the diffusion coefficient (D), we calculated the hydrodynamic radius (r_H) of ApoSOD1^{2SH} outside the droplet to be around 2.80 nm, which is consistent with earlier reports (Vassall *et al*, 2011; Bunck *et al*, 2018). Inside the droplets, we observed a large (~2.5 fold) reduction in the value of D (and reduced mobility; Fig 2I). Interestingly, between the outside and inside droplets, we

also observed a large (17-fold) increase in the value of rotational correlation times (Appendix Fig S2H), which we measured by time-resolved anisotropy measurements using time-domain fluorescence lifetime imaging microscopy (TD-FLIM). The restricted environment inside the droplet likely causes a decrease in rotational and translational motion of the protein molecules inside the droplets. It may be noted that a large decrease in D for the condensed phase compared with the dilute phase has been previously observed for different proteins including FUS (Murthy *et al*, 2019), TDP-43 (Conicella *et al*, 2020), and Tau (Boyko *et al*, 2019). In addition, we measured the fluorescence lifetime values of the attached dye (Alexa 488 Maleimide) to probe its excited state properties, which increased from the dilute phase to the condensed phase (Appendix Fig S2I–K). Droplet formation was also found to be salt-dependent as increasing salt concentration (from 100 to 600 μ M) gives rise to larger droplets (Appendix Fig S2L and M). In addition, when the condensates were subjected to 1,6-hexanediol treatment, an aliphatic alcohol that has been proposed to disrupt weak hydrophobic interactions (Kroschwald *et al*, 2017), there was a significant reduction in the number of droplets (Appendix Fig S2N and O). These results highlight the importance of weak hydrophobic interactions in stabilizing the ApoSOD1^{2SH} protein condensates.

Studies with ApoSOD1^{2SH} and ALS mutants suggest that the cofactor Zn modulates LLPS

Since WTSOD1^{2SH} does not form condensates, while the metal-free ApoSOD1^{2SH} forms these readily, it is apparent that the metal cofactors may have a role to play in condensate formation. Since SOD1 contains two metals (Cu and Zn) as cofactors, we then wanted to test the effect of the exogenous addition of each of these on the LLPS propensity of ApoSOD1^{2SH}. We added Cu and Zn, respectively, to 100 μ M protein solutions, which were then incubated for LLPS (preincubation condition, Fig 2J). We found that the addition of Zn at the time of incubation inhibited LLPS formation, while exogenous Cu addition did not have any effect on the condensed phase of ApoSOD1^{2SH} (Fig 2J–L). We then added Zn to preformed condensates of ApoSOD1^{2SH} (postincubation condition) to check whether Zn could dissolve them (Appendix Fig S2P). The addition of Zn to preformed condensates was observed to dissolve them immediately. This experiment shows that LLPS of ApoSOD1^{2SH} is reversible through Zn binding and that metal coordination can either inhibit (preincubation condition) or disrupt (postincubation) condensates.

After establishing that Zn has a major role in modulating the LLPS of ApoSOD1^{2SH}, we selected three ALS-associated disease mutants for further studies. Two of these mutants, I113T SOD1^{2SH} and G85R SOD1^{2SH} are known to have compromised Zn binding in their native conditions (Hayward *et al*, 2002; Cao *et al*, 2008). The inefficiency in Zn binding for I113T SOD1^{2SH} has been attributed to the mutational stress introduced at the dimeric surface of the protein (Hennig *et al*, 2015). In G85R SOD1^{2SH}, the loss of Zn binding is likely due to the proximity of the mutation site to the Zn-binding domain (residue 63–83). G85R SOD1^{2SH} was found to bind ~5% Zn relative to WTSOD1^{2SH} when expressed with the same metal ion supplementation (Hayward *et al*, 2002). In the third ALS mutant, G37R SOD1^{2SH} the mutation site is comparatively distant from the Zn-binding site (23.7 Å). Although it has an intact Zn-binding site, G37R SOD1^{2SH} shows Cu deficiency (Tokuda *et al*, 2018). We have

shown previously that G37R SOD1^{2SH} and I113T SOD1^{2SH} behave similarly to the WTSOD1^{2SH} and ApoSOD1^{2SH}, respectively, in terms of their membrane binding and aggregation propensity (Sannigrahi *et al.*, 2021). In addition, the G37RS OD1^{2SH} mutant possesses a less severe disease phenotype (average patient survival time after disease onset ~ 17 years) as compared to I113T SOD1^{2SH} and G85R SOD1^{2SH} mutations (average survival times of ~ 4.3 and 6 years, respectively; Wang *et al.*, 2008).

Analytical size exclusion chromatography (SEC) of all three mutants (with or without metal cofactors) showed single eluting species (Appendix Fig S3A). Mass spectrometric analyses also suggested these to be in their monomeric states (Appendix Fig S3B). Since SOD1 has been found to form dimer by involving Cys57 and Cys146, we used nonreducing SDS gel electrophoresis (Appendix Fig S3C) and native gel electrophoresis (Appendix Fig S3D) for further size characterization. Both methods show a single protein band corresponding to the monomeric state indicating the absence of any multimeric species. We found that the two variants in their native forms, I113T SOD1^{2SH} and G85R SOD1^{2SH} formed droplets while G37R SOD1^{2SH} did not (Fig 3A, Appendix Fig S3E). We observed that the addition of Cu did not have any effect on the condensed phase in either I113T SOD1^{2SH} or G85R SOD1^{2SH} (Fig 3A, Appendix Fig S3F). By contrast, the addition of Zn inhibited LLPS in I113T SOD1^{2SH} in a dose-dependent way (Fig 3A, Appendix Fig S3F). Interestingly, with G85R SOD1^{2SH}, the addition of Zn did not lead to complete inhibition of LLPS (Fig 3A, Appendix Fig S3F) when compared to that of I113T SOD1^{2SH}. FCS measurements confirmed that phase-separated condensates of I113T SOD1^{2SH} and G85R SOD1^{2SH} were composed of slow diffusing species (Fig 3B). The fluorescence lifetime of the probe increased inside the condensates (Appendix Fig S3G–I). Further, when we removed the metal ions from G37R SOD1^{2SH} by dialyzing the protein in EDTA, we found that the metal-free G37R SOD1^{2SH} mutant also readily underwent LLPS, further highlighting the central role of metal binding in this process (Fig 3C). The addition of Zn into metal-free G37R SOD1^{2SH} inhibited LLPS, while the addition of Cu did not yield any change (Fig 3C). When Zn was added to preformed condensates (postincubation condition) to see whether the LLPS can be reversed (Appendix Fig S3J), I113T SOD1^{2SH} droplets disappear completely whereas G85R SOD1^{2SH} droplets show partial dissolution (Appendix Fig S3J). These experiments suggest that the LLPS of SOD1^{2SH} is effectively reversible through Zn coordination for ALS mutants as well unless the Zn binding is significantly compromised as in the case of G85R SOD1^{2SH}.

LLPS of monomeric SOD1 is driven by an order-to-disorder transition in the absence of Zn

The results above lead to a natural question about the mechanism of LLPS in the absence of Zn or reduced Zn-binding in the case of ALS mutants. NMR studies indicate that the conformational landscape of ApoSOD1^{2SH} exhibits two sparsely populated conformers that correspond to non-native oligomers (Sekhar *et al.*, 2015). These oligomers form via interactions between the native dimeric interface and disordered loop VII. The tendency to form non-native oligomers may facilitate the formation of a liquid-like, condensed phase under suitable conditions.

We used FCS to study the hydrodynamics of the different SOD1^{2SH} variants in the absence and presence of Zn (Fig 4A,

Appendix Table S1). Both ApoSOD1^{2SH} and severe mutants (I113T SOD1^{2SH} and G85R SOD1^{2SH}) showed larger r_H when compared to G37R SOD1^{2SH} and WTSOD1^{2SH} (Appendix Table S1). The value of r_H obtained by FCS (this study) for ApoSOD1^{2SH} matched well with previous experimental data (Vassall *et al.*, 2011; Bunck *et al.*, 2018). To obtain further insights into the average conformational properties of SOD1, we plotted the literature values (Chakraborty *et al.*, 2021) of r_H of different proteins in their compact folded and chemically unfolded states. The log–log plot of the r_H values of the folded proteins as a function of the number of residues could be fit to a straight line with a slope of 0.29 (Fig 4B). For chemically unfolded proteins, the slope of the log–log plot was found to be 0.59. Interestingly, when we plotted the r_H values of different SOD1^{2SH} variants in Fig 4B, we found that ApoSOD1^{2SH}, I113T SOD1^{2SH}, and G85R SOD1^{2SH} were positioned near the line for the chemically unfolded proteins. When we plotted the r_H value of α -synuclein, a well-characterized intrinsically disordered protein, it was found positioned near the same line. WTSOD1^{2SH} and G37R SOD1^{2SH} variants, on the other hand, were found near the line obtained for the compact folded proteins. This suggests that ApoSOD1^{2SH} and severe variants (I113T SOD1^{2SH} and G85R SOD1^{2SH}) are more extended (or sample extended conformer more often) compared with G37R SOD1^{2SH} and WTSOD1^{2SH}. We also observed that r_H decreased substantially with the addition of Zn in ApoSOD1^{2SH} and severe variants I113T SOD1^{2SH} and G85R SOD1^{2SH} (Fig 4B, Appendix Fig S4A–C).

Since the addition of Zn resulted in large compaction in ApoSOD1^{2SH} and severe variants, we used FCS data to determine their Zn-binding affinity (Fig 4C). For the Zn-binding study, all protein variants were in their de-metalated Apo forms, which we prepared by dialyzing the protein samples with EDTA using previous literature. We found that while ApoSOD1^{2SH} and ApoG37R SOD1^{2SH} bind to Zn with the highest affinity (k_a of $1.28 \times 10^7 \text{ M}^{-1}$ and $1.54 \times 10^7 \text{ M}^{-1}$, respectively), the binding of ApoG85R SOD1^{2SH} is the weakest (k_a of $1.71 \times 10^6 \text{ M}^{-1}$). In comparison, ApoI113T SOD1^{2SH} showed an intermediate binding affinity (k_a of $0.75 \times 10^7 \text{ M}^{-1}$) towards Zn. We then used FTIR to determine how the secondary structure of the protein changed as a result of cofactor insertion. Using FTIR, we found that disorder/extended conformations were higher in metal-free ApoSOD1^{2SH} and severe variants (I113T SOD1^{2SH} and G85R SOD1^{2SH}) when compared to WTSOD1^{2SH} and G37R SOD1^{2SH} (Appendix Fig S4D, Appendix Table S2). The disordered/extended components in ApoSOD1^{2SH} and I113T SOD1^{2SH} (Fig 4D, Appendix Fig S4E and F) decreased as Zn was added, while the effect of Zn was less visible in G85R SOD1^{2SH} (Appendix Fig S4G). No significant change in the secondary structure for any variant was observed in the presence of Cu (Fig 4D, Appendix Fig S4E–G). Together, FTIR and FCS data revealed that the addition of Zn in ApoSOD1^{2SH} and I113T SOD1^{2SH} resulted in a conformational transition of the Zn-free protein from an extended (FCS data, greater r_H) and disordered (FTIR data) state to a compact (lower r_H) and less disordered state (FTIR data). For G85R SOD1^{2SH}, this transition is partial, presumably because of its weaker zinc binding compared with the I113T mutant.

Characterization of disorder in monomeric ApoSOD1^{2SH} using all-atom simulations

To complement FTIR and FCS experiments, we characterized the extent of conformational disorder for SOD1 monomer variants using

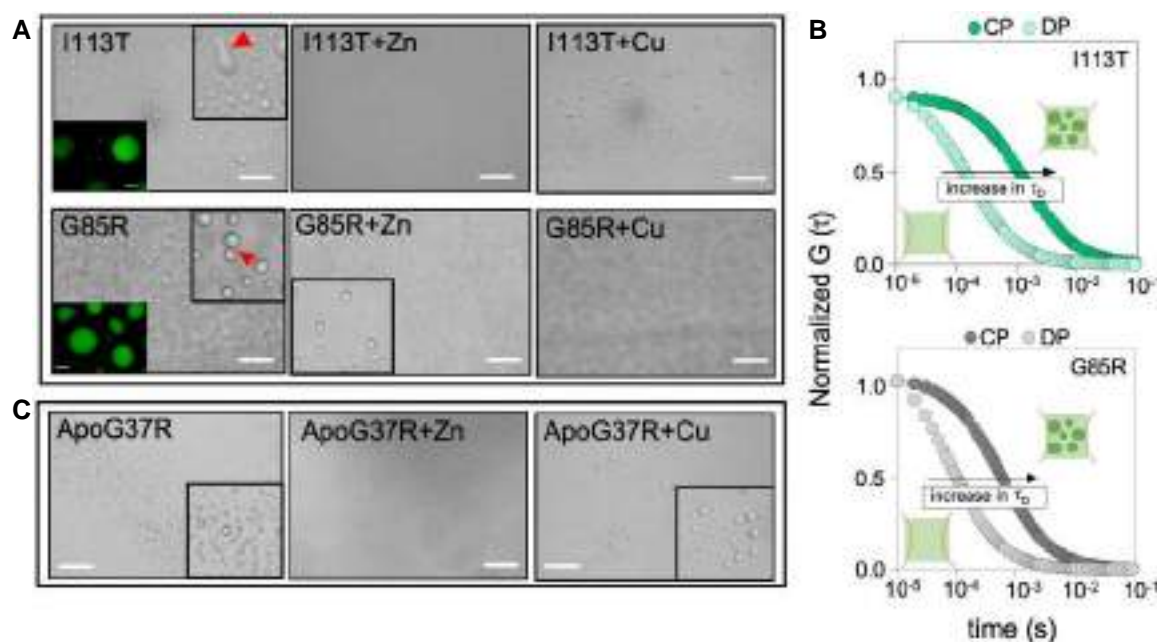


Figure 3. ALS mutants with compromised Zn binding undergo LLPS.

- A DIC microscopic images of I113T SOD1^{2SH} (top) and G85R SOD1^{2SH} (bottom) droplets incubated in the absence and presence of Zn and Cu, respectively (scale bar: 100 μ m); insets on bottom left show Alexa Fluor 488 maleimide-labeled protein condensates for I113T SOD1^{2SH} and G85R SOD1^{2SH}, respectively; scale bar: 5 μ m. Droplet dissolution was observed for I113T SOD1^{2SH} on the addition of Zn while droplets persisted on the addition of Cu. Red arrowhead indicates fusion of liquid droplets.
- B Amplitude normalized FCS curves of I113T SOD1^{2SH} (in green) and G85R SOD1^{2SH} (in gray) of dilute phase (DP) and condensed phase (CP) showing an increase in diffusion time from DP to CP. The intense color indicates CP, and light variant indicates DP.
- C On metal cofactor removal, ApoG37R SOD1^{2SH} formed condensates, which ceased to exist when protein was incubated with Zn, while condensates persisted on Cu addition (left to right); scale bar: 100 μ m.

Source data are available online for this figure.

microsecond timescale and atomistic MD simulations (Souza *et al.*, 2019; Timr *et al.*, 2020). Simulations were performed using the AMBER99SB-disp force field (Robustelli *et al.*, 2018) that was shown to be suitable for simulating both folded and disordered proteins (see [Materials and Methods](#)). The hydrodynamic radius r_H was calculated using the HullRad algorithm (Fleming & Fleming, 2018), which employs a convex hull method to estimate the hydrodynamic volume of the protein molecule. The mean r_H value determined from simulations ranges from 2.1 nm for ApoSOD1^{2SH} variants to 3.2 nm for unfolded SOD1^{2SH} (Fig 4B). The value of r_H for ApoSOD1^{2SH} from FCS measurements (2.80 ± 0.09 nm) lies within the range of simulation results, which indicates the partially unfolded nature of this variant. Secondary structure analysis of ApoSOD1^{2SH} variants using the DSSP algorithm (Kabsch & Sander, 1983) indicates the presence of coil-like conformations in loop IV/VII while β -sheet conformations were dominant in the expected β -barrel regions (Appendix Fig S5A). By contrast, unfolded SOD1^{2SH} adopted coil-like conformations with short stretches of α -helix and β -sheet conformations (Appendix Fig S5B). Distance root mean square deviation (dRMSD) analysis confirms that the β -barrel fold is stable (dRMSD ≤ 0.3 nm) across all ApoSOD1^{2SH} variants (Appendix Fig S5C), which is consistent with previous NMR/SAXS experiments (Furukawa *et al.*, 2016). Representative conformations of ApoSOD1^{2SH} and unfolded SOD1^{2SH} are shown in Appendix Fig S5D.

Consistent with secondary structure and dRMSD analysis, root mean-square fluctuation (RMSF) of α atoms suggests that ApoSOD1^{2SH} variants exhibit high conformational flexibility ($\text{RMSF}_{\text{max}} > 0.4$ nm) in loop-IV/VII regions (Fig 5A). To assess the effect of Zn binding on the conformational disorder of monomeric SOD1, we also simulated three additional SOD1 states: ApoSOD1^{S-S} (disulfide present, without metal cofactors), ZnSOD1^{2SH} (Zn-bound and disulfide-reduced) and ZnSOD1^{S-S} (Zn-bound and disulfide present). The stable coordination of Zn to SOD1^{2SH} and SOD1^{S-S} was confirmed based on distance analysis for Zn/Zn-binding residues over the course of the trajectories (Appendix Fig S5E and F). We compared the conformational flexibility across different regions of the SOD1 by analyzing their RMSF profiles (Fig 5B). The RMSF profile of ApoSOD1^{2SH} shows considerable flexibility in loop IV and loop VII wherein RMSF for several residues exceed 0.3 nm (Fig 5B, Appendix Movie EV1). Notably, the presence of disulfide bond only reduced flexibility in the aa: 51–60 region ($\text{RMSF}_{\text{max}} \sim 0.15$ nm) within loop IV, which is involved in disulfide bond formation through C57 while loop VII remained flexible. Zn significantly reduced the flexibility of loop IV ($\text{RMSF}_{\text{max}} \sim 0.15$ nm) to which it directly binds and led to a reduction in the RMSF of loop-VII residues (Appendix Movie EV2). In conclusion, the high flexibility of loop IV/VII observed in the absence of Zn in simulations is consistent with experimental observations and points towards an intrinsic propensity for structural disorder within the SOD1 monomer in the absence of Zn.

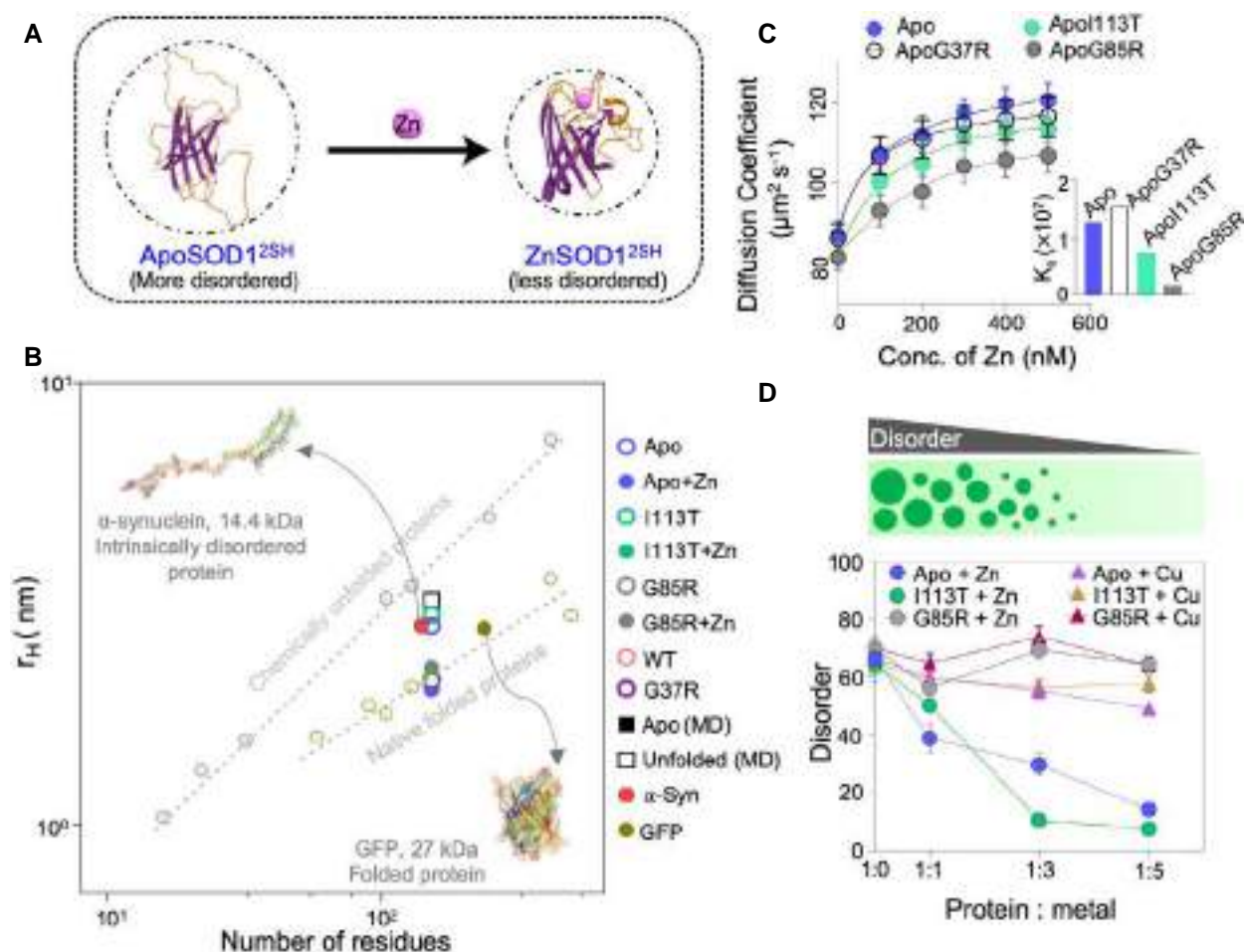


Figure 4. Zn drives disorder to order transition in SOD1.

A Scheme shows Zn-dependent disorder to order transition in monomeric SOD1.

B Plot of the \log_e of the hydrodynamic radius (r_H) versus the \log_e of the number of residues in the polypeptide chain. The line fitted to these data for the native folded proteins (yellow dashed) has a slope of 0.29 ± 0.02 and a y-axis intercept of 1.56 ± 0.1 , while the other fitted to the chemically denatured protein (gray dashed) data has a slope of 0.57 ± 0.02 and a y-axis intercept of 0.79 ± 0.07 . Literature data have been used for folded and chemically denatured proteins while we employed FCS to calculate the r_H of all SOD1^{2SH} variants with (solid shapes) and without Zn (hollow shapes). The hollow gray circle of G85R SOD1^{2SH} is directly under hollow green I113T SOD1^{2SH} in the log-log plot.

C Variation of diffusion coefficients of de-metalated protein variants determined from FCS measurement with increasing Zn concentration (inset shows a comparison of binding constants between mutants and Zn; ApoSOD1^{2SH} and ApoG37R SOD1^{2SH} has a higher binding affinity to Zn than ApoI113T SOD1^{2SH} and ApoG85R SOD1^{2SH}). Data are represented as mean \pm SD (from three biological replicates).

D Disordered/ extended conformation content decreases in ApoSOD1^{2SH} and ApoI113T SOD1^{2SH} with the addition of Zn calculated from FTIR spectra; data are represented as mean \pm SD (from three biological replicates).

Source data are available online for this figure.

To understand the mechanism by which G85R substitution in ApoSOD1^{2SH} may lead to loss of Zn binding, we analyzed the interactions of R85 with neighboring residues over the course of the 6 μ s run (Fig 5C and D). We observed that R85 formed salt bridges with key aspartate residues (Strange *et al*, 2006), which either stabilize Zn (D83/D124) or may play a role in stabilizing the native conformation of loop IV (D101). D83 directly binds to Zn whereas D124 coordinates two key histidine residues involved in Zn coordination. D101 natively forms a salt bridge with R79, which may help stabilize the conformation of loop IV. Overall, the simulation of ApoG85R SOD1^{2SH} suggests a mechanism wherein the formation of dynamic, non-native salt bridges involving R85 may hinder its ability to bind

Zn. The induction of non-native, intramolecular salt bridges through post-translational modifications (Skinner *et al*, 2017; Mohanty *et al*, 2019, 2021) has been previously shown to alter the binding affinity of protein-protein interactions and may therefore modulate ApoG85R SOD1^{2SH} affinity for Zn²⁺ through a similar mechanism.

CG simulations highlight the role of loop regions in ApoSOD1^{2SH} condensate formation

To determine which regions of ApoSOD1^{2SH} are involved in stabilizing the condensate, we performed coarse-grained (CG), phase coexistence simulations (Fig 5E) using a protocol, which has been described

previously (Mammen Regy *et al*, 2021). Briefly, ApoSOD1^{2SH} monomers were modeled at a single bead per amino acid resolution and formed a stable condensate at 275 K (Fig 5F—top,

Appendix Movie EV3). To model ApoSOD1^{2SH}, the residues which form the β -barrel structure were made rigid while those belonging to loop IV/VII were allowed to remain flexible. The analysis of

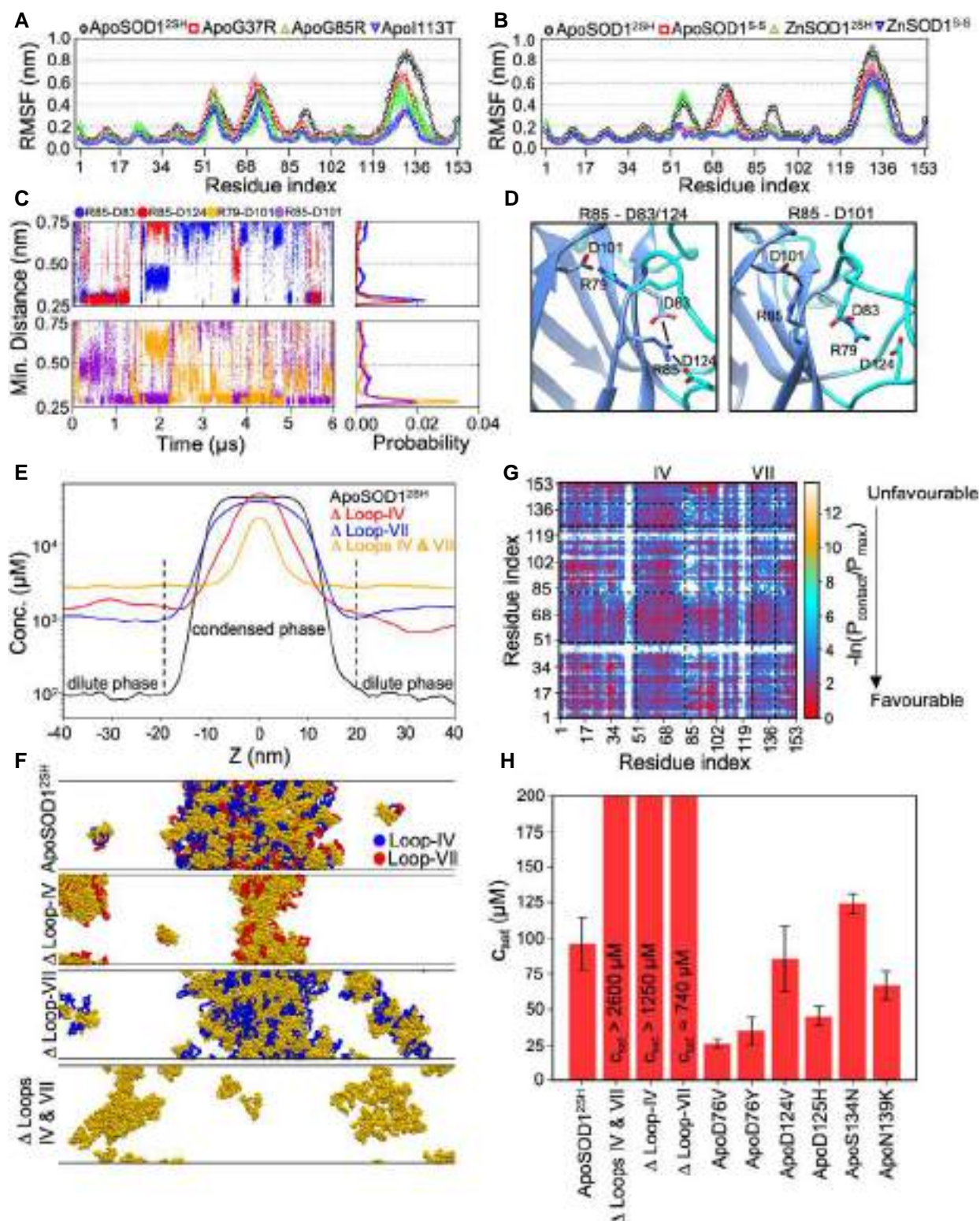


Figure 5.

Figure 5. Characterization of SOD1^{2SH} variants and molecular interactions in the condensed phase using molecular dynamics simulations.

- A, B (A) Per-residue RMSF profiles of ApoSOD1^{2SH} & its mutants computed from 5 μ s simulations performed for each variant. (B) Per-residue RMSF profiles of ApoSOD1^{2SH}, ApoSOD1^{S5}, ZnSOD1^{S5}, and ZnSOD1^{2SH} computed from 5 μ s simulations performed for each variant. Error bars in A and B correspond to standard errors, which are estimated by blocks averaging over 10 (500 ns each) blocks.
- C Salt-bridge analysis of ApoG85R SOD1^{2SH} (dist. cutoff < 0.5 nm = salt bridge).
- D Snapshots from the ApoG85R SOD1^{2SH} trajectory showing the formation of non-native salt bridges, which are likely to be detrimental for Zn-binding.
- E Density profile of ApoSOD1^{2SH} and its loop-deletion variants computed from the CG slab simulations. The condensed phase is centered in the middle of the simulation box.
- F Slab snapshots from CG simulations of ApoSOD1^{2SH} and its variants at 275 K (blue beads represent loop IV, red beads represent loop VII, and orange beads represent the other domains).
- G Pairwise intermolecular contact formation (normalized by maximum probability) in the condensed phase as a function of residue index.
- H Saturation concentration measured in the CG phase coexistence simulations for ApoSOD1^{2SH} and its variants including ALS mutants at 275 K. The error bars correspond to SD, which are estimated from block averages over four blocks.

Source data are available online for this figure.

intermolecular contact maps between SOD1 monomers in the condensed phase indicates that several regions of the β -barrel and disordered loop IV (aa:60–75) collectively stabilize the condensate (Fig 5G). By contrast, fewer intermolecular contacts were observed for loop VII owing to its shorter length. The observed contacts based on residue type indicate the presence of electrostatic interactions between lysine and aspartate/glutamate residues (Appendix Fig S5G and H). In addition, a wide range of pairwise interactions involving residue types such as valine/isoleucine and serine/glycine also contributed towards phase separation. Taken together, the CG simulation suggests that ApoSOD1^{2SH} condensate is stabilized through numerous interactions involving both the β -barrel and loop-IV/VII regions.

The presence of long, disordered loops was shown to destabilize the β -barrel structure of ApoSOD1^{2SH} (~ 3 kcal/mol) and promote aggregation (Yang *et al*, 2018). To assess the importance of disordered loop-IV/VII regions in the formation of ApoSOD1^{2SH} condensate, we tested the effect of loop deletion on the saturation concentration (c_{sat}) in simulations (Fig 5E). In comparison with full-length ApoSOD1^{2SH}, deletion of either loop IV/VII or both was found to substantially increase the concentration of the dilute phase (c_{sat} ; Fig 5F and H). These observations collectively suggest that loop-mediated interactions play an important role in the stabilization of the ApoSOD1^{2SH} condensed phase. Several ALS-associated mutations are found to occur in the loop-IV/VII regions, which do not impact the stability of the SOD1 but instead disrupt surface-exposed hydrogen bonds (Byström *et al*, 2010). Many of these mutations alter the net charge of SOD1, which may impact the stability of the condensed phase by modulating electrostatic interactions. Hence, we tested the impact of these mutants and found that those which decreased the net negative charge of SOD1 (D76 \rightarrow V/Y, D124V, D125H, N139K) reduced c_{sat} by up to two-fold (Fig 5H, Appendix Fig S5I). By contrast, the neutral substitution—S134N had no impact on c_{sat} (Fig 5H). These observations indicate the potential sensitivity of the condensed phase towards mutations, which alter the net charge of SOD1. Altogether, CG simulations highlight the importance of loop-IV/VII interactions in the condensed phase.

LLPS of SOD1 is followed by aggregation

Studies of RNA-binding proteins (Anderson & Kedersha, 2006; Satoh *et al*, 2012; Wheeler *et al*, 2016) involved in SG formation such as FUS, hnRNPA1/2, and TDP-43 indicate that LLPS of their disordered, low complexity domains (LCDs) gives rise to labile fibrils

upon droplet maturation. Moreover, the liquid-to-solid phase transition, which leads to the formation of fibrils was shown to be enhanced by mutations associated with neurodegenerative diseases. Based on these observations, it has been proposed that LLPS may represent an intermediate state en route to toxic aggregate formation (Babinchak & Surewicz, 2020).

After establishing that ApoSOD1^{2SH} and severe ALS mutants (I113T SOD1^{2SH} and G85R SOD1^{2SH}) undergo a Zn-dependent phase separation, we investigated the temporal maturation of ApoSOD1^{2SH} droplets using fluorescence microscopy in combination with FCS (Fig 6A and B). As the maturation progressed with time, we observed the presence of high-intensity fluorescent aggregates, which started forming within the droplets (Fig 6C). FCS experiments were carried out at different regions and different time points to investigate the diffusional dynamics of droplets maturation. For the FCS experiments, we chose three regions, namely the diffused part of the image outside the droplets (region 1, Fig 6A–C, Appendix Fig S6A); the relatively low-intensity portion inside the droplets (region 2, Fig 6A–C, Appendix Fig S6B); and the high-intensity regions inside the droplets, which contained the aggregates (region 3, Fig 6A–C). The analyses of the correlation functions obtained at region 1 showed the presence of fast diffusing molecules (Fig 6D). The hydrodynamic properties (r_H of 2.80 ± 0.09 nm) of these fast-moving molecules resembled that of labeled ApoSOD1^{2SH}, suggesting that region 1 predominantly contained monomeric protein.

By contrast, analyses of the correlation functions obtained inside the droplets (region 2) were complex. Even at the early time points (for example, at 0* h in Fig 6D, which shows the data at the earliest time point when LLPS was observed) the values of D were found to be considerably less than what was observed for the monomeric protein in solution or for the molecules present at the diffused region (region 1) indicating a restrictive environment inside the droplets. As the maturation progresses, the values of D decreased further with time (Fig 6D). Interestingly, at 24 h and beyond, the correlation functions contained more than one component with a large fraction of an extremely low diffusing component (Fig 6D). The region containing the aggregates (region 3) did not yield any correlation functions as their diffusion behavior was too slow to measure.

Aggregation kinetics and formation of amyloid fibrils

ThT fluorescence assay was used to determine whether the aggregates obtained after long incubation would eventually lead to the

amyloid formation or these are amorphous. We found that the ApoSOD1^{2SH} and two severe mutants (I113T SOD1^{2SH} and G85R SOD1^{2SH}) showed large ThT fluorescence indicating amyloid formation, while G37R SOD1^{2SH} did not aggregate (Fig 6E). The

aggregation kinetics were sigmoidal with prominent lag phases. We used atomic force microscopy (AFM) experiments to complement ThT fluorescence data (Fig 6F, Appendix Fig S6C), which provided information about the height and morphology of the aggregates.

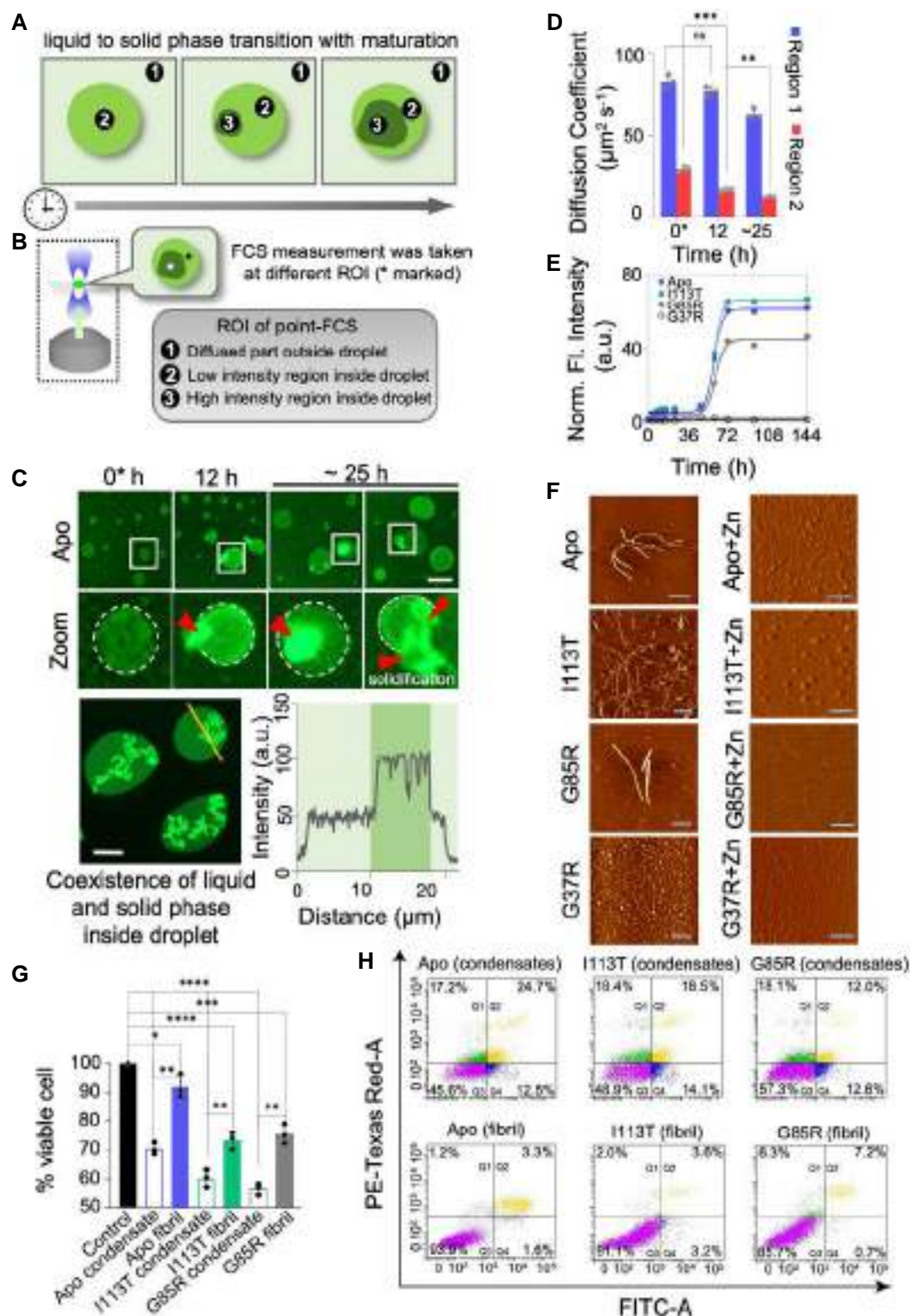


Figure 6.

Figure 6. Maturation of liquid droplets precedes aggregation.

- A Cartoon scheme showing the maturation of protein droplets with time (region 1: diffused region outside droplet, region 2: low-intensity portion inside the droplet, region 3: highly intense portion inside droplet appears during maturation) at different time points.
- B Diffusion coefficient of regions 1 and 2 (within droplet) was measured using point FCS as shown in the scheme.
- C Upper panel shows fluorescence images of the maturation of Alexa Fluor 488-labeled ApoSOD1^{2SH} droplets with time, samples were incubated at 37°C up to ~ 25 h. Images are taken at indicated time point: 0* hour (the time after incubation required for droplet formation), 12 h, and > 24 h; images below show magnified scale bar: 5 µm. The middle panel shows magnified view of the marked region from corresponding images on the upper panel. Red arrowhead indicates matured (solid) portion inside the droplet. Lower panel shows the coexistence of liquid and solid phases inside droplet; scale bar: 10 µm. Intensity plot (bottom right) shows the distribution of high-intensity region within matured droplet.
- D Diffusion coefficient obtained from point FCS measurement at different regions of the droplet during maturation course; 0* (x-axis label) indicates the time after incubation required for droplet formation. Data are shown mean ± SD (from three biological replicates). Statistical significance was measured using paired t-test; ns denotes nonsignificant; **P < 0.01; ***P < 0.001.
- E ThT fluorescence assay plot showing aggregation kinetics of all SOD1^{2SH} variants. ApoSOD1^{2SH}, I113T SOD1^{2SH}, and G85R SOD1^{2SH} show high ThT fluorescence.
- F AFM micrographs of ApoSOD1^{2SH}, I113T SOD1^{2SH}, and G85R SOD1^{2SH} show fibrillar aggregates after prolonged incubation at 37°C, 180 RPM in absence of Zn (left panel); AFM micrographs of ApoSOD1^{2SH}, I113T SOD1^{2SH}, and G85R SOD1^{2SH} incubated with Zn (at 1:5 protein:Zn molar ratio) show the presence of oligomers for ApoSOD1^{2SH}, I113T SOD1^{2SH} and short fibrils for G85R SOD1^{2SH} (right panel); scale bar: 200 nm.
- G Cell proliferation of SHSY5Y human neuroblastoma cells assessed by MTT assay post 12 h treatment with 5 µM ApoSOD1^{2SH}, I113T SOD1^{2SH}, and G85R SOD1^{2SH} condensates and aggregates (fibrils). Cell culture medium (DMEM) was used as negative control and untreated SHSY5Y cells were used as a positive control. Data are shown as mean ± SEM (from three biological replicates). P values were determined by two-tailed unpaired t tests; *P < 0.05, **P < 0.01; ***P < 0.001, ****P < 0.0001.
- H Dot plots showing flow cytometric analysis of annexin V and propidium iodide (PI) staining of apoptotic SHSY5Y neuroblastoma cells following a 12 h treatment with 5 µM ApoSOD1^{2SH} condensates, I113T SOD1^{2SH} condensates, G85R SOD1^{2SH} condensates, ApoSOD1^{2SH} fibrils, I113T SOD1^{2SH} fibrils, and G85R SOD1^{2SH} fibrils, respectively (see [Materials and Methods](#) for details). High cytotoxicity was observed for SOD1^{2SH} condensates.

Source data are available online for this figure.

AFM micrographs of ApoSOD1^{2SH} showed the presence of long curved fibrils with a height of 4 nm (Fig 6F, Appendix Fig S6C). I113T SOD1^{2SH} aggregates formed a fibrillar network of long dense fibrils with a height of 5 nm (Fig 6F, Appendix Fig S6C). AFM micrographs of G85R SOD1^{2SH} showed fibrillar aggregates with a height ranging between 4 and 8 nm.

We had observed earlier that LLPS was completely reversible when Zn was added either at the preincubation or postincubation conditions. Therefore, we chose to probe the effect of the metal cofactors on the formation and stability of amyloid aggregates under preincubation and postincubation conditions, respectively. When we added Zn at the beginning of incubation (preincubation), aggregation of ApoSOD1^{2SH} and I113T SOD1^{2SH} (Fig 6F, Appendix Fig S6D) was inhibited while the presence of Cu did not suppress aggregation (Appendix Fig S6E and F). AFM micrographs of ApoSOD1^{2SH} and I113T SOD1^{2SH} incubated in presence of Zn were observed to consist of oligomers alone (Fig 6F). Interestingly, short fibrils were observed for G85R SOD1^{2SH} incubated with Zn (Fig 6F), which is consistent with its significantly reduced affinity towards Zn. By contrast, when we added Zn at the stationary phase of the amyloid formation (144 h, postincubation), we found no significant change in ThT fluorescence (Appendix Fig S6G). These data in combination with the Zn-induced dissolution of ApoSOD1^{2SH} droplets clearly suggest that while the state of droplet formation is reversible by the addition of Zn, the protein aggregates are stable and not altered by either of the cofactors.

SOD1 condensates show higher toxicity compared with aggregates

Since mutations in SOD1 are linked to motor neuronal death and ALS pathology, we studied the toxicity of condensates as opposed to the aggregates using three different assays. For these assays, we prepared condensates and aggregates of different SOD1 variants, and their formation was checked using phase contrast microscopy (for condensates) and AFM (for aggregates), respectively. WTSOD1^{2SH} and G37R

SOD1^{2SH} were excluded from these assays as they did not form either condensates or aggregates. It may also be noted that nontoxic nature of WT-SOD1 was established by previous results (Clement *et al*, 2003; Magrané *et al*, 2009; Zhu *et al*, 2018; Sannigrahi *et al*, 2021). Untreated neuroblastoma cells in DMEM media were used as a control in all the following assays. Cultured SHSY5Y human neuroblastoma cells were treated for 12 h with 5 µM SOD1^{2SH} condensates and aggregates (after long incubation of 144 h), respectively, and cell death was first probed by trypan blue exclusion assay. This assay is based on the principle that cells that lose their membrane integrity are permeable to trypan blue dye. We observed a significant increase in cell death in SHSY5Y cells treated with SOD1^{2SH} condensates (Appendix Fig S6H). We complemented our observations with an MTT assay, which assesses the metabolic activity of cells reflecting the cell proliferation of the sample. 5 µM mutant SOD1^{2SH} condensates and aggregates were added to the cell media of SHSY5Y cells in a 96-well plate, respectively (see [Materials and Methods](#)). Condensates showed significantly higher toxicity than aggregates after incubation with MTT (Fig 6G). To validate these results, we used flow cytometry with annexin V and propidium iodide. 5 µM condensates and aggregates were added to the cell media of cultured SHSY5Y cells and incubated for 12 h at 37°C. Both apoptotic and necrotic cell populations were highest in cells treated with condensates. I113T SOD1^{2SH} condensate was observed to be the most toxic in terms of apoptotic and necrotic cell population (Fig 6H, Appendix Fig S6I). Complementing our findings, observations from recent studies (Bolognesi *et al*, 2019; Kanaan *et al*, 2020) on TDP-43 C-terminal domain and Tau, respectively, also indicate that condensates promote cellular toxicity as opposed to aggregates. Further studies are needed to determine the relative significance of condensate versus aggregate toxicity for proteins implicated in neurodegenerative diseases.

Discussion

The link between SOD1 stability, aggregation, and its relation to ALS disease characteristics has been extensively studied. Mutant

SOD1 aggregates were found in inclusion bodies formed in the spinal cord of familial ALS patients (Shibata *et al*, 1996). Notably, aggregates isolated from spinal cord tissue of ALS-SOD1 mouse models were found to be metal deficient (Shaw *et al*, 2008) implying that ApoSOD1 is aggregation-prone. ALS mutants were shown to exert their destabilizing effect predominantly on ApoSOD1^{2SH} and could trigger unfolding at physiological temperature (Furukawa & O'Halloran, 2005). The extent of structural destabilization (decrease in T_m) induced by fALS-associated mutations in monomeric ApoSOD1^{2SH} was shown to be positively correlated to aggregation propensity (Vassall *et al*, 2011). However, decreased thermal stability/increased aggregation propensity was uncorrelated with disease severity (Byström *et al*, 2010; Vassall *et al*, 2011). Based on these observations, it was suggested that ApoSOD1^{2SH} may play an important role in ALS, while additional factors, such as environmental changes and the presence of conformational heterogeneity may be involved, highlighting the mechanistic complexity of ALS onset and progression.

SOD1 has been reported to associate with and alter SG dynamics. T-cell intracellular antigen-1 (TIA-1) is an RNA-binding protein that promotes the formation of SGs and is critical to the eukaryotic cellular stress response. Overexpression of mutant SOD1 increases TIA-1 positive inclusions in spinal cord tissue of ALS transgenic mouse and familial ALS patient (Lee *et al*, 2020). Mutant SOD1 also co-

localizes and interacts with another important SG marker G3BP1 (Gal *et al*, 2016). Since both G3BP1 and TIA-1 are RNA-binding proteins, their interactions with mutant SOD1 suggest a potential link between SOD1 mutations and RNA metabolism alterations.

Using both experiments and molecular simulations, we show here that while compact, WTSOD1^{2SH} does not undergo phase separation, partially disordered ApoSOD1^{2SH} or Zn-compromised mutants engage in intermolecular interactions, which lead to condensate formation. Based on the data presented in this study, we suggest here a “cofactor-regulated LLPS model of SOD1” (Fig 7), which shows that Zn (and not Cu) removal induces sampling of disordered states and the generation of LLPS. We also observe that further incubation of the condensates results in a liquid-to-solid-like transition, which culminates in aggregation.

Recently, Hatters and colleagues (Ruff *et al*, 2022) showed that mutations, which reduce the thermal stability of globular proteins, can trigger their phase separation *in vivo* and lead to the formation of unfolded protein deposits (UPODs). These deposits were found to be stabilized by homotypic interactions between hydrophobic core residues, which are exposed upon unfolding. Further, heterotypic interactions between unfolded proteins could promote colocalization within condensates as observed for barnase (I25A, I196G) and SOD1 (A4V). Interestingly, Ebbinghaus and colleagues (Samanta *et al*, 2021) observed that the partitioning of SOD1 into

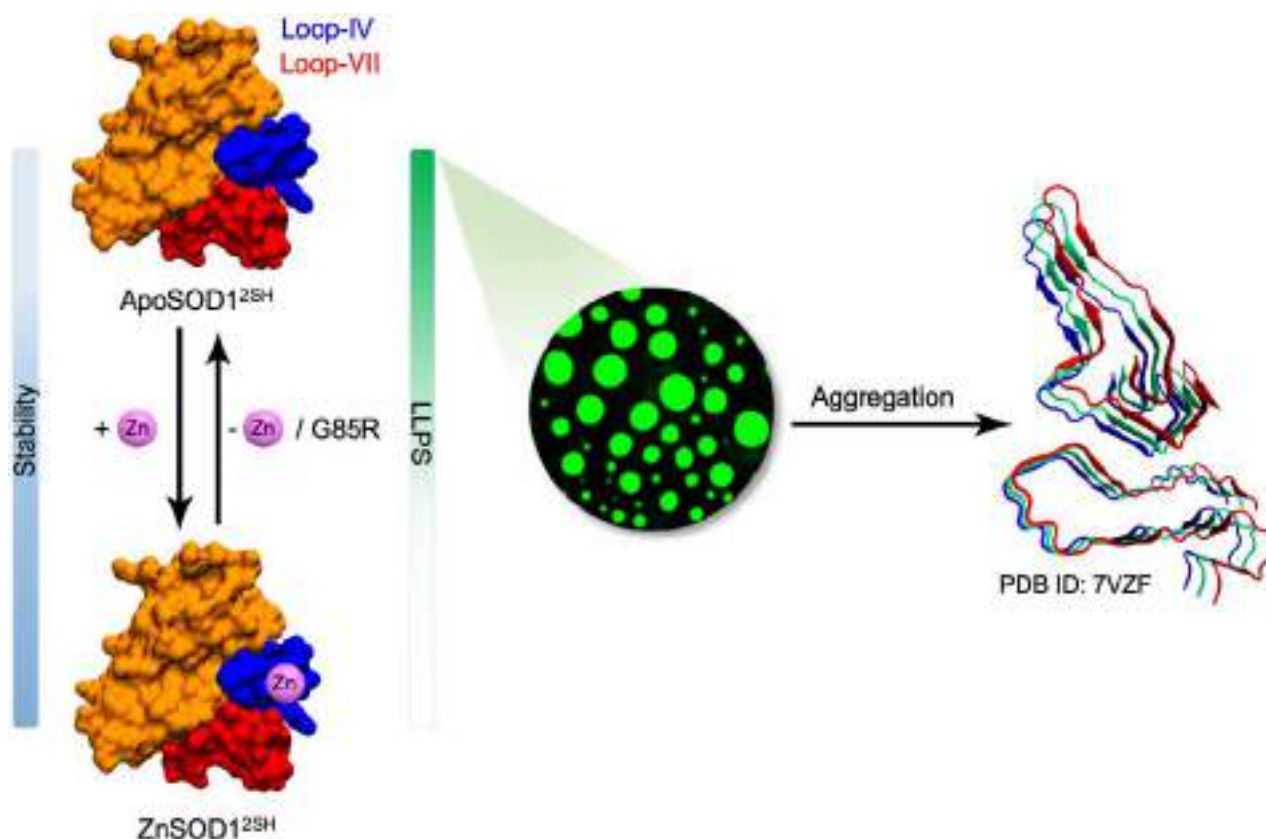


Figure 7. A schematic describing the mechanism by which Zinc regulates LLPS and aggregation of SOD1.

In the absence of Zn, SOD1 exhibits conformational disorder (instability) in the loop regions (IV/VII), which promotes LLPS and the subsequent maturation of condensates into aggregates. Upon binding to Zn, the loop regions adopt a rigid conformation, which inhibits LLPS.

SGs in response to heat shock treatment was more sensitive to the modulation of specific protein–protein interactions in the cytoplasm than on fold stability.

Here, we show that the loss of Zn, which promotes solvent exposure of disordered loop regions, is sufficient to trigger phase separation of SOD1 under physiological conditions. Our CG simulations of ApoSOD1^{2SH} suggest that interactions that involve the disordered loop-IV/VII regions can promote its phase separation. Notably, Oliveberg and co-workers (Yang *et al*, 2018) showed that the presence of disordered loops IV/VII destabilizes the ApoSOD1^{2SH} monomer by ~ 3 kcal/mol. The structural destabilization induced by the absence of Zn (either in ApoSOD1^{2SH} or in the Zn-compromised ALS mutants) can result in local unfolding and/or more efficient sampling of the transient locally unfolded structures. These locally unfolded states have been shown to generate amyloid formation in globular folded proteins (Chiti & Dobson, 2009), and a similar mechanistic interpretation can also be applied in the present case of SOD1 phase separation, which eventually matures into the amyloid aggregation.

Our results correlate well with the severity of disease phenotypes for three ALS disease mutants under *in vitro* conditions. The less severe G37R SOD1^{2SH} mutant is compact with a lower tendency towards LLPS. By contrast, more severe I113T SOD1^{2SH} and G85R SOD1^{2SH} mutants, with reduced Zn affinity are more disordered, readily forming droplets and subsequent aggregates. Interestingly, unlike I113T SOD1^{2SH} (and ApoSOD1^{2SH}), the disease mutant G85R SOD1^{2SH} exhibits a significant reduction in Zn-binding affinity due to non-native salt bridge formation as substantiated by atomistic simulation data. A number of complementary assays presented in our study suggest that the cellular toxicity of SOD1 condensates is higher than large aggregates, which form after maturation. One limitation of these assays where condensates are added to the cells exogenously in the cell culture media is that it is difficult to ascertain whether the condensates remain in their initial state or transform to a different state, given their transient nature and uncharacterized material properties. Keeping this limitation in mind, we note the similarity of our data to the results of Lehner and colleagues (Bolognesi *et al*, 2019). They generated more than 50,000 mutants in the prion-like domain of TDP-43 and showed that LLPS-promoting mutants exhibited increased toxicity in yeast cells while aggregate-forming mutants reduced cellular toxicity. Detailed and careful investigations are needed to characterize the toxicity of the droplets with respect to their interconversion dynamics, material properties, and cellular uptake properties.

Several studies emphasize the toxicity induced by small oligomers as opposed to large aggregates in ALS and other neurodegenerative diseases (Vega *et al*, 2019; Chakraborty *et al*, 2021). Incubation of ApoSOD1^{S-S} *in vitro* under physiological conditions was shown to form soluble, non-native oligomers, which persisted even under reducing conditions (Redler *et al*, 2014). Based on NMR experiments, Kay and colleagues reported that the free energy landscape of immature ApoSOD1^{2SH} is rugged and comprises four transiently populated conformers in equilibrium with the native state (Sekhar *et al*, 2015). Two of the conformers exist as non-native oligomers and are regarded as “off-pathway” states to the mature, native SOD1 dimer. Key events during SOD1 maturation such as metalation and oxidation assist in eliminating the off-pathway oligomers that correspond to high energy states in immature

ApoSOD1^{2SH} (Culik *et al*, 2018). Non-native, trimeric SOD1 oligomers, which are transiently formed, were found to strongly promote neuronal cell death (Proctor, 2016). Interestingly, it was observed that LLPS of Tau promoted the acquisition of pathogenic conformations and the formation of toxic oligomers (Kanaan *et al*, 2020). Similarly, we speculate that LLPS may facilitate the formation of toxic SOD1 oligomers and would explain the greater toxicity of SOD1 condensates compared with aggregates. A detailed understanding of how condensates metamorphose to inclusion bodies could open possibilities for developing therapeutic drugs targeting these non-native oligomers instead of aggregate species.

Materials and Methods

Materials

For the purification of SOD1, LB media, isopropyl-1-thio-β-D-galactopyranoside (IPTG), CuSO₄, Tris-HCl, NaCl, imidazole, dithiothreitol (DTT), sodium phosphate monobasic, sodium phosphate dibasic, sodium acetate, and EDTA from Sigma Aldrich, St. Louis, USA were used. Ni-NTA resin from Thermo Fisher Scientific, MA, USA was used. For LLPS study, HEPES, heparin, polyethylene glycol (PEG) 8,000, and polyethylenimine (PEI) were purchased from Sigma Aldrich, MO, USA. For protein labelling, AlexaFluor488 maleimide and tris 2-carboxyethyl phosphine (TCEP) from Thermo Fisher Scientific, MA, USA, and Sigma Aldrich, MO, USA, were used, respectively. All media, supplements, reagents, and kits for cell culture were obtained from Invitrogen, CA, USA, unless stated otherwise.

Recombinant SOD1^{2SH} purification

SOD1 plasmid was transformed into competent *E. coli* (BL21 DE3 strain) cells using the heat shock method. Transformed bacterial cells were grown in LB media at 37°C. The overexpression of SOD1 was induced with 1 ml of 1 M IPTG in 1 L culture after cells reached the log phase (at OD₆₀₀ ~ 0.6–0.8). 1 mM CuSO₄ was added to the culture for proper metal loading over the protein. The cells were allowed to grow for 3.5 h after which they were pelleted down by centrifugation at 4,000 g for 15 min at 4°C. Cells were re-suspended in prechilled lysis buffer (20 mM Tris-HCl + 500 mM NaCl, pH 8.0). After thorough re-suspension in lysis buffer, cells were sonicated (20 pulses, each of 30 s with an interval time of 1 min) to allow cell lysis. Unbroken cells and debris were removed by another centrifugation step at 16,100 g for 30 min. The supernatant obtained was carefully removed and allowed to bind to Ni-NTA agarose resin. The Ni-NTA column was washed using 50 ml wash buffer (20 mM Tris-HCl, 500 mM NaCl, and 50 mM imidazole, pH 8.0) followed by elution with 20 mM Tris-HCl, 500 mM NaCl, 500 mM imidazole, pH 8.0, and 1 mM DTT. Protein concentration of eluted fractions was determined by their absorbances at 280 nm. The eluted fractions were pooled and dialyzed using SnakeSkin Dialysis Tubing (10 KDa MWCO) in 20 mM Na-phosphate buffer and 1 mM DTT, pH 7.4. The protein concentration of the postdialyzed fraction was estimated by recording absorbance at 280 nm using the monomeric molar extinction coefficient of 5,500 M⁻¹ cm⁻¹ (Wright *et al*, 2013).

Preparation of ApoSOD1^{2SH}

ApoSOD1 was prepared from the WTSOD1^{2SH} by metal removal following previously reported protocol (McCords & Fridovich, 1969). WTSOD1^{2SH} was subjected to overnight dialysis in 50 mM Na acetate, 10 mM EDTA, pH 3.8 to carry out the proper removal of metal ions. EDTA was removed by successive dialysis in 50 mM Na acetate pH 5.2 and in 20 mM Na-phosphate, pH 7.4. This was followed by dialysis in Na-phosphate buffer, pH 7.4.

Size exclusion chromatography and MALDI mass spectrometry

100 μ M of freshly purified protein (G37R SOD1^{2SH}, ApoG37R SOD1^{2SH}, I113T SOD1^{2SH}, ApoI113T SOD1^{2SH}, G85R SOD1^{2SH}, and ApoG85R SOD1^{2SH}) were loaded on a gel filtration column (Bio-Rad Enrich SEC 70 10 \times 300) fitted to a Fast Protein Liquid Chromatography (FPLC) system (Bio-Rad NGC chromatography system, Bio-Rad Laboratories, USA) and absorbance change at 280 nm of the elution was monitored. The molecular weights of the eluted fractions of the proteins collected after the run were determined by Matrix Assisted Laser Desorption/Ionization (MALDI) mass spectrometer (4800 MALDI-TOF/TOF Analyzer, Applied Biosystems/MDS SCIEX, USA).

Native PAGE

Freshly purified SOD1 variants (G37R SOD1^{2SH}, ApoG37R SOD1^{2SH}, I113T SOD1^{2SH}, ApoI113T SOD1^{2SH}, G85R SOD1^{2SH}, and ApoG85R SOD1^{2SH}) were run on a 15% nondenaturing polyacrylamide gel. The wells were loaded with 20 μ g protein. 20 μ g Bovine Serum Albumin (BSA) and lysozyme were used as protein standards.

Liquid–liquid phase separation *in vitro*

To study LLPS and liquid droplet formation, 100 μ M SOD1^{2SH} and its mutants, respectively, were incubated in 20 mM HEPES buffer (pH 7.4), ~ 7% (w/v) heparin, and 100 mM NaCl for 20 min at 37°C with constant shaking of 180 RPM. 10 μ l of the reaction mixture was aliquoted and drop casted onto grease-free glass slides with single concavity and covered with a 22 mm coverslip (Blue Star, India), sealed with commercially available nail polish. LLPS was also induced with neutral crowding agent PEG-8000 from 5% to 20% (w/v) and cationic polymer PEI 5% and 10% (w/v) and 100 mM NaCl for 20 min at 37°C with constant shaking of 180 RPM. The slides were visualized with a 10 \times and 40 \times objective using Leica microsystems DMIL LED inverted fluorescence microscope (Wetzlar, Germany) in the DIC mode and fluorescence mode for imaging droplets composed of labeled protein. Droplet numbers from different fields were computed using ImageJ software (NIH, MD, USA). The optical density of the samples was measured at 600 nm with Hidex Sense Microplate Reader (Turku, Finland). The turbidity was measured as optical density from three independent measurements.

Fluorescent labelling of protein

All SOD1^{2SH} protein variants were labeled using a thiol active fluorescence dye AlexaFluor 488 maleimide (Invitrogen, MA, USA) following a previously established protocol (Kundu et al, 2017). The

fluorescence dye was dissolved in DMSO and added to 2 mg/ml solution of protein under constant stirring. The molar ratio between the protein and dye was 1:10. The reaction mixture was incubated at 4°C for 5 h with vortexing after every 30 min. The labelling reaction was then quenched by adding excess β -mercaptoethanol. Excess free dye from the reaction mixture was removed by extensive dialysis in Na-phosphate (pH 7.4) buffer using SnakeSkin (Thermo Fisher Scientific, MA, USA) Dialysis Tubing (10 kDa MWCO) followed by column chromatography using a Sephadex G20 column (Bio-rad Laboratories, CA, USA), which was pre-equilibrated with 20 mM Na-phosphate buffer (pH 7.4).

Lifetime and anisotropy of protein condensates

15 nM-labeled ApoSOD1^{2SH}, I113T SOD1^{2SH}, and G85R SOD1^{2SH} along with 100 μ M unlabeled protein were subjected to LLPS conditions, and droplets were visualized under a confocal microscope for time-domain FLIM experiments. The time-resolved fluorescence measurements were made using a time-correlated single photon counting (TCSPC) setup of Alba (ISS Inc., IL, USA). Measurement samples were excited using a 488 nm QuixX picosecond pulsed laser made by Omicron-Laserage Laserprodukte GmbH (Germany). The repetition rate of the laser was set to be 20 MHz. The laser was linearly polarized in the vertical direction, and a linear polarization cleanup filter (DPM-100-VIS by Meadowlark Optics) was used for further improving the extinction ratio. For FLIM measurements, the fluorescence emission was detected by a single photon avalanche diode (SPAD) detector (SPD-100-CTC by Micro Photon Devices) after the 530/43-nm band-pass filter (Semrock, NY, USA). For the anisotropy measurements, the fluorescence emission was separated by the polarization beam splitter into two channels, which are parallel and perpendicular to the orientation of the linear polarization of the excitation; both parallel and perpendicular emissions were simultaneously detected by two SPAD detectors using the same 530/43-nm band-pass filters. Both the FLIM and the anisotropy data were analyzed using the ISS 64-bit VistaVision software. For FLIM data analysis, the software allows the single or multiexponential curve fittings on a pixel-by-pixel basis using a weighted least-squares numerical approach (Lakowicz, 1999; Gryczynski et al, 2009; Sun et al, 2011). The double-exponential model was used for fitting the lifetime data of diffused and condensed ApoSOD1^{2SH} with the instrument response function, estimated by taking the first derivative of the rising of the decay. For time-resolved anisotropy data analysis, the software performs the global fittings of both fluorescence lifetimes and rotation times. The steady-state anisotropy (r) was calculated by

$$r = (I_{\text{par}} - I_{\text{per}}) / (I_{\text{par}} + 2I_{\text{per}}) \quad (1)$$

where I_{par} and I_{per} are the measured intensities in the parallel and perpendicular channels, respectively.

Fluorescence correlation spectroscopy

Fluorescence Correlation Spectroscopy (FCS) measures the fluctuations of fluorescence intensity in the confocal volume and yields the diffusion times of the fluorescent species. For nanomolar level binding study using FCS, 15 nM Alexa 488 labeled monomeric protein

mixed with unlabeled protein keeping total unlabeled protein (demetallized) concentration at 100 nM in the presence of increasing concentration of Zn from 1:0 to 1:5 molar ratio and 10 mM TCEP. The FCS measurements were carried out using an ISS Alba FFS/FLIM confocal system (Champaign, IL, USA), coupled to a Nikon Ti2U microscope equipped with the Nikon CFI PlanApo 60X/ 1.2NA water immersion objective. The 48-nm picosecond pulsed diode laser was used for the excitation of the FCS measurements. The fluorescence emission was collected using a pair of SPAD (Single Photon Avalanche Detector) detectors with the 50/50 beam splitter and the 530/43-nm band-pass filter. The use of two detectors enabled us to determine single-color cross-correlation functions to eliminate the artifacts given the detector after-pulsing. The FCS correlation curves were fit to the 3D Gaussian 1-component diffusion model, where the beam waists in the radial and axial dimensions were calibrated using a standard fluorescence dye (Rhodamine 6G, R6G) in water of known diffusion coefficient ($2.8 \times 10^{-6} \text{ cm}^2/\text{s}$). Diffusion coefficients of different mutants are measured by measuring the diffusion time (τ_D) and using the relation (Chatterjee et al, 2019):

$$\frac{D_{\text{protein}}}{D_{\text{R6G}}} = \frac{\tau_{D, \text{R6G}}}{\tau_{D, \text{protein}}} \quad (2)$$

The hydrodynamic radii of each species were computed from their respective diffusion coefficients (D). For comparison between hydrodynamic radii of the wild-type protein and its mutants, Alexa Fluor 488 labeled monomeric protein (15 nM) and 100 nM unlabeled protein in presence of 10 mM TCEP in 20 mM Na-phosphate buffer (pH 7.4) was used. The FCS data obtained were normalized with respect to free dye following a previously published method (Chattopadhyay et al, 2005).

In the 3D Gaussian diffusion model involving a single type of diffusing molecules (the 3D Gaussian 1-component model excluding the contributions of the triplet state), the correlation function $G(\tau)$ can be defined by the following equation:

$$G(\tau) = 1 + \frac{1}{N} \cdot \left(\frac{1}{1 + \left(\frac{\tau}{\tau_D} \right)} \right) \cdot \left(\frac{1}{\sqrt{1 + S^2 \left(\frac{\tau}{\tau_D} \right)^2}} \right) \quad (3)$$

where τ_D denotes the diffusion time of the diffusing molecules, N is the average number of molecules within the observation volume, and S is the structural parameter that defines the ratio between the radius and the height. The value of τ_D obtained by fitting the correlation function is related to the diffusion coefficient (D) of a molecule by the following equation:

$$\tau_D = \omega^2 / 4D \quad (4)$$

where ω is the size of the observation volume. From here, the value of the hydrodynamic radius (r_H) of the protein molecule/complex/ aggregate can be obtained from D using the Stokes–Einstein formula:

$$D = kT / 6\pi\eta r_H \quad (5)$$

where η is the viscosity, T is the absolute temperature and k is the Boltzmann constant.

All-atom MD simulation protocol and analysis

Initial structures for all ApoSOD1^{2SH} monomers were taken from PDB entry 2C9V (Chain F). Structural mutations were made through rotamer substitutions using the Dunbrack rotamer library in UCSF Chimera (Pettersen et al, 2004). Initial conformation for the all-atom simulation of unfolded SOD1 was taken from a 1 μs single-chain simulation performed using the single bead per-residue, HPS-Urry model (Mammen Regy et al, 2021). The coarse-grained structure was converted to an all-atom model using MODELER (Eswar et al, 2008). All systems were modeled based on the AMBER99SB-disp force field (Robustelli et al, 2018) along with a modified version of the TIP4P-D water model (Piana et al, 2015). Force field parameters for Zn and Zn-coordinated residues were obtained from previous studies (Macchiagodena et al, 2019, 2020). Energy minimization and equilibration were performed using GROMACS 2020 (Páll, 2020). The SOD1 monomer was placed into an octahedral box of 6.5-nm length. Energy minimization of the protein was first performed in vacuum using the steepest descent algorithm. Following vacuum minimization, TIP4P-D water molecules were added, and the solvated system was further minimized using the steepest descent algorithm. To mimic physiological salt concentration (0.1 M), Na⁺ and Cl[−] ions were added along with additional Na⁺ counter ions to achieve electrical neutrality. NVT equilibration was performed using Noose-Hoover thermostat ($T_c = 1.0 \text{ ps}$) to stabilize the system temperature at 300 K. NPT equilibration was performed using the Berendsen barostat (Berendsen et al, 1984) with isotropic coupling ($T_p = 5.0 \text{ ps}$) to achieve a system pressure of 1 bar. All production simulations were performed using OpenMM 7.5 (Eastman et al, 2017) in the canonical ensemble at 300 K using the Langevin middle integrator (Zhang et al, 2019) with a friction coefficient of 1 ps^{-1} . Masses of all hydrogen atoms were increased to 1.5 amu, which allowed for a simulation timestep of 4 fs. Constraints were applied to all hydrogen-containing bonds using the SHAKE algorithm (Ryckaert et al, 1977). Short-range nonbonded interactions were calculated based on a cutoff radius of 0.9 nm. Long-range electrostatic interactions were treated using the PME method (Darden et al, 1993).

Hydrodynamic radii were calculated using the HullRad algorithm (Fleming & Fleming, 2018) and averaged over 500 ns intervals. All other analysis was carried out using analysis programs available within GROMACS. Secondary structure fractions were calculated based on the DSSP library (Kabsch & Sander, 1983) using gmx do dssp. Per-residue root mean-square fluctuation (RMSF) and distance root mean square deviation (dRMSD) were calculated using gmx rmsf and gmx rmsdist, respectively. Minimum distances in G85R ApoSOD1^{2SH} were measured between arginine N η atoms and aspartate O δ atoms using gmx mindist.

CG MD slab simulation protocol and analysis

Phase coexistence simulation of ApoSOD1^{2SH} and its variants were conducted using the HOOMD-Blue 2.9.3 software package (Anderson et al, 2020) with features extended using azplugins (version 0.10.1; <https://github.com/mpohwardlab/azplugins>), using a protocol proposed in our previous works (Dignon et al, 2018; Mammen Regy et al, 2021). We simulated “partially rigid/flexible” SOD1 chains wherein loop IV (aa: 49–81) and VII (aa: 124–139) of SOD1

are allowed to be flexible while the rest of the protein remains folded/rigid. Regions except Loop IV/VII were constrained as a rigid body using the `hoomd.md.constrain.rigid` function (Nguyen *et al*, 2011; Glaser *et al*, 2020), keeping the initial structure from PDB entry 2C9V. Partially folded SOD1 was modeled based on the HPS-Urry model (Regy *et al*, 2021), in which solvent is treated implicitly. The initial slab geometry ($14 \times 14 \times 280$ nm) was prepared from the 100 chains of SOD1 sequence, then a 5 μ s NVT simulation (with 10 fs time step) was conducted at 275 K using a Langevin thermostat with the residue friction factor, $\gamma_i = m_i/\tau_{\text{damp}}$. Here m_i is the mass of each amino acid bead (g/mol), τ_{damp} is the damping parameter, which was set to 1,000 ps. The first microsecond of the trajectory was treated as equilibration time and skipped for the calculation of the density profile and contact maps.

Contact analysis of the coarse-grained simulation was carried out with MDAnalysis (Michaud-Agrawal *et al*, 2011). Two amino acids (i and j) were considered in contact in the simulations when their inter-bead distance was less than $1.5\sigma_{ij}$ where $\sigma_{ij} = (\sigma_i + \sigma_j)/2$ is the average of the bead diameter of the respective amino acids i and j. The intermolecular contact probability ($P = \text{mean}(n_{ij})$ where $n_{ij} = 1$ if distance criteria are met, otherwise $n_{ij} = 0$) was computed by averaging the individual contact over the trajectory. The residue index contact map is plotted as $-\ln(P/P_{\text{max}})$, where P_{max} is the maximum probability observed between any pairs of amino acids in the given sequence.

The concentrations c_{sat} (μ M) and c_{dense} (μ M) of vapor and dense phases along Z, respectively, were determined by centering the trajectory on the slab for each frame so that the dense phase with the largest number of chains is placed at $z = 0$ for all frames. This is done using clustering according to the center-of-mass distance between chain pairs. All the measured properties were divided into four independent blocks to estimate error bars.

Time-based maturation study using fluorescence correlation spectroscopy

100 μ M unlabeled ApoSOD1^{2SH} with 15 nM Alexa-488 labeled ApoSOD1^{2SH} was incubated at 37°C, 180 RPM for maturation study for 28 h. 10 μ l of the sample aliquoted from different time points 30 min postincubation (marked as 0*), 12 h, and ~ 25 h were drop casted in a depression slide (Blue Star, India) and mounted with 22 mm coverslip (Bluestar, India) and sealed with commercially available nail polish. The slide was visualized under the confocal microscope using TD-FLIM (Nikon Eclipse Ti2, Japan) at 60 \times water emersion objective. FCS measurements were taken from regions with varying intensities within the droplet using point FCS mode. The FCS correlation curves were fit to the 3D Gaussian 1-component diffusion model, where the beam waists in the radial and axial dimensions were calibrated using a standard fluorescence dye (Rhodamine 6 G, R6G) in water of known diffusion rate.

Thioflavin T (ThT) assay

For monitoring the effect of Zn on the aggregation kinetics of SOD1^{2SH}, all protein variants were incubated in the presence and absence of Zn under shaking at 180 RPM at 37°C for 350 h. The protein concentrations for the aggregate preparation were 100 μ M in 20 mM HEPES buffer at pH 7.4. Aliquots of proteins were

withdrawn at each time point in the aggregation pathway and diluted in 20 mM HEPES buffer at pH 7.4 to reach a volume of 500 μ l. ThT was added to protein in a 1:10 molar ratio (protein: ThT). Steady-state fluorescence measurements were recorded in a quartz cuvette of path length 1 cm using a Photon Technology International (PTI) fluorescence spectrometer with excitation wavelength of 450 nm, emission wavelength of 485 nm and an integration time of 0.1 s averaging over three times. For seeded aggregation, 10% (10 μ M) seed of prepared condensates and aggregates were added to 100 μ M protein, respectively, and studied for aggregation by detecting ThT fluorescence as mentioned previously.

Atomic force microscopy

Aggregating samples of SOD1^{2SH} and its mutants were aliquoted after prolonged incubation at 37°C and diluted 20 times with milliQ water. A 5 μ l diluted sample was drop casted on freshly cleaved mica. The aggregates were rinsed with MilliQ water and then dried using a stream of nitrogen. Images were acquired at room temperature using a Bioscope Catalyst AFM (Bruker Corporation, MA, USA) with silicon probes. The standard tapping mode was used to image the morphology of aggregates. The nominal spring constant of the cantilever was kept at 20–80 N/m. The spring constant was calibrated by a thermal tuning method. A standard scan rate of 0.5 Hz with 512 samples per line 6 was used for imaging the samples. A single third-order flattening of height images with a low pass filter was done followed by section analysis to determine the dimensions of aggregates.

Cell culture and cytotoxicity assay

Neuroblastoma cell lines SHSY5Y acquired from the national cell repository (National Centre for Cell Science, Pune, India) were authenticated using STR analysis. The cells tested negative for mycoplasma contamination as tested using PCR. Cells were maintained in Dulbecco's modified Eagle's media (DMEM), which in turn were supplemented with 10% heat-inactivated fetal bovine serum (FBS), respectively, 4.5 g/L of glucose, 1.5 g/L sodium bicarbonate, 110 mg/L sodium pyruvate, 4 mM l-glutamine, 50 units/ml penicillin G, and 50 μ g/ml streptomycin in humidified air containing 5% CO₂ at 37°C. Sub-culturing was done by allowing the passaging of cells as per ATCC recommendations (ATCC, VA, USA).

Trypan Blue exclusion assay was performed to determine the number of viable cells present in cell suspension after a 12 h treatment with 5 μ M SOD1^{2SH} condensates, oligomer, and fibrils. It is based on the principle that viable cells have intact cell membranes that exclude certain dyes such as trypan blue. SHSY5Y cells were seeded in 6-well plates at 1×10^6 cells/well and incubated for 24 h at 37°C, 5% CO₂. 5 μ M preformed ApoSOD1^{2SH}, I113T SOD1^{2SH}, and G85R SOD1^{2SH} condensates, oligomers and fibrils were added to each well, respectively, and incubated for 12 h at 37°C, 5% CO₂. Following incubation, cells were trypsinized and 20 μ l 0.4% trypan blue solution from Sigma Aldrich, MO, USA was added to 20 μ l cell suspension. 20 μ l of this mixture was added between the hemocytometer and cover slip. The loaded hemocytometer was examined under a light microscope at 10 \times magnification. The number of blue-stained cells and total cells were counted. Percentage of viable cells was calculated from the formula:

$$\% \text{viable cells} = \frac{[1 - (\text{number of blue cells} / \text{total number of cells})] \times 100}{(6)}$$

MTT assay was employed to evaluate the cellular cytotoxicity on the addition of SOD1^{2SH} condensates, oligomers, and fibrils to determine which structures were the most toxic. SHSY5Y cells (4×10^3 cells per well) were seeded in a 96-well plate and incubated at 37°C, 5% CO₂ for 24 h. After 24 h, cells were treated with preformed ApoSOD1^{2SH}, I113T SOD1^{2SH}, and G85R SOD1^{2SH} condensates, oligomers, and fibrils at a concentration of 5 µM for 12 h. After 12 h of incubation, cells were washed with PBS, and then following the manufacturer's protocol, 10 µl of 12 mM MTT stock solution from Invitrogen Vybrant MTT Cell Proliferation Assay kit was added to each well and kept in incubator at 37°C, 5% CO₂ for 4 h to form formazan salt. The formazan salt was solubilized by adding 50 µl DMSO to each well and mixing thoroughly, following an incubation of 10 min at 37°C. The absorbance was recorded at 540 nm using an ELISA reader (Emax, Molecular Device). DMEM was used as the blank or negative control and untreated cells were used as the positive control. Percentage cell viability was calculated from the formula:

$$\% \text{cell viability} = \frac{[(\text{absorbance}_{\text{sample}} - \text{absorbance}_{\text{blank}}) / (\text{absorbance}_{\text{control}} - \text{absorbance}_{\text{blank}})] \times 100}{(7)}$$

For the FITC-Annexin V/ Propidium Iodide early and late apoptosis analyses, cells were seeded in 6 wells plates at 1×10^6 cells/ well. 24 h after seeding, the cells were subjected to preformed ApoSOD1^{2SH}, I113T SOD1^{2SH}, and G85R SOD1^{2SH} condensates, oligomers, and fibrils to understand which structures were the most toxic. The final concentration of the protein added to the cells was maintained at 5 µM. After the addition of the treatments, the cells were incubated for 12 h at 37°C, 5% CO₂. The percentage of apoptotic cells was determined using the Invitrogen Dead Cell Apoptosis Kit following instructions from the manufacturer. Apoptosis is a cellular process that entails a genetically programmed series of events leading to the death of a cell. During early apoptosis, the lipid phosphatidylserine (PS) is translocated to the outer leaflet of the plasma membrane from the cytoplasmic side. FITC-conjugated Annexin V is a strong probe for the exposed PS and can be used for detecting early apoptosis in stressed cells. For the determination of late apoptosis and/or necrosis as a result of oligomer treatment, propidium iodide (PI) was added to the treated cells at a concentration of 2 µg/ml. PI labels the cellular DNA in late apoptotic/ necrotic cells where the cell membrane has been completely ruptured, and the nuclear membrane has been dilated to release nucleus contents. The BD LSRFortessa flow cytometer was employed for Fluorescence Activated Cell Sorting (FACS) to analyze the apoptotic, necrotic, and viable cell populations in treated SHSY5Y cells.

Fourier transform infrared spectroscopy (FTIR)

FTIR spectra of ApoSOD1^{2SH} and SOD1^{2SH} mutants in the presence of increasing concentrations of zinc and copper were acquired using Bruker 600 series FTIR spectrometer. Protein samples at a concentration of 20 µM were treated with increasing concentrations of zinc sulphate and copper sulphate, from molar ratios 1:1 to 1:5 (protein: metal ion), respectively, in 20 mM Na-phosphate buffer at pH 7.4 and incubated for 15 min at room temperature before the

measurements. All the FTIR measurements were carried out in Na-phosphate buffer. The experiments were carried out in solution, and the buffer baseline was subtracted before recording each spectrum. The spectral readouts were obtained on absorbance mode with a path length of 0.01 mm following standard methodology. The deconvolution of raw spectra in the amide I region (1,700–1,600 cm⁻¹) was done using least-squares iterative curve fitting to Gaussian/ Lorentzian line shapes. Peak identifications were typically carried out by using double derivatives of the FTIR spectra, as described before (Goormaghtigh *et al*, 1990; Sarkar-Banerjee *et al*, 2016; Mahapatra *et al*, 2019). We used OriginPro 9 software for the curve fitting, second derivative analysis, and other data fitting.

Data availability

This study includes no data deposited in external repositories.

Expanded View for this article is available [online](#).

Acknowledgements

We thank T. Murugunandan, Sounak Bhattacharya and S. Laha for technical support in Atomic Force Microscopy, Confocal microscopy and Fourier Transform Infrared Spectroscopy; Central Instrumentation Facility, CSIR-Indian Institute of Chemical Biology for provision of infrastructure; Bishal Roy for image processing; work done at CSIR-Indian Institute of Chemical Biology was supported by a research grant (MLP-139) from Council of Scientific & Industrial Research (CSIR). BD and SR are supported by fellowships from CSIR and University Grants Commission, respectively. Work done at Texas A&M University was supported by NINDS and NIA R01NS116176. All-atom simulations were performed on the Extreme Science and Engineering Discovery Environment (XSEDE), which is supported by National Science Foundation grant number ACI-1548562. The simulations utilized the XSEDE Expanse GPU at the San Diego Supercomputer Center through allocation of TG-MCB120014. Coarse-grained simulations were conducted with the advanced computing resources provided by Texas A&M High Performance Research Computing.

Author contributions

Krishnananda Chattopadhyay: Conceptualization; resources; supervision; funding acquisition; writing – review and editing. **Bidisha Das:** Formal analysis; validation; investigation; writing – original draft; writing – review and editing. **Sumangal Roychowdhury:** Data curation; formal analysis; validation; writing – original draft; writing – review and editing. **Priyesh Mohanty:** Formal analysis; methodology; writing – original draft; writing – review and editing. **Azamat Rizuan:** Formal analysis; methodology; writing – original draft; writing – review and editing. **Jeetain Mittal:** Conceptualization; supervision; writing – original draft; project administration; writing – review and editing. **Joy Chakraborty:** Visualization.

Disclosure and competing interests statement

The authors declare that they have no conflict of interest.

References

- Ambadipudi S, Biernat J, Riedel D, Mandelkow E, Zweckstetter M (2017) Liquid-liquid phase separation of the microtubule-binding repeats of the Alzheimer-related protein tau. *Nat Commun* 8: 275

- Andersen PM (2006) Amyotrophic lateral sclerosis associated with mutations in the CuZn superoxide dismutase gene. *Curr Neurol Neurosci Rep* 6: 37–46
- Anderson P, Kedersha N (2006) RNA granules. *J Cell Biol* 172: 803–808
- Anderson JA, Glaser J, Glotzer SC (2020) HOOMD-blue: a python package for high-performance molecular dynamics and hard particle Monte Carlo simulations. *Comput Mater Sci* 173: 109363
- Annunziata O, Asherie N, Lomakin A, Pande J, Ogun O, Benedek GB (2002) Effect of polyethylene glycol on the liquid–liquid phase transition in aqueous protein solutions. *Proc Natl Acad Sci U S A* 99: 14165–14170
- Babinchak WM, Surewicz WK (2020) Liquid–liquid phase separation and its mechanistic role in pathological protein aggregation. *J Mol Biol* 432: 1910–1925
- Babinchak WM, Dumm BK, Venus S, Boyko S, Putnam AA, Jankowsky E, Surewicz WK (2020) Small molecules as potent biphasic modulators of protein liquid–liquid phase separation. *Nat Commun* 11: 5574
- Berendsen HJ, Postma JV, Van Gunsteren WF, DiNola ARHJ, Haak JR (1984) Molecular dynamics with coupling to an external bath. *J Chem Phys* 81: 3684–3690
- Bhandari K, Cotten MA, Kim J, Rosen MK, Schmit JD (2021) Structure-function properties in disordered condensates. *Journal of Physical Chemistry B* 125: 467–476
- Boeynaems S, Alberti S, Fawzi NL, Mittag T, Polymenidou M, Rousseau F, Schymkowitz J, Shorter J, Wolozin B, Van Den Bosch L et al (2018) Protein phase separation: a new phase in cell biology. *Trends Cell Biol* 28: 420–435
- Bolognesi B, Faure AJ, Seuma M, Schmiedel JM, Tartaglia GG, Lehner B (2019) The mutational landscape of a prion-like domain. *Nat Commun* 10: 4162
- Boundedjah O, Hamon L, Savarin P, Desforges B, Curmi PA, Pastré D (2012) Macromolecular crowding regulates assembly of mRNA stress granules after osmotic stress: new role for compatible osmolytes. *J Biol Chem* 287: 2446–2458
- Boyko S, Qi X, Chen TH, Surewicz K, Surewicz WK (2019) Liquid–liquid phase separation of tau protein: the crucial role of electrostatic interactions. *J Biol Chem* 294: 11054–11059
- Brangwynne CP (2013) Phase transitions and size scaling of membrane-less organelles. *J Cell Biol* 203: 875–881
- Brangwynne CP, Tompa P, Pappu RV (2015) Polymer physics of intracellular phase transitions. *Nat Phys* 11: 899–904
- Bunck DN, Atsavapranee B, Museth AK, VanderVelde D, Heath JR (2018) Modulating the folding landscape of superoxide dismutase 1 with targeted molecular binders. *Angewandte Chemie – International Edition* 57: 6212–6215
- Byström R, Andersen PM, Gröbner G, Oliveberg M (2010) SOD1 mutations targeting surface hydrogen bonds promote amyotrophic lateral sclerosis without reducing apo-state stability. *J Biol Chem* 285: 19544–19552
- Cao X, Antonyuk SV, Seetharaman SV, Whitson LJ, Taylor AB, Holloway SP, Strange RW, Doucette PA, Valentine JS, Tiwari A et al (2008) Structures of the G85R variant of SOD1 in familial amyotrophic lateral sclerosis. *J Biol Chem* 283: 16169–16177
- Chakraborty R, Dey S, Sil P, Paul SS, Bhattacharyya D, Bhunia A, Sengupta J, Chattopadhyay K (2021) Conformational distortion in a fibril-forming oligomer arrests alpha-Synuclein fibrillation and minimizes its toxic effects. *Communications Biology* 4: 518
- Chatterjee S, Ghosh S, Mishra S, Das Saha K, Banerji B, Chattopadhyay K (2019) Efficient detection of early events of α -Synuclein aggregation using a cysteine specific hybrid scaffold. *Biochemistry* 58: 1109–1119
- Chattopadhyay K, Saffarian S, Elson EL, Frieden C (2005) Measuring unfolding of proteins in the presence of denaturant using fluorescence correlation spectroscopy. *Biophys J* 88: 1413–1422
- Chiti F, Dobson CM (2009) Amyloid formation by globular proteins under native conditions. *Nat Chem Biol* 5: 15–22
- Clement AM, Nguyen MD, Roberts EA, Garcia ML, Boillée S, Rule M, McMahon AP, Doucette W, Siwek D, Ferrante RJ et al (2003) Wild-type nonneuronal cells extend survival of SOD1 mutant motor neurons in ALS mice. *Science* 302: 113–117
- Conicella AE, Dignon GL, Zerbe GH, Schmidt HB, D'Ordine AM, Kim YC, Rohatgi R, Ayala YM, Mittal J, Fawzi NL (2020) TDP-43 α -helical structure tunes liquid–liquid phase separation and function. *Proc Natl Acad Sci U S A* 117: 5883–5894
- Culik RM, Sekhar A, Nagesh J, Deol H, Rumpf JAO, Meiering EM, Kay LE (2018) Effects of maturation on the conformational free-energy landscape of SOD1. *Proc Natl Acad Sci U S A* 115: E2546–E2555
- Culotta VC, Klomp LWJ, Strain J, Casareno RLB, Krebs B, Gitlin JD (1997) The copper chaperone for superoxide dismutase. *J Biol Chem* 272: 23469–23472
- Darden T, York D, Pedersen L (1993) Particle mesh Ewald: an $N \cdot \log(N)$ method for Ewald sums in large systems. *J Chem Phys* 98: 10089–10092
- Dignon GL, Zheng W, Kim YC, Best RB, Mittal J (2018) Sequence determinants of protein phase behavior from a coarse-grained model. *PLoS Comput Biol* 14: e1005941
- Dignon GL, Best RB, Mittal J (2020) Biomolecular phase separation: from molecular driving forces to macroscopic properties. *Annu Rev Phys Chem* 71: 53–75
- Eastman P, Swails J, Chodera JD, McGibbon RT, Zhao Y, Beauchamp KA, Wang L-P, Simonnet AC, Harrigan MP, Stern CD et al (2017) OpenMM 7: rapid development of high-performance algorithms for molecular dynamics. *PLoS Comput Biol* 13: e1005659
- Eswar N, Eramian D, Webb B, Shen MY, Sali A (2008) Protein structure modeling with MODELLER. In *Structural proteomics*, Kobe B, Guss M, Huber T (eds), pp 145–159. Totowa, NJ: Humana Press
- Farwell NE, Lambert-Smith IA, Warraich ST, Blair IP, Saunders DN, Hatters DM, Yerbury JJ (2015) Distinct partitioning of ALS associated TDP-43, FUS and SOD1 mutants into cellular inclusions. *Sci Rep* 5: 13416
- Fleming PJ, Fleming KG (2018) HULLRad: fast calculations of folded and disordered protein and nucleic acid hydrodynamic properties. *Biophys J* 114: 856–869
- Furukawa Y, O'Halloran TV (2005) Amyotrophic lateral sclerosis mutations have the greatest destabilizing effect on the apo-and reduced form of SOD1, leading to unfolding and oxidative aggregation. *J Biol Chem* 280: 17266–17274
- Furukawa Y, Torres AS, O'Halloran TV (2004) Oxygen-induced maturation of SOD1: a key role for disulfide formation by the copper chaperone CCS. *EMBO J* 23: 2872–2881
- Furukawa Y, Anzai I, Akiyama S, Imai M, Cruz FJC, Saio T, Nagasawa K, Nomura T, Ishimori K (2016) Conformational disorder of the most immature Cu, Zn-superoxide dismutase leading to amyotrophic lateral sclerosis. *J Biol Chem* 291: 4144–4155
- Gal J, Kuang L, Barnett KR, Zhu BZ, Shissler SC, Korotkov KV, Hayward LJ, Kasarskis EJ, Zhu H (2016) ALS mutant SOD1 interacts with G3BP1 and affects stress granule dynamics. *Acta Neuropathol* 132: 563–576
- Ghosh A, Mazarakos K, Zhou HX (2019) Three archetypical classes of macromolecular regulators of protein liquid–liquid phase separation. *Proc Natl Acad Sci U S A* 116: 19474–19483
- Glaser J, Zha X, Anderson JA, Glotzer SC, Travestet A (2020) Pressure in rigid body molecular dynamics. *Comput Mater Sci* 173: 109430
- Goormaghtigh E, Cabiaux V, Ruysschaert JM (1990) Secondary structure and dosage of soluble and membrane proteins by attenuated total reflection

- Fourier-transform infrared spectroscopy on hydrated films. *Eur J Biochem* 193: 409–420
- Gryczynski I, Luchowski R, Bharill S, Borejdo J, Gryczynski Z (2009) Non-linear curve fitting methods for time-resolved data analysis. In *FLIM microscopy in biology and medicine*, Periasamy A, Clegg RM (eds), pp 341–370. Boca Raton, FL: Chapman and Hall/CRC
- Hayward LJ, Rodriguez JA, Kim JW, Tiwari A, Goto JJ, Cabelli DE, Valentine JS, Brown RH (2002) Decreased metallation and activity in subsets of mutant superoxide dismutases associated with familial amyotrophic lateral sclerosis. *J Biol Chem* 277: 15923–15931
- Hennig J, Andrésen C, Museth AK, Lundström P, Tibell LAE, Jonsson BH (2015) Local destabilization of the metal-binding region in human copper-zinc superoxide dismutase by remote mutations is a possible determinant for progression of ALS. *Biochemistry* 54: 323–333
- Hyman AA, Simons K (2012) Beyond oil and water – phase transitions in cells. *Science* 337: 1047–1049
- Hyman AA, Weber CA, Jülicher F (2014) Liquid-liquid phase separation in biology. *Annu Rev Cell Dev Biol* 30: 39–58
- Kabsch W, Sander C (1983) Dictionary of protein secondary structure: pattern recognition of hydrogen-bonded and geometrical features. *Biopolymers* 22: 2577–2637
- Kanaan NM, Hamel C, Grabinski T, Combs B (2020) Liquid-liquid phase separation induces pathogenic tau conformations *in vitro*. *Nat Commun* 11: 2809
- Kang J, Lim L, Song J (2018) ATP enhances at low concentrations but dissolves at high concentrations liquid-liquid phase separation (LLPS) of ALS/FTD-causing FUS. *Biochem Biophys Res Commun* 504: 545–551
- Krainer G, Welsh TJ, Joseph JA, Espinosa JR, Wittmann S, de Csilléry E, Sridhar A, Toprakcioglu Z, Gudiškytė G, Czekalska MA et al (2021) Reentrant liquid condensate phase of proteins is stabilized by hydrophobic and non-ionic interactions. *Nat Commun* 12: 1085
- Kroschwald S, Maharana S, Simon A (2017) Hexanediol: a chemical probe to investigate the material properties of membrane-less compartments. *Matters* <https://doi.org/10.19185/matters.201702000010>
- Kundu A, Kundu S, Chattopadhyay K (2017) The presence of non-native helical structure in the unfolding of a beta-sheet protein MPT63. *Protein Sci* 26: 536–549
- Lakowicz JR (1999) Instrumentation for fluorescence spectroscopy. In *Principles of fluorescence spectroscopy*, Lakowicz JR (ed), pp 25–61. Boston, MA: Springer
- Lee DY, Jeon GS, Sung JJ (2020) ALS-linked mutant SOD1 associates with TIA-1 and alters stress granule dynamics. *Neurochem Res* 45: 2884–2893
- Macchiagodena M, Pagliai M, Andreini C, Rosato A, Procacci P (2019) Upgrading and validation of the AMBER force field for histidine and cysteine zinc (II)-binding residues in sites with four protein ligands. *J Chem Inf Model* 59: 3803–3816
- Macchiagodena M, Pagliai M, Andreini C, Rosato A, Procacci P (2020) Upgraded AMBER force field for zinc-binding residues and ligands for predicting structural properties and binding affinities in zinc-proteins. *ACS Omega* 5: 15301–15310
- Magrané J, Hervás I, Henning MS, Damiano M, Kawamata H, Manfredi G (2009) Mutant SOD1 in neuronal mitochondria causes toxicity and mitochondrial dynamics abnormalities. *Hum Mol Genet* 18: 4552–4564
- Mahapatra A, Sarkar S, Biswas SC, Chattopadhyay K (2019) An aminoglycoside antibiotic inhibits both lipid-induced and solution-phase fibrillation of α -synuclein *in vitro*. *Chem Commun* 55: 11052–11055
- Maiza A, Chantepie S, Vera C, Ffife A, Huynh MB, Stettler O, Ouidja MO, Papy-Garcia D (2018) The role of heparan sulfates in protein aggregation and their potential impact on neurodegeneration. *FEBS Lett* 592: 3806–3818
- Mammen Regy R, Zheng W, Mittal J (2021) Using a sequence-specific coarse-grained model for studying protein liquid-liquid phase separation. *Methods Enzymol* 646: 1–17
- Mateju D, Franzmann TM, Patel A, Kopach A, Boczek EE, Maharana S, Lee HO, Carra S, Hyman AA, Alberti S (2017) An aberrant phase transition of stress granules triggered by misfolded protein and prevented by chaperone function. *EMBO J* 36: 1669–1687
- Mccords JM, Fridovich I (1969) Superoxide dismutase an enzymatic function for erythrocuprein (Hemocuprein). *J Biol Chem* 244: 6049–6055
- Michaud-Agrawal N, Denning EJ, Woolf TB, Beckstein O (2011) MDAnalysis: a toolkit for the analysis of molecular dynamics simulations. *J Comput Chem* 32: 2319–2327
- Mohanty P, Rashmi HBI, Arun GS, Das R (2019) Deamidation disrupts native and transient contacts to weaken the interaction between UBC13 and RING-finger E3 ligases. *Elife* 8: e49223
- Mohanty P, Chatterjee KS, Das R (2021) NEDD8 Deamidation inhibits Cullin RING ligase dynamics. *Front Immunol* 12: 695331
- Mohanty P, Kapoor U, Sundaravadivelu Devarajan D, Phan TM, Rizuan A, Mittal J (2022) Principles governing the phase separation of multidomain proteins. *Biochemistry* 61: 2443–2455
- Mojumdar S, Scholl ZN, Dee DR, Rouleau L, Anand U, Garen C, Woodside MT (2017) Partially native intermediates mediate misfolding of SOD1 in single-molecule folding trajectories. *Nat Commun* 8: 1881
- Molliex A, Temirov J, Lee J, Coughlin M, Kanagaraj AP, Kim HJ, Mittag T, Taylor JP (2015) Phase separation by low complexity domains promotes stress granule assembly and drives pathological fibrillization. *Cell* 163: 123–133
- Murthy AC, Dignon GL, Kan Y, Zerze GH, Parekh SH, Mittal J, Fawzi NL (2019) Molecular interactions underlying liquid-liquid phase separation of the FUS low-complexity domain. *Nat Struct Mol Biol* 26: 637–648
- Nguyen TD, Phillips CL, Anderson JA, Glotzer SC (2011) Rigid body constraints realized in massively-parallel molecular dynamics on graphics processing units. *Comput Phys Commun* 182: 2307–2313
- Páll S (2020) Heterogeneous parallelization and acceleration of molecular dynamics simulations in GROMACS. *J Chem Phys* 153: 134110
- Park S, Barnes R, Lin Y, Jeon B, Najafi S, Delaney KT, Fredrickson GH, Shea J-E, Hwang DS, Han S (2020) Dehydration entropy drives liquid-liquid phase separation by molecular crowding. *Commun Chem* 3: 83
- Pettersen EF, Goddard TD, Huang CC, Couch GS, Greenblatt DM, Meng EC, Ferrin TE (2004) UCSF chimera—a visualization system for exploratory research and analysis. *J Comput Chem* 25: 1605–1612
- Piana S, Donchev AG, Robustelli P, Shaw DE (2015) Water dispersion interactions strongly influence simulated structural properties of disordered protein states. *J Phys Chem B* 119: 5113–5123
- Pokrishevsky E, Grad LI, Yousefi M, Wang J, Mackenzie IR, Cashman NR (2012) Aberrant localization of FUS and TDP43 is associated with misfolding of SOD1 in amyotrophic lateral sclerosis. *PLoS ONE* 7: e35050
- Proctor EA (2016) Nonnative SOD1 trimer is toxic to motor neurons in a model of amyotrophic lateral sclerosis. *Proc Natl Acad Sci U S A* 113: 614–619
- Pullara P, Alshareedah I, Banerjee PR (2022) Temperature-dependent reentrant phase transition of RNA-polycation mixtures. *Soft Matter* 18: 1342–1349
- Ray S, Singh N, Kumar R, Patel K, Pandey S, Datta D, Mahato J, Panigrahi R, Navalkar A, Mehra S et al (2020) α -Synuclein aggregation nucleates through liquid-liquid phase separation. *Nat Chem* 12: 705–716
- Redler RL, Fee L, Fay JM, Caplow M, Dokholyan NV (2014) Non-native soluble oligomers of Cu/Zn superoxide dismutase (SOD1) contain a conformational epitope linked to cytotoxicity in amyotrophic lateral sclerosis (ALS). *Biochemistry* 53: 2423–2432

- Regy RM, Thompson J, Kim YC, Mittal J (2021) Improved coarse-grained model for studying sequence dependent phase separation of disordered proteins. *Protein Sci* 30: 1371–1379
- Robustelli P, Piana S, Shaw DE (2018) Developing a molecular dynamics force field for both folded and disordered protein states. *Proc Natl Acad Sci U S A* 115: E4758–E4766
- Ros MD, Deol HK, Savard A, Guo H, Meiering EM, Gibbings D (2020) Wild-type and mutant SOD1 localizes to RNA-rich structures in cells and mice but does not bind RNA. *J Neurochem* 156: 524–538
- Rosen DR, Siddique T, Patterson D, Figlewicz DA, Sapp P, Hentati A, Donaldson D, Goto J, O'Regan JP, Deng HX *et al* (1993) Mutations in Cu/Zn superoxide dismutase gene are associated with familial amyotrophic lateral sclerosis. *Nature* 362: 59–62
- Rotunno MS, Bosco DA (2013) An emerging role for misfolded wild-type SOD1 in sporadic ALS pathogenesis. *Front Cell Neurosci* 7: 253
- Rowland LP, Shneider NA (2001) Amyotrophic lateral sclerosis. *N Engl J Med* 344: 1688–1700
- Ruff KM, Choi YH, Cox D, Ormsby AR, Myung Y, Ascher DB, Radford SE, Pappu RV, Hatters DM (2022) Sequence grammar underlying the unfolding and phase separation of globular proteins. *Mol Cell* 82: 3193–3208
- Ryckaert JP, Ciccotti G, Berendsen HJ (1977) Numerical integration of the cartesian equations of motion of a system with constraints: molecular dynamics of n-alkanes. *J Comput Phys* 23: 327–341
- Samanta N, Ribeiro SS, Becker M, Laborie E, Pollak R, Timr S, Sterpone F, Ebbinghaus S (2021) Sequestration of proteins in stress granules relies on the in-cell but not the *in vitro* folding stability. *J Am Chem Soc* 143: 19909–19918
- Sannigrahi A, Chowdhury S, Das B, Banerjee A, Halder A, Kumar A, Saleem M, Naganathan AN, Karmakar S, Chattopadhyay K (2021) The metal cofactor zinc and interacting membranes modulate sod1 conformation-aggregation landscape in an in vitro ALS model. *Elife* 10: e61453
- Sarkar-Banerjee S, Chowdhury S, Paul SS, Dutta D, Ghosh A, Chattopadhyay K (2016) The non-native helical intermediate state may accumulate at low pH in the folding and aggregation landscape of the intestinal fatty acid binding protein. *Biochemistry* 55: 4457–4468
- Satoh R, Tanaka A, Kita A, Morita T, Matsumura Y, Umeda N, Takada M, Hayashi S, Tani T, Shinmyozu K *et al* (2012) Role of the RNA-binding protein Nrd1 in stress granule formation and its implication in the stress response in fission yeast. *PLoS ONE* 7: e29683
- Sekhar A, Rumpfolt JA, Broom HR, Doyle CM, Bouvignies G, Meiering EM, Kay LE (2015) Thermal fluctuations of immature SOD1 lead to separate folding and misfolding pathways. *Elife* 4: e07296
- Shaw BF, Lelie HL, Durazo A, Nersissian AM, Xu G, Chan PK, Gralla EB, Tiwari A, Hayward LJ, Borchelt DR *et al* (2008) Detergent-insoluble aggregates associated with amyotrophic lateral sclerosis in transgenic mice contain primarily full-length, unmodified superoxide dismutase-1. *J Biol Chem* 283: 8340–8350
- Shibata N, Hirano A, Kobayashi M, Siddique T, Deng HX, Hung WY, Kato T, Asayama K (1996) Intense superoxide dismutase-1 immunoreactivity in intracytoplasmic hyaline inclusions of familial amyotrophic lateral sclerosis with posterior column involvement. *J Neuropathol Exp Neurol* 55: 481–490
- Siegt A, Rankovic M, Favretto F, Ukmar-Godec T, Strohäker T, Becker S, Zweckstetter M (2021) Interplay between tau and α -synuclein liquid-liquid phase separation. *Protein Sci* 30: 1326–1336
- Singh V, Xu L, Boyko S, Surewicz K, Surewicz WK (2020) Zinc promotes liquid-liquid phase separation of tau protein. *J Biol Chem* 295: 5850–5856
- Skinner JJ, Wang S, Lee J, Ong C, Sommesse R, Sivaramakrishnan S, Koelmel W, Hirschbeck M, Schindelin H, Kisker C *et al* (2017) Conserved salt-bridge competition triggered by phosphorylation regulates the protein interactome. *Proc Natl Acad Sci U S A* 114: 13453–13458
- Souza PCT, Thallmair S, Marrink SJ, Mera-Adasme R (2019) An allosteric pathway in copper, zinc superoxide dismutase unravels the molecular mechanism of the G93A amyotrophic lateral sclerosis-linked mutation. *J Phys Chem Lett* 10: 7740–7744
- Strange RW, Antonyuk S v, Hough MA, Doucette PA, Valentine JS, Hasnain SS (2006) Variable metallation of human superoxide dismutase: atomic resolution crystal structures of Cu-Zn, Zn-Zn and as-isolated wild-type enzymes. *J Mol Biol* 356: 1152–1162
- Sun Y, Day RN, Periasamy A (2011) Investigating protein-protein interactions in living cells using fluorescence lifetime imaging microscopy. *Nat Protoc* 6: 1324–1340
- Timr S, Gnut D, Ebbinghaus S, Sterpone F (2020) The unfolding journey of superoxide dismutase 1 barrels under crowding: atomistic simulations shed light on intermediate states and their interactions with Crowders. *J Phys Chem Lett* 11: 4206–4212
- Tokuda E, Nomura T, Ohara S, Watanabe S, Yamanaka K, Morisaki Y, Misawa H, Furukawa Y (2018) A copper-deficient form of mutant Cu/Zn-superoxide dismutase as an early pathological species in amyotrophic lateral sclerosis. *Biochim Biophys Acta Mol Basis Dis* 1864: 2119–2130
- Vassall KA, Stubbs HR, Primmer HA, Tong MS, Sullivan SM, Sobering R, Srinivasan S, Briere L-AK, Dunn SD, Colón W *et al* (2011) Decreased stability and increased formation of soluble aggregates by immature superoxide dismutase do not account for disease severity in ALS. *Proc Natl Acad Sci U S A* 108: 2210–2215
- Vega M, Cascella R, Chen SW, Fusco G, De Simone A, Dobson CM, Cecchi C, Chiti F (2019) The toxicity of misfolded protein oligomers is independent of their secondary structure. *ACS Chem Biol* 14: 1593–1600
- Vilasi S, Sarcina R, Maritato R, de Simone A, Irace G, Sirangelo I (2011) Heparin induces harmless fibril formation in amyloidogenic W7FW14F apomyoglobin and amyloid aggregation in wild-type protein *In vitro*. *PLoS ONE* 6: e22076
- Wang Q, Johnson JL, Agar NYR, Agar JN (2008) Protein aggregation and protein instability govern familial amyotrophic lateral sclerosis patient survival. *PLoS Biol* 6: 1508–1526
- Wegmann S, Eftekhazadeh B, Tepper K, Zoltowska KM, Bennett RE, Dujardin S, Laskowski PR, MacKenzie D, Kamath T, Commis C *et al* (2018) Tau protein liquid-liquid phase separation can initiate tau aggregation. *EMBO J* 37: 1–21
- Wheeler JR, Matheny T, Jain S, Abrisch R, Parker R (2016) Distinct stages in stress granule assembly and disassembly. *Elife* 5: e18413
- Wright GS, Antonyuk SV, Kershaw NM, Strange RW, Samar Hasnain S (2013) Ligand binding and aggregation of pathogenic SOD1. *Nat Commun* 4: 1–10
- Yang F, Wang H, Logan DT, Mu X, Danielsson J, Oliveberg M (2018) The cost of long catalytic loops in folding and stability of the ALS-associated protein SOD1. *J Am Chem Soc* 140: 16570–16579
- Zhang Z, Liu X, Yan K, Tuckerman ME, Liu J (2019) Unified efficient thermostat scheme for the canonical ensemble with holonomic or isokinetic constraints via molecular dynamics. *J Phys Chem A* 123: 6056–6079
- Zhu C, Beck MV, Griffith JD, Deshmukh M, Dokholyan NV (2018) Large SOD1 aggregates, unlike trimeric SOD1, do not impact cell viability in a model of amyotrophic lateral sclerosis. *Proc Natl Acad Sci U S A* 115: 4661–4665
- Zittin Potter S, Zhu H, Francis Shaw B, Rodriguez JA, Doucette PA, Hui Sohn S, Durazo A, Faull KF, Butler Gralla E, Nersissian AM *et al* (2007) Binding of a single zinc ion to one subunit of copper-zinc superoxide dismutase Apoprotein substantially influences the structure and stability of the entire Homodimeric protein. *J Am Chem Soc* 129: 4575–4583

The metal cofactor zinc and interacting membranes modulate SOD1 conformation-aggregation landscape in an in vitro ALS model

Achinta Sannigrahi^{1†}, Sourav Chowdhury^{2†}, Bidisha Das^{1,3†}, Amrita Banerjee⁴, Animesh Halder⁵, Amaresh Kumar⁶, Mohammed Saleem⁶, Athi N Naganathan⁷, Sanat Karmakar⁵, Krishnananda Chattopadhyay^{1,3*}

¹Structural Biology & Bio-Informatics Division, CSIR-Indian Institute of Chemical Biology, Kolkata, India; ²Chemistry and Chemical Biology, Harvard University, Cambridge, United States; ³Academy of Scientific and Innovative Research (AcSIR), CSIR- Human Resource development Centre Campus, Ghaziabad, India; ⁴Hiralal Mazumdar Memorial College for Women, Kolkata, India; ⁵Department of Physics, Jadavpur University, Kolkata, India; ⁶School of Biological Sciences, National Institute of Science Education and Research (NISER), Bhubaneswar, India; ⁷Department of Biotechnology, Bhupat & Jyoti Mehta School of Biosciences, Indian Institute of Technology Madras, Chennai, India

Abstract Aggregation of Cu-Zn superoxide dismutase (SOD1) is implicated in the motor neuron disease, amyotrophic lateral sclerosis (ALS). Although more than 140 disease mutations of SOD1 are available, their stability or aggregation behaviors in membrane environment are not correlated with disease pathophysiology. Here, we use multiple mutational variants of SOD1 to show that the absence of Zn, and not Cu, significantly impacts membrane attachment of SOD1 through two loop regions facilitating aggregation driven by lipid-induced conformational changes. These loop regions influence both the primary (through Cu intake) and the gain of function (through aggregation) of SOD1 presumably through a shared conformational landscape. Combining experimental and theoretical frameworks using representative ALS disease mutants, we develop a 'co-factor derived membrane association model' wherein mutational stress closer to the Zn (but not to the Cu) pocket is responsible for membrane association-mediated toxic aggregation and survival time scale after ALS diagnosis.

*For correspondence:

krish@iicb.res.in

[†]These authors contributed equally to this work

Competing interests: The authors declare that no competing interests exist.

Funding: See page 25

Received: 25 July 2020

Accepted: 01 April 2021

Published: 07 April 2021

Reviewing editor: Hannes Neuweiler, University of Würzburg, Germany

© Copyright Sannigrahi et al. This article is distributed under the terms of the [Creative Commons Attribution License](#), which permits unrestricted use and redistribution provided that the original author and source are credited.

Introduction

The aggregation of SOD1 is believed to be one of the chief causative factors behind the lethal motor neuron disease, amyotrophic lateral sclerosis (ALS) (*Shaw and Valentine, 2007*). Although more than 140 SOD1 mutations have been reportedly associated with ALS, there is no correlation between the stability (and aggregation) of these mutations and their disease manifestations. SOD1 aggregation has been investigated extensively in vitro by altering the solution conditions, such as temperature, pH, the presence of metal chelators, and the reduction of disulfide linkages (*Bush, 2002; Niwa, 2007; Rodriguez et al., 2005*). The results of these studies clearly suggest that the aggregation of SOD1 is heterogeneous containing multiple steps, which is presumably the reason behind the lack of a structural understanding of aggregation processes (*Pasinelli et al., 2004; Tomik et al., 2005*).

eLife digest Amyotrophic lateral sclerosis, or ALS, is an incurable neurodegenerative disease in which a person slowly loses specialized nerve cells that control voluntary movement. It is not fully understood what causes this fatal disease. However, it is suspected that clumps, or aggregates, of a protein called SOD1 in nerve cells may play a crucial role.

More than 140 mutations in the gene for SOD1 have been linked to ALS, with varying degrees of severity. But it is still unclear how these mutations cause SOD1 aggregation or how different mutations influence the survival rate of the disease. The protein SOD1 contains a copper ion and a zinc ion, and it is possible that mutations that affect how these two ions bind to SOD1 influences the severity of the disease.

To investigate this, Sannigrahi, Chowdhury, Das et al. genetically engineered mutants of the SOD1 protein which each contain only one metal ion. Experiments on these mutated proteins showed that the copper ion is responsible for the protein's role in neutralizing harmful reactive molecules, while the zinc ion stabilizes the protein against aggregation. Sannigrahi et al. found that when the zinc ion was removed, the SOD1 protein attached to a structure inside the cell called the mitochondria and formed toxic aggregates.

Sannigrahi et al. then used these observations to build a computational model that incorporated different mutations that have been previously associated with ALS. The model suggests that mutations close to the site where zinc binds to the SOD1 protein increase disease severity and shorten survival time after diagnosis. This model was then experimentally validated using two disease variants of ALS that have mutations close to the sites where zinc or copper binds.

These findings still need to be tested in animals and humans to see if these mechanisms hold true in a multicellular organism. This discovery could help design new ALS treatments that target the zinc binding site on SOD1 or disrupt the protein's interactions with the mitochondria.

WT SOD1 contains Cu^{2+} (Cu) and Zn^{2+} (Zn) as cofactors. It has been established that Cu is responsible for the primary function of SOD1 (the dismutase activity), and cell membrane acts as a scaffold in the process of Cu transfer to apo-SOD1 (metal free non-functional protein) through a Cu delivery chaperone (CCS) (Culotta et al., 1997). Previous studies have found noticeable presence of SOD1 in human serum lipoproteins, mainly in LDL and HDL, hinting at a possible protective role of SOD1 against the lipid peroxidation (Mondola et al., 2016). It has also been noted that SOD1 has a physiological propensity to accumulate near the membranes (Ilieva et al., 2009) of different cellular compartments, including mitochondria, endoplasmic reticulum (ER), and Golgi apparatus (Manfredi and Kawamata, 2016). In addition, computational studies have shown that the electrostatic loop (loop VII, residues 121–142) and Zn-binding loop (loop IV, residues 58–83) promote membrane interaction of apo-SOD1 initiating the aggregation process (Chng and Strange, 2014). Membrane binding induced aggregation of SOD1 has also been shown experimentally both in vitro and inside cells (Hervias et al., 2006; Yamanaka et al., 2008; Choi et al., 2011). Inclusions of SOD1 have been detected in the inter-membrane space of mitochondria originating from the spinal cord (Mondola et al., 2016).

The above results can be reconciled by suggesting that cell membrane can play crucial roles not only in shaping up the primary function of the protein, but also in defining its aggregation process of generating fibrillar and non-fibrillar aggregates (the gain of function), with the loops IV and VII contributing critically to both processes. We hypothesize that (1) the induction of metal cofactors for the stabilization of loop IV and VII, membrane interaction, and SOD1 aggregation would be some of the crucial elements in defining the overlapping folding-aggregation landscape of SOD1; (2) metal pocket perturbation by mutational stresses (as in disease variants) would modulate membrane association and facilitate aggregation, and (3) the difference in aggregate morphology as a result of differential membrane interaction may contribute to the variation in cellular toxicity observed in ALS.

In this paper, we investigated the above hypothesis by studying how different structural elements (i.e. co-ordination of individual metals, membrane association, and the location of mutations) attenuate the toxic gain of function of SOD1. An effective understanding of the role of individual metals (Cu and Zn) would require studying SOD1 variants containing only one metal (Cu or Zn) in addition

to a variant that contains none. We have therefore prepared an apo (metal free) protein, which serves the latter purpose. For the former, we have generated two single metal containing mutants of SOD1, viz. H121F (only Zn, no Cu) and H72F (only Cu, no Zn), which are situated near the key loop VII (H121F) and loop IV (H72F) at the protein structure (Figure 1a).

Using computational analysis based on a statistical mechanical model and detailed in vitro experiments, we propose here a 'Co-factor derived membrane association model' of SOD1 aggregation and its possible implication in ALS. We demonstrate that differential metal binding and membrane assisted conformational changes can work in concert to attenuate the rate and propensity of aggregation. While apo (no metal) protein and H72F mutant (no Zn) experience strong membrane interaction, the WT (both metals) protein and H121F (no Cu) mutant do not show significant binding. We further find that membrane-induced aggregates of H72F and apo protein showed significantly higher toxicity in terms of cell death and model membrane deformation when compared to WT and H121F mutant. We finally check the validity of this model to ALS using computational and experimental studies. For the computational validation, we show, using 15 ALS disease mutants, that the distance between the mutation site and Zn correlates well with the membrane binding energy and patient survival time after disease diagnosis, while Cu site does not seem to have any prominent role. For the experimental study, we use two well-studied disease mutants (G37R where mutational site is close to the Cu pocket and I113T where mutational site is near Zn pocket) to show that the model accounts well for their membrane binding/aggregation, correlating well with their disease onset phenotypes. This model puts forward a mechanism that Zn pocket destabilization (either by metal content variation or by mutational stress near Zn center) is the driving force behind the toxic gain of function of SOD1 mediated by the process of membrane association.

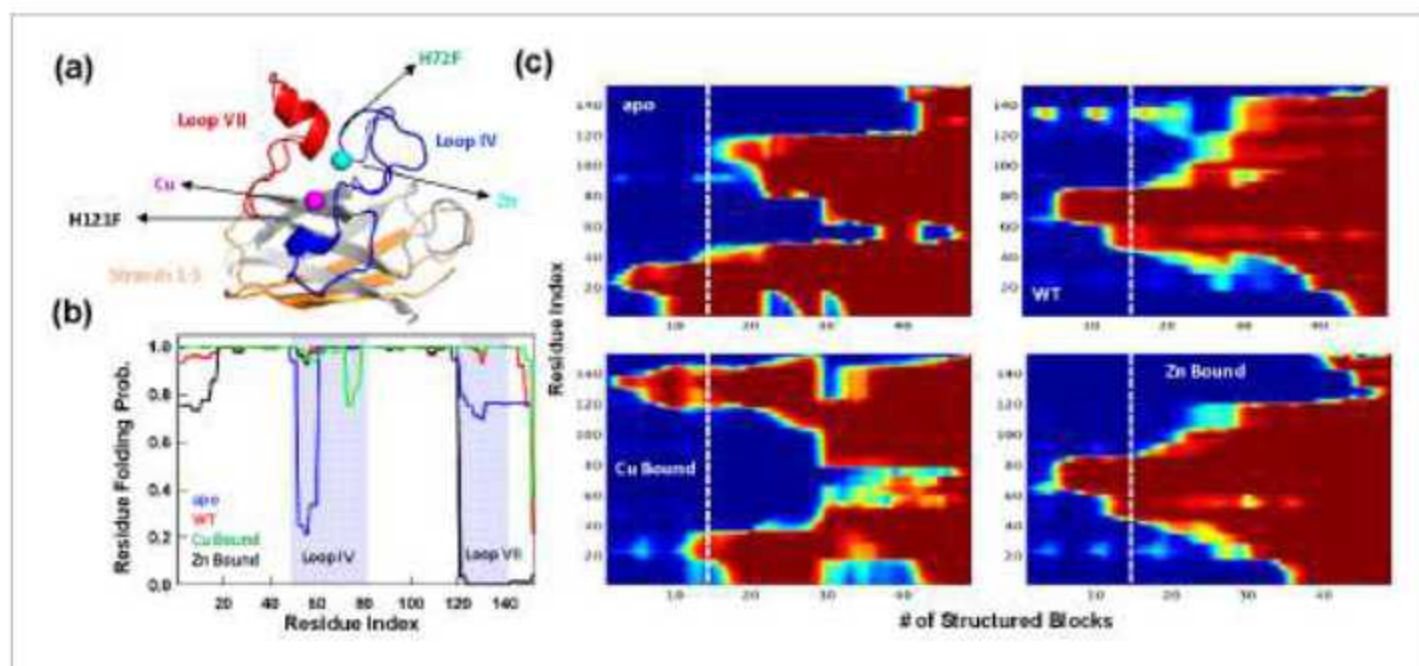


Figure 1. Statistical mechanical modeling of SOD1 folding mechanism. (a) Cartoon representation of SOD1 monomer highlighting the various structural elements. The positions of the mutation for H121F and H72F have been arrow marked. (b) Residue folding probability as a function of residue index for the different variants of SOD1 as predicted by the bWSME model. Note that WT represents the variant in which both the metallic cofactors are bound. (c) Average folding probabilities colored in the spectral scale going from 0 (dark blue) to 1 (dark red) as a function of the reaction coordinate, number of structured blocks. The vertical white dashed line signals the parts of the protein that fold first. For example, it can be seen that residues 1–40 fold early in the apo SOD1 (dark red) when compared to WT where residues 40–80 fold first.

The online version of this article includes the following figure supplement(s) for figure 1:

Figure supplement 1. Aggregation prone regions as a function of sequence from AGGRESCAN software (<http://bioinf.uab.es/aggrescan/>).

Results

Statistical mechanical modeling of SOD1 folding mechanism hints at aggregation origins

The large size of SOD1 (151 residues) precludes a detailed characterization of the conformational landscape, the role of ions in determining the stability-folding mechanism, and the effect of numerous mutations via all-atom simulation methods. To overcome this challenge and to obtain a simple physical picture of how the energetics of folding is governed by metal ions, we resort to constructing the folding landscape of reduced SOD1 variants through the statistical mechanical Wako-Saitō-Muñoz-Eaton (WSME) model (see Materials and methods for model description and parametrization) (Wako and Saitō, 1978; Muñoz and Eaton, 1999). Here, we employ the bWSME model where stretches of three consecutive residues are considered as a block (b) that reduces the total number of microstates from 42.7 million to just ~450,000 (Gopi et al., 2019).

The model, however, incorporates contributions from van der Waals interactions, simplified solvation, Debye-Hückel electrostatics, excess conformational entropy for disordered residues, and restricted conformational freedom for proline residues (Naganathan, 2012; Rajasekaran et al., 2016). The predicted average folding path of SOD1 WT (with both Cu and Zn bound) highlights that the folding is initiated around the metal binding regions with early folding of the loop IV (nucleated by Zn) in the unfolded well and aided by flickering structure in the electrostatic loop (loop VII, nucleated by Cu). The rest of the structure coalesces around this initial folding site leading to the native state. This folding mechanism is very similar to that proposed earlier via detailed kinetic studies (Leinartaitė et al., 2010). In the absence of metal ions, the apo variant folds through an alternate pathway wherein the folding is nucleated through the first three strands (residues 1–40) following which the rest of the structure folds, recapitulating the results of single-molecule experiments (Figure 1; Sen Mojumdar et al., 2017). It is important to note that the first three strands exhibit higher aggregation propensity as predicted from different computational servers (Figure 1—figure supplement 1). Interestingly, the folding mechanism of the Zn-bound SOD1 (with no Cu bound) is similar to that of the WT hinting that Zn coordination promotes proper folding. On the other hand, the folding mechanism of the Cu-bound SOD1 (in the absence of Zn) is similar to that of apo-SOD1 with additional folding probability in the region around the electrostatic loop. Taken together, the statistical modeling highlights how the absence of metals and particularly the absence of Zn (or mutations that affect Zn binding and not Cu binding) alters the folding mechanism by populating partially structured states involving beta strands in the unfolded well thus possibly increasing the chances of aggregation. Importantly, the model provides multiple testable predictions on the differential roles of Zn and Cu, which we address below via experiments.

Cu-deficient H121F behaves like WT SOD1, whereas zn-deficient H72F behaves like apo

We have recently shown that the mutants H121F and H72F contain negligible Cu and Zn, respectively, while the apo protein is completely devoid of metal (Chowdhury et al., 2019). We validated this further using atomic absorption spectroscopy (Table 1) and activity measurements (Figure 2—figure supplement 1). Guanidinium-induced equilibrium unfolding transitions of H121F and H72F were found to be similar (Figure 2—figure supplement 2). We used steady-state tryptophan fluorescence, far UV CD, and FTIR spectroscopy to characterize these different proteins. SOD1 is a single tryptophan protein (Trp32), in which the tryptophan residue has been shown to be partially

Table 1. Metal contents (Cu and Zn) in WT and other mutants (H121F, H72F, and apo) as obtained from atomic absorption spectroscopy.

Protein forms	Cu content	Zn content
WT	4.5 μ M	3.9 μ M
H121F	<1 μ M	3.8 μ M
H72F	4.1 μ M	<1.2 μ M
apo	<0.5 μ M	<0.25 μ M

buried (Muneeswaran *et al.*, 2014). The role of Trp32 within the sequence segment (Lomize *et al.*, 2012) KVGSIKGL (Gohil and Greenberg, 2009) of high aggregation propensity has been investigated before (Taylor *et al.*, 2007). We found that the formation of apo form resulted in a large shift in Trp32 emission maximum (332 nm for WT protein and 350 nm for apo protein) (Figure 2a). In contrast, other two mono-metallated variants (H121F and H72F) exhibited fluorescence emission maxima at wavelengths, which were intermediate between the WT and apo proteins (342 nm for H121F and 345 nm for H72F) (Figure 2a). Next, we performed acrylamide-quenching experiments to measure the solvent surface exposure of Trp32 for all variants. The values (Table 2) of the Stern-Volmer constant (K_{sv}) were determined using a straight line fit, as shown in Figure 2—figure supplement 3. K_{sv} for WT ($6.8 \pm 0.1 \text{ M}^{-1}$) was significantly lower than that of apo SOD1 ($14.3 \pm 0.1 \text{ M}^{-1}$). Steady-state fluorescence maxima in combination with acrylamide quenching data suggested an appreciable conformational alteration in going from the WT to the apo form. Interestingly, Zn-starved H72F mutant showed higher K_{sv} compared to Cu-starved H121F mutant (Figure 2—figure supplement 3, Table 2).

Far-UV circular dichroism (CD) spectra for WT and apo protein were in line with earlier observations (Figure 2—figure supplement 4; Banci *et al.*, 2007). Specifically, we found a slight broadening in the far UV CD spectrum of the apo protein when compared to the WT. In agreement with steady-state fluorescence data, the far UV-CD spectrum of the Zn-deficient H72F protein was found to be similar to the apo variant, while the WT- and Cu-deficient H121F variant displayed similar spectra. We then used FT-IR spectroscopy to complement far-UV CD results and to obtain a preliminary estimate of the secondary structure contents of the protein variants, using amide-I FTIR spectral region. The carbonyl ($\text{C}=\text{O}$) stretching vibrations at amide-I region provides information related to the secondary structure (beta sheet 1633–1638, alpha helix 1649–1656, disorder and turns and loops 1644 and 1665–1672 cm^{-1}). The analyses of the FT-IR data were carried out using published method using two steps (Yang *et al.*, 2015; Kong and Yu, 2007; Bandyopadhyay *et al.*, 2021). First, the peak positions were assigned using the double derivatives of the FT-IR data for all protein variants (Figure 2—figure supplement 5 shows the representative double derivative plot of WT SOD1 in the absence of lipid). The peak positions were selected from the minima of the secondary derivatives of the FT-IR absorbance data. In the second step, selected peak positions thus determined were used for the fitting of the FT-IR raw data using Gaussian distributions analyses. Analysis of the secondary structure of WT protein (Figure 2b) showed the presence of 10% alpha helix, 38% beta sheet, and 52% turns and loops including disordered stretches. The percentage of the secondary structure determined from the FT-IR analysis was found to be consistent with the data obtained from the crystal structure (PDB 4BCY with 11% alpha helix, 40% beta sheet, and 49% turns and loops), thus validating our method (Danielsson *et al.*, 2013). FT-IR data showed a decrease in beta sheet content (from 38% to 31%) as apo protein (Figure 2c) formed. In contrast, the behavior of H72F mutant (Figure 2—figure supplement 6a, beta sheet content of 32%) was found to be similar to the apo protein, while H121F mutant (Figure 2—figure supplement 6b, beta sheet content of 37%) remained similar to WT protein. The percentage of secondary structure elements of all protein variants are shown in Figure 2d.

Zn-deficient SOD1 shows higher membrane association compared to the Cu-deficient and WT proteins

To obtain a preliminary understanding of the possible membrane binding sites of SOD1, we resorted to computational techniques using 'Orientation of protein in membrane' tool (Lomize *et al.*, 2012), which predicted weak interaction of WT on membrane surface (Figure 2—figure supplement 7a). In contrast, the same calculation predicted higher binding affinity of apo protein with the membrane (Figure 2e). When we used ITASSER-modeled structures, the computed values of $\Delta G_{\text{transfer}}$ (free energy change of protein transfer from bulk to the membrane) was found to be substantially higher for the apo ($-2.6 \text{ kcal mol}^{-1}$) when compared to the WT protein ($-1.2 \text{ kcal mol}^{-1}$). When we used the crystal structure of the WT protein, $\Delta G_{\text{transfer}}$ calculation modeling yielded similar results for the WT protein ($-0.9 \text{ kcal mol}^{-1}$). To probe protein-lipid binding constants experimentally (K_a, M^{-1}), we used fluorescence correlation spectroscopy (FCS). FCS monitors diffusional and conformational dynamics of fluorescently labeled biomolecules at single-molecule resolution (Chattopadhyay *et al.*, 2002). For FCS experiments, we labeled the cysteine residues of all the SOD1 variants using Alexa-488-maleimide. Figure 2f shows a schematic diagram of how the labeled proteins and protein-lipids

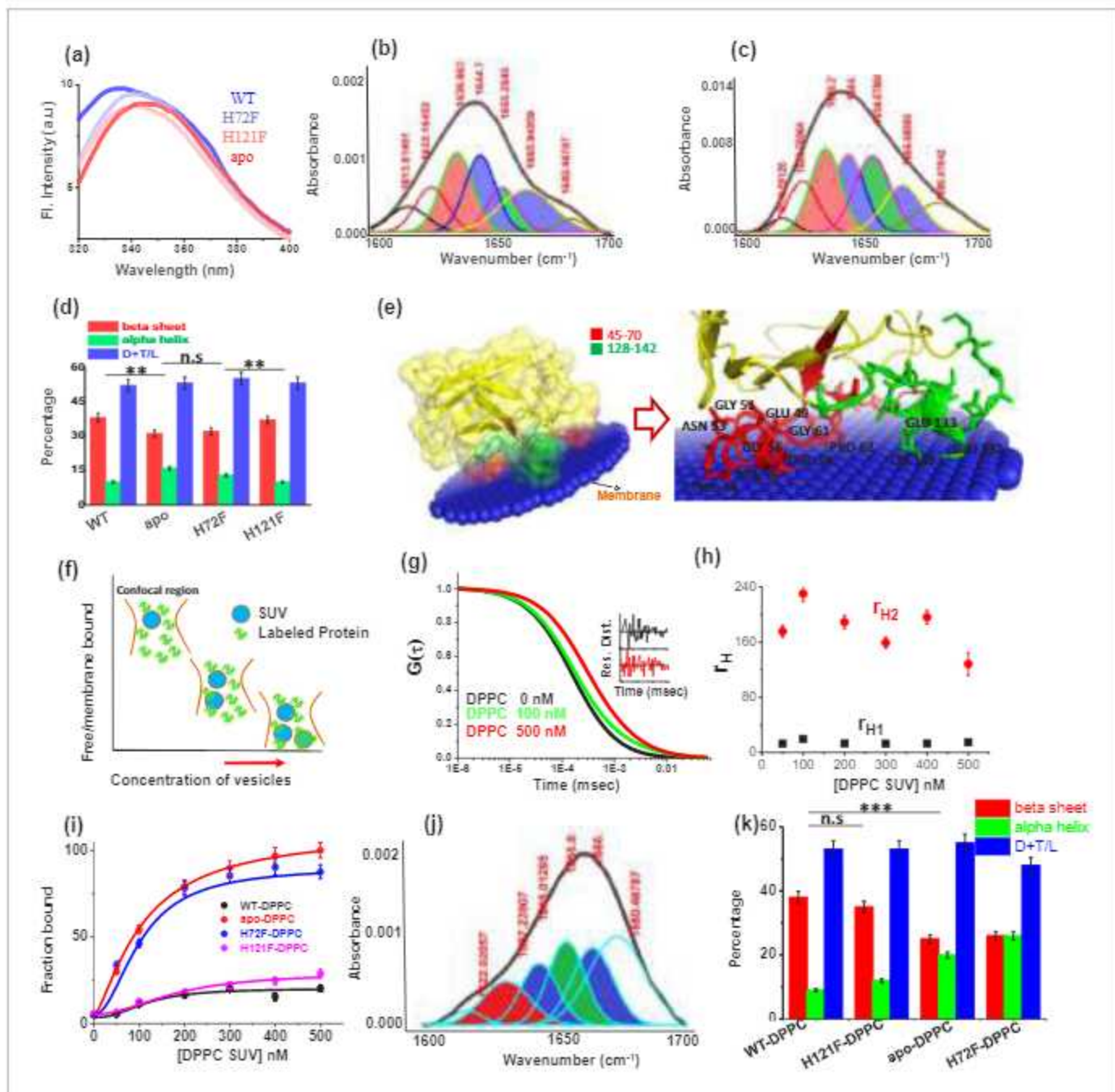


Figure 2. Structural characterization of SOD1 mutants and membrane association. (a) Steady-state tryptophan fluorescence spectra of WT, apo, and other two metal mutants (H121F and H72F). The WT displays an emission maximum at 332 nm, whereas the apo variant shows a red-shifted spectrum with the emission maximum at 350 nm. On the other hand, H121F and H72F show emission maxima at intermediate wavelengths. Deconvoluted FTIR spectral signatures of (b) WT and (c) apo. Red contour ($\sim 1637\text{ cm}^{-1}$) indicates beta sheet; blue color contour stands for disorder (1644 cm^{-1}) and loops and turns ($\sim 1667\text{ cm}^{-1}$); green contour represents alpha helical character. All these secondary signatures were obtained by considering the amide-I spectra, which arises due to carbonyl frequency ($C=O$). (d) Percentage of different secondary structural components in WT, apo, H121F, and H72F are shown in this figure. n.s. denotes nonsignificant change, while ** stands for significant change with $p\text{-value} < 0.01$. Error bars indicate the standard deviation of the data, which were obtained from triplicate experiments. Here, D + T/L stands for Disorder + Turns/Loops. (e) The membrane association of the apo protein as suggested by the OPM calculations. The membrane association of apo protein through the stretches 45–70 and 128–142 has been evaluated from the calculations. The residues which are involved in binding with membrane (Thr54,58, Ala54, Gly56,61, Pro62, Asn53, Glu49, Lys136, Glu132,133) are mentioned. (f) A schematic representation regarding the membrane binding experiments through FCS which suggests that with increasing concentration of DPPC small unilamellar vesicles (SUVs), the alexa labeled free monomeric protein populations (fast component of diffusion model) decreases with concomitant increase in the membrane bound labeled protein that is the slow component. (g) The correlation functions of alexa

Figure 2 continued on next page

Figure 2 continued

488 maleimide labeled apo SOD1 in the absence (black) and presence of DPPC SUVs (red) where DPPC concentration was kept 500 nM. The green correlation curve corresponds to an intermediate DPPC concentration (100 nM). The inset shows the residual distributions of the correlation curves. (h) The hydrodynamic radii of free alexa 488-apo SOD1 and membrane bound labeled apo SOD1 were plotted against the concentrations of added DPPC SUVs. The average hydrodynamic radius of fast component that is free monomeric apo SOD1 (r_{11}) was found to be 13.5 Å, whereas the average radius for slow membrane bound protein molecule (r_{12}) was found to be 170 Å. The change of r_{11} and r_{12} with increasing DPPC SUV concentration remains invariant. (i) Percentage populations of membrane bound alexa-labeled protein variants were plotted against the concentrations of DPPC SUVs added to evaluate the binding affinities of the protein variants towards membranes. (j) Deconvoluted FTIR spectra of apo in membrane (DPPC SUV) bound condition. (k) Percentage of different secondary structural components in WT, apo, H121F, and H72F in the presence of DPPC SUVs are shown in this figure. n.s denotes nonsignificant change, while *** stands for significant change with p -value < 0.001.

The online version of this article includes the following source data and figure supplement(s) for figure 2:

Source data 1. Structural characterization and membrane binding of SOD1 protein variants.

Figure supplement 1. Activity assay (pyrogallol auto-oxidation) for WT and other metal mutants of SOD1.

Figure supplement 2. Equilibrium unfolding transitions of H121F and H72F mutants using guanidinium hydrochloride as chemical denaturant.

Figure supplement 3. Acrylamide quenching experiments for the different variants.

Figure supplement 4. Far UV-CD spectra of the SOD1 variants.

Figure supplement 5. Second derivative of the FT-IR data obtained with WT SOD1.

Figure supplement 6. FTIR assessment of the H72F and H121F mutant.

Figure supplement 7. Membrane binding and conformational changes of the protein variants.

complex would behave inside the confocal volume. Using FCS we determined the correlation functions using 50 nM Alexa488Maleimide protein in the presence of increasing concentration of DPPC small unilamellar vesicles (SUVs) (Figure 2g showed the typical correlation functions of alexa labeled apo SOD1 in absence and presence of 100 nM and 500 nM DPPC SUVs). We fit the correlation functions using a two component diffusion model and the goodness of the fit was established using the randomness of the residual distribution. In this model, the fast and slow diffusing components corresponded to the free (with r_{11} 13.5 Å) and lipid bound protein (r_{12} 170 Å) respectively (Figure 2h). With increasing DPPC SUV concentration, the percentage of slow component increased (Figure 2f), which occurred at the expense of the fast component, and a sigmoidal fit of either of these components yield the values of K_{av} , which showed that the binding affinities followed the trend: apo \geq H72F > H121F > WT (Figure 2i, Table 3). Since FCS experiments required the use of labeled proteins in which the presence of bulky fluorescence dye can potentially influence the results, we complemented FCS binding data by measuring the tryptophan fluorescence of the SOD1 variants with increasing concentrations of DPPC SUVs. From the gradual enhancement of tryptophan fluorescence due to lipid binding, we calculated the binding affinities of all the protein variants towards membrane which showed comparable binding constants as obtained from our FCS experiments (Figure 2—figure supplement 7b,c). We then measured the Stern–Volmer constants using acrylamide quenching experiments of Trp32 fluorescence with protein variants in the absence (K_{sv}) and presence of (K_{svm}) membrane. The parameter K_{sv}/K_{svm} was found maximum for the apo protein, and minimum for WT (Figure 2—figure supplement 7d, Table 2). H121F and H72F variants behaved like WT and apo protein, respectively. As observed by FT-IR, DPPC binding resulted in no or minimum change in conformation for WT and H121F proteins (Figure 2—figure supplement 7e,f), while a large decrease in beta sheet content with simultaneous rise in non-beta content, specifically alpha helical

Table 2. The values of Stern–Volmer quenching constants for Trp 32 residue of all the protein variants in the absence (K_{sv} , M^{-1}) and presence of DPPC SUVs (K_{svm} , M^{-1}) as obtained from acrylamide quenching for WT SOD1 and all the mutants including apo SOD1.

Proteins	K_{sv}	K_{svm}	K_{sv}/K_{svm}
WT SOD1	6.8 ± 0.1	5.7 ± 0.2	1.19
H121F	8.0 ± 0.1	6.3 ± 0.1	1.26
H72F	12.7 ± 0.3	7.0 ± 0.2	1.82
apo SOD1	14.3 ± 0.1	7.6 ± 0.2	1.88

Table 3. Binding constants (K_a, M^{-1}) of the protein variants with model DPPC SUVs as obtained from the FCS study for WT SOD1 and all the mutants.

Systems	Association constants (K_a, M^{-1})
WT SOD1 + DPPC SUV	$(4.1 \pm 0.1) \times 10^6$
H121F + DPPC SUV	$(5.2 \pm 0.2) \times 10^6$
H72F + DPPC SUV	$(9.6 \pm 0.4) \times 10^7$
apo + DPPC SUV	$(9.8 \pm 0.1) \times 10^7$
G37R-DPPC SUV	$(2.2 \pm 0.3) \times 10^6$
I113T-DPPC SUV	$(8.8 \pm 0.2) \times 10^6$

content, was observed for the apo protein and H72F mutant (*Figure 2j,k* *Figure 2—figure supplement 7g*).

Lipid vesicles accelerate aggregation kinetics of apo and zn-deficient mutants

Aggregation kinetics of WT, apo, and the mutant SOD1 in their TCEP reduced states were studied systematically both in the absence and in the presence of DPPC. A typical protein membrane ratio of 1:2 was maintained for all measurements involving membranes. For the initial assessment of the aggregation kinetics, the fluorescence intensity enhancement of amyloid marker Thioflavin T (ThT) was monitored. ThT is known to bind to protein aggregates with cross beta structure giving rise to a large increase in its fluorescence intensity. From the ThT fluorescence assay, we found that the WT protein does not aggregate, both in the absence or in the presence of membrane (*Figure 3a,b*). For the H121F variant in the absence of membrane, we found a small and slow enhancement of ThT fluorescence and the profile remained unchanged when we added the membrane (*Figure 3a,c*). In contrast, for apo and H72F variants, ThT assay showed large fluorescence increase and the kinetics followed typical sigmoidal patterns. The addition of membrane increased the rate of aggregation for both variants and a large decrease in the lag times. When compared between the apo and H72F variants, we found that the rate of aggregation is higher (i.e. with less lag time) for the apo protein (*Figure 3a,b,c* *Table 4*).

We then imaged using atomic force microscopy (AFM) the aggregates collected from the plateau regions of the aggregation kinetics (at a time point when the fluorescence of ThT was maximum [saturated] and did not change). Protein (P) aggregates will be denoted by P_{agg} , and P_{aggm} to indicate if they are formed in the absence or presence of membranes respectively. For example, the aggregates of WT in the absence and presence of membranes would be denoted by WT_{agg} , and WT_{aggm} , respectively. AFM imaging also showed that in the absence of membrane, WT and H121F did not form aggregates, fibrillar, or otherwise (*Figure 3—figure supplement 1*), while large fibrillar aggregates were found to form with apo (*Figure 3d*) and H72F mutant (*Figure 3—figure supplement 1*). The average size of the fibrillar apo_{agg} was found to be 1.8–2 μm with an average height of 20 nm. H72F_{agg} showed similar morphology (*Figure 3—figure supplement 1*). Significant morphological differences were noticed for the aggregates of apo and H72F variants, in the absence (*Figure 3d,e*, *Figure 3—figure supplement 1*) and the presence of the membrane. The apo_{aggm} appeared to exhibit network of thin aggregates (the average size was found to be 700–800 nm with an average height of 6–8 nm) which were found to be connected by the spherical DPPC vesicles (*Figure 3e*, inset; *Figure 3f*). To understand the effect of curvature on membrane binding and aggregation, we performed the binding experiments with H72F mutant using liposomes of different curvatures. We used DPPC SUVs (diameter ~78 nm), LUVs (diameter ~140 nm) and GUVs (~20 μm) for this study. Our results showed that with increasing curvature of the DPPC lipid vesicles, binding, and aggregation of H72F increased that is fibril formation rate and extents were found to be highest in the presence of SUVs and moderate for LUVs and lowest for GUVs (*Figure 3—figure supplement 2a,b*). To investigate the effect of H72F mutant toward curvature induction in GUVs, we studied the aggregation of H72F in the presence of GUVs and the final point aggregates were imaged through a transmission electron microscope. We found that as a result of the incubation with H72F, the size of the GUVs reduced many folds starting from an average size of 5–10 μm to about 1–2 μm .

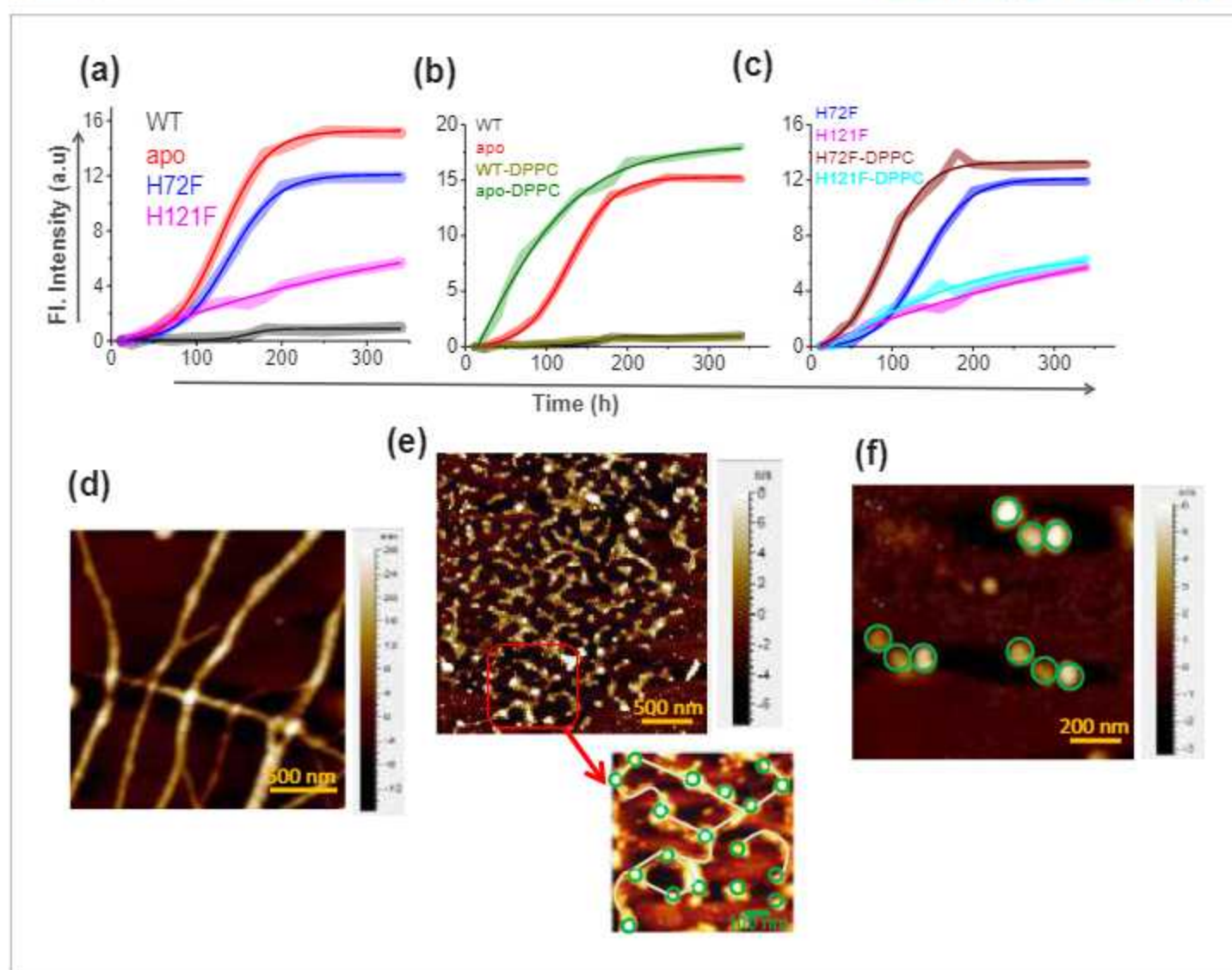


Figure 3. Aggregation of WT SOD1 and its mutants and membrane effects. (a) ThT fluorescence (at 484 nm) for the protein variants under reducing conditions to monitor the kinetics of aggregation. (b) Time-dependent increase in ThT fluorescence intensity of WT and apo both in the absence and in the presence of membrane (DPPC SUVs were used here as membrane). (c) Same as (b) but for H72F and H121F. Atomic force microscopy (AFM) images of the aggregates of apo SOD1 in the absence (d) and presence (e) of DPPC SUVs. These AFM images were taken at the plateau of the ThT aggregation curves. AFM images of apo_{agg} showed linear fibrillar aggregates with an average size 1.8–2 μ m. In contrast in the presence of membrane (apo_{agg}), we found network of small fibrils, which were connected by DPPC vesicles (as drawn in the inset of e). It may be noted that the size and height (average diameter is 70 nm and average height is 7 nm) of the connecting spherical objects are similar to (f) AFM micrograph of the control DPPC SUVs, which showed distinct membrane structures with an average size of 70–90 nm.

The online version of this article includes the following source data and figure supplement(s) for figure 3:

Source data 1. Aggregation and effect of membrane curvature and composition on the aggregation behavior of SOD1 protein variants.

Figure supplement 1. AFM topographic images of the aggregates of different protein samples at the final points of aggregation.

Figure supplement 2. Effect of membrane curvature on binding and aggregation.

Figure supplement 3. Effect of membrane composition on binding and aggregation.

Numerous smaller vesicles are observed in the background that suggest a possible vesiculation of the GU induced by H72F during the long incubation period (Figure 3—figure supplement 2c,d). Such vesiculation has also been reported earlier in some cases of other amyloid structures (Meker et al., 2018). These results suggested possible membrane remodeling induced by Zn-deficient H72F mutant, an aspect we would like to study in further detail. To determine the effect of

Table 4. Log-phase mid-points of different protein variants obtained from ThT assay.

Systems	Log-phase mid-point (h)
WT SOD1	Not detectable
WT SOD1 + DPPC SUV	Not detectable
H121F	Not detectable
H121F + DPPC SUV	Not detectable
H72F	167.2
H72F + DPPC SUV	90.8
apo SOD1	112.8
apo + DPPC SUV	55.9

membrane composition, we studied DPPG, which is a widely used negatively charged membrane with chain length identical to DPPC. Interestingly, our results showed that both binding and the rate of aggregation increased in the presence of a negatively charged membrane (*Figure 3—figure supplement 3*).

Aggregates of apo and H72F variants that form in the presence of membrane show highest cellular toxicity and GUV deformation rates

We investigated the effect of the aggregates of different protein variants on cellular toxicity (by measuring cell viability) in general and on the cell membranes (using a number of spectroscopy and imaging assays) in particular. Cell viability was measured by the standard MTT assay. We used aggregates collected at the plateau region of the aggregation kinetics. MTT assay using SHSY5Y cell line showed minimum toxicity in terms of cell death for WT_{agg}, WT_{aggm}, H121F_{agg}, and H121F_{aggm} (*Figure 4—figure supplement 1*). In contrast, apo_{agg}, and H72F_{agg}, showed significantly higher neuronal dead cell population which increased further with apo_{aggm} and H72F_{aggm}, respectively. Although neuronal cell death is one of the decisive factors of aggregate toxicity, the severity of ALS has been found to depend on the extent of membrane perturbations, which may contribute to multiple events including (1) mitochondria-associated membrane (MAM) collapse and disruption (*Watanabe et al., 2016*), (2) the synaptic dysfunction due to impaired synaptic vesicles function toward neurotransmission (*Casas et al., 2016; Song, 2020*), and (3) the prion like spread of toxic aggregates between cells presumably through macropinocytosis (*Yerbury, 2016; McAlary et al., 2019*). Therefore, it is necessarily important to investigate in detail the protein aggregates induced membrane perturbation, which has never been addressed before. We used three different assays for the in vitro studies, viz. (1) phase-contrast microscopy using a membrane model of giant unilamellar vesicle (GUV) to probe how the presence of aggregates change their size and shapes, (2) a calcein release assay to probe aggregate-induced pore formation, and (3) FTIR to determine the molecular mechanism of the influence of different aggregates on the structure of lipids.

For the imaging assay, we used time based optical microscopic investigation to unveil how the addition of P_{agg}, and P_{aggm} affects the size and shape of GUVs. GUV is widely used as a model membrane system, providing free-standing bilayers unaffected by support-induced artifacts yet with sufficiently low curvature to well mimic cellular membranes and mitochondrial membrane as well. An advantage of this assay comes from the use of phase contrast without requiring any external fluorophore label. We made the GUVs composed of DOPC:DOPE:PI:DOPS:CL in the ratio 4.5:2.5:1:0.5:1.5, which mimics mitochondrial membrane composition (*Gohil and Greenberg, 2009*). *Figure 4a* is a representative example of how apo-aggregates formed in the absence of membrane (apo_{agg}) behaved with the GUVs. In contrast, *Figure 4b* shows the influence of the apo-aggregates formed in the presence of membrane (apo_{aggm}) (*Figure 4—figure supplement 2*). *Figure 4c* shows an example of a control, in which WT samples (WT_{agg}, which should contain minimum aggregates population) were added to the GUVs. GUV images of *Figure 4a,b* clearly demonstrate that the aggregates attach on the surface of GUVs (shown by arrows) leading to membrane deformation and change in lamellarity. These two images also show the pore formation, which was further established by the contrast loss. A comparison between *Figure 4a,b* shows visually that membrane deformation

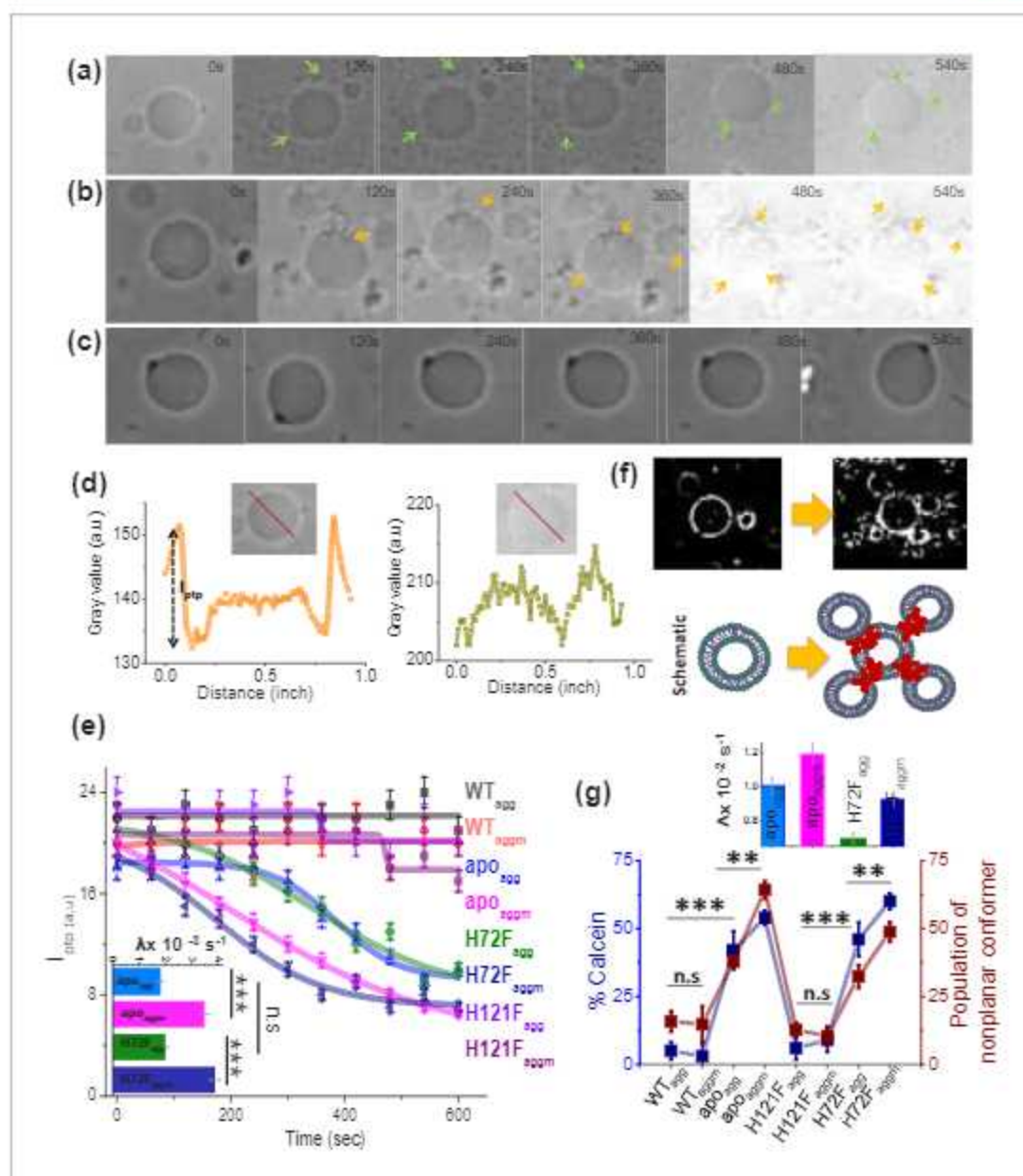


Figure 4. Membrane deformation by protein aggregates. Time variations of phase-contrast micrographs of a single GUV when GUVs were treated with (a) apo_{agg} , (b) apo_{aggm} , and (c) WT_{agg} . The images show gradual contrast loss, the loss of lamellarity and aggregate association with the vesicles for (a) and (b), while (c) does not show any change. (b) also shows few vesicles assemblies as induced by aggregates (also refer to a high contrast image below). The protein aggregates and their association with GUVs have been marked by green and yellow arrows. (d) The pictorial definition of I_{ptp} and how I_{ptp} changes for an intact (left) and porous (right) vesicle. (e) The values of I_{ptp} are plotted for different protein aggregates with time. The inset of this figure shows the rate of deformation (λ, s^{-1}) for $\text{apo}_{agg}/\text{apo}_{aggm}$ and $\text{H72F}_{agg}/\text{H72F}_{aggm}$. The typical sizes of the GUVs were $\sim 30 \mu\text{m}$. (f) High-contrast images of GUVs show vesicular assembly in the presence of apo_{aggm} , which is also schematically described in the figure below using a drawing. The schematic representation shows that apo_{aggm} can act as a connector between multiple GUVs. (g) Plot of calcein leakage percentage and the population of nonplanar rotamers (these rotamers arise at 1367 cm^{-1} vibrational frequency region of hydrocarbon lipid chains on treatment with different protein aggregates). Here, the subscripts agg and aggm stand for the aggregates of the respective protein species at the plateau region of the aggregation profiles, which were formed in the absence and presence of membrane (DPPC SUVs), respectively. The inset of this figure shows the rate of fluorescence growth (λ, s^{-1}) due to aggregate induced pore formation mediated calcein dye leakage from the SUVs that mimic synaptic vesicles (composition of lipid: DOPC:DOPE:DOPS in the ratio 2:5:3). Here, n.s. designates nonsignificant change, whereas ** stands for significant ($p\text{-value} < 0.01$) and *** for highly significant ($p\text{-value} < 0.001$). The error bars indicate the standard deviation of triplicate experimental data.

The online version of this article includes the following source data and figure supplement(s) for figure 4:

Source data 1. Toxicity of the aggregates .

Figure 4 continued on next page

Figure 4 continued

Figure supplement 1. MTT assay to detect the cell viability of neuronal cells (SHSY5Y) when treated with different aggregates of SOD1 protein variants.

Figure supplement 2. Time scale optical microscopic images of GUVs when these were treated with apo_{aggm}.

Figure supplement 3. High contrast images of the GUV when it was treated with apo_{agg}.

Figure supplement 4. Assembly of vesicles/GUV clustering when GUVs were treated with H72F_{aggm}.

Figure supplement 5. Change in I_{ptp} of a single GUV in presence of DPPC SUVs (10 μ M).

Figure supplement 6. Effect of aggregates on membrane deformation.

is more prominent (more damage) and faster (occurs at earlier time points) in the presence of P_{aggm}. All these changes in GUVs were found absent in Figure 4c, in which WT_{agg} was used. For the quantification of the image data, we determined the difference in refractive indices between the exterior and interior of GUVs (represented by I_{ptp} , peak-to-peak intensity in Figure 4d; Sannigrahi et al., 2019). In the case of intact vesicles, the values of I_{ptp} would be high (Figure 4d, left) due to the difference in sugar asymmetry between outside and inside of GUVs, which would disappear in the case of membrane deformation (Figure 4d, right). We plotted the time dependence of I_{ptp} to determine quantitatively the membrane deformation kinetics by measuring the deformation rate constants, λ (Figure 4e, inset). The GUV deformation was insignificant and no detectable kinetics were found for WT_{agg}, WT_{aggm}, H121F_{agg}, and H121F_{aggm} (Figure 4e). On the other hand, apo_{agg} and H72F_{agg} exhibited significantly high deformation rate ($\lambda_{apo_{agg}} \sim 1.8 \times 10^{-3} \text{ s}^{-1}$ and $\lambda_{H72F_{agg}} \sim 2.1 \times 10^{-3} \text{ s}^{-1}$) and both kinetics appeared cooperative (sigmoidal behavior, Figure 4e). It is interesting to note that in the presence of apo_{aggm} and H72F_{aggm}, the deformation rate increased significantly ($\lambda_{apo_{aggm}} \sim 3.5 \times 10^{-3} \text{ s}^{-1}$ and $\lambda_{H72F_{aggm}} \sim 3.9 \times 10^{-3} \text{ s}^{-1}$). More interestingly, both apo_{agg} and apo_{aggm} showed a tendency to create attachments between vesicles to generate vesicular assembly and co-operative deformations (high-contrast images in Figure 4f, which is also shown by a schematic drawing). The image analysis and visualization of the GUVs in presence of apo_{aggm} suggested that the co-operative vesicular clustering and deformation presumably occurred through allosteric communications mechanism by the aggregates (Figure 4—figure supplement 2). We found that apo_{aggm} and H72F_{aggm} are more efficient towards inducing vesicular assembly and deformations (Figure 4f, Figure 4—figure supplement 3, Figure 4—figure supplement 4). To rule out the effect of only SUVs (which are present along with the protein), we performed a control experiment by treating the GUVs with similar concentration of DPPC SUVs as employed for the formation of P_{aggm}. Our results showed insignificant changes in I_{ptp} values in the presence of DPPC SUVs (Figure 4—figure supplement 5), further highlighting that P_{agg} and P_{aggm} are responsible for the GUV perturbations.

Electron microscopic images of the synapses infused with ALS variants, like G85R, showed vacant active zones (AZs) and occasional abnormal membranous structures, whereas there occurred no reduction in the synaptic vesicles number in case of WT SOD1 (Song, 2020). Similar observation was found previously by Wang et al., 2009. Using *C. elegans* as model system, they showed that the neuronal toxicity in ALS appears due to synaptic dysfunction that occurs because of misfolded and aggregated disease mutant driven lowering in the number of organelles including synaptic vesicles and mitochondria. The pore formation and vesicle rupture by aggregates may be a possible reason for the reduced synaptic vesicle population in case of ALS disease mutants. To investigate this issue, we prepared calcein entrapped SUVs composed of DOPE, DOPS, and DOPC at the molar ratio 5:3:2 to mimic the synaptic vesicle composition and curvature (Fusco et al., 2016). In this assay, we measured the percentage of calcein leakage from the dye entrapped inside lipid vesicles (Figure 4g, Figure 4—figure supplement 6). The extent of calcein leakage after the treatment of different protein aggregates followed the trend similar to what was observed by GUV micrographic observation (Figure 4e), which suggested that the membrane rupture is facilitated in significantly higher rate and extent by apo_{aggm} and H72F_{aggm}, while compared with apo_{agg} and H72F_{agg}, respectively (Figure 4g, inset, Figure 4—figure supplement 6a).

In order to induce membrane deformation as observed by previous two assays, the aggregates need to inflict substantial changes in lipid structure. To determine the extent of conformational change the lipid molecules experience by protein variants, we used ATR-FTIR to measure quantitatively the populations of different rotamers in a general planar trans-oriented phospholipid bilayer of

DPPC. CH₂ wagging band frequency (1280–1460 cm⁻¹) of the hydrocarbon tail region of the bilayer was carefully monitored for this purpose (Lewis and McElhaney, 2013; Maroncelli et al., 1982). The results show a significant increase in the populations of nonplanar kink+gtg' rotamers (this band appears at 1367 cm⁻¹) when planar lipid bilayer was treated with apo_{agg}/apo_{aggm} and H72F_{agg}/H72F_{aggm} (Figure 4g; Figure 4—figure supplement 6b,c). We also found that apo_{aggm}/H72F_{aggm} exerted greater effect on lipids than apo_{agg}/H72F_{agg}. Interestingly, differences in the populations of non-planar conformers are found to be similar to the variation in the extent of calcein release induced by protein variants (Figure 4g). This observation provides preliminary evidence that both events occur by similar trigger (presumably the membrane attachment by the aggregates).

Aggregation kinetics and aggregate-induced toxicity studies of ALS disease mutants

In the previous few sections using WT, apo, H121F, and H72F, we established that the WT (containing both Zn and Cu) and the Zn bound H121F protein did not aggregate or induced toxicity through membrane deformation. In contrast, the removal of either Zn (H72F mutant) or both metals (the apo protein) resulted in strong membrane association, aggregation and induction of cellular toxicity. The data clearly suggest that Cu plays secondary roles in aggregation induced toxicity, while Zn pocket destabilization acts in concert with membrane-induced conformational change resulting in aggregation and toxic gain of function. Since these experiments validate successfully the predictions from the statistical mechanical model, we subsequently wanted to understand this behavior could be generalized in ALS disease mutants.

For this purpose, we used both in silico and experimental approaches. For the in silico method, we selected fifteen disease mutants of ALS, whose structures are available in the protein data bank (PDB) (Table 5). From the crystal structures, we determined the distance between the mutation site and Zn (and Cu) for all these disease mutants. In addition, we calculated the transfer free energies, that is the theoretical membrane association energies (ΔG_{Tr}), of these mutants using the OPM server. We found that the negative values of ΔG_{Tr} decreased linearly with the increased distance of Zn site for these mutants, while it remained non-variant with the distance of Cu site (Figure 5a). We also found that the severity of ALS mutants (defined here as the survival time in year of ALS patients after

Table 5. SOD1 disease mutants, their corresponding distance parameters in terms of the distances of mutational stress points from the Zn and Cu center, and the membrane binding energies of the disease mutants.

Mutants	Mutational points distances from zn center (Å)	Mutational points distances from Cu Center (Å)	Membrane binding energies (ΔG , kcal/mole)
AMV	19.6	19.3	-1.6
C6A	17	15.7	-2.1
G37R	23.7	17.2	-1.0
L38V	22.2	13.6	-1.2
H43R	17.8	9.9	-1.0
H46R	7.8	10.2	-2.3
H80R	4.2	10.3	-2.3
G85R	8.6	8.4	-2.0
G93A	20.5	22.7	-1.8
C111A	11.9	18.3	-3.3
C112S	19.7	17.6	-1.3
I113T	16	18.5	-3.2
D124V	9	13	-2.1
H72F	2.9	8.2	-3.1
H121F	14.4	5.6	-1.9
S134N	9.6	10.9	-1.6
C147S	16.3	10.3	-1.7

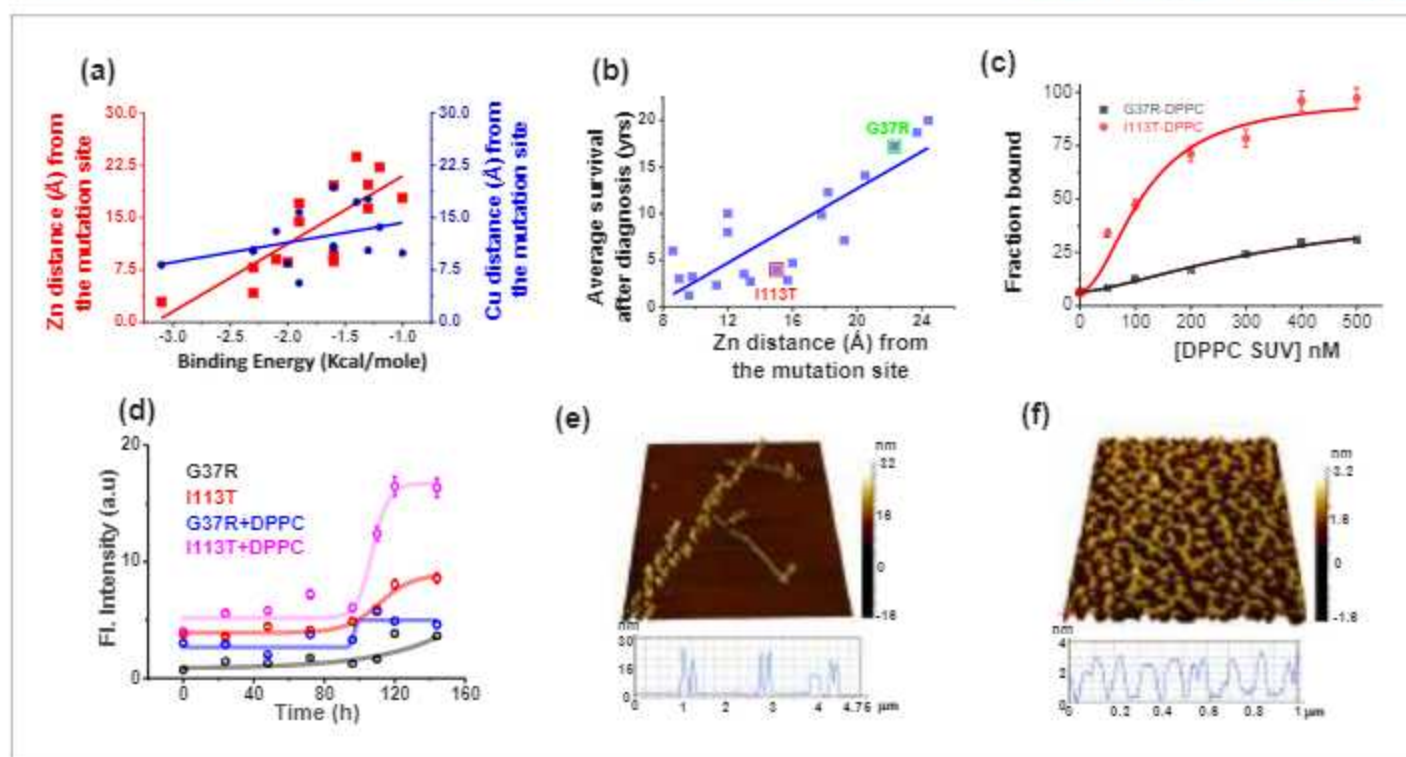


Figure 5. Validation in ALS disease mutants. (a) Computational validation. The distances of the disease mutation sites from the Zn (red) and Cu (blue) co-factor were plotted against the binding energy towards membrane, which were computed. The binding energy decreased linearly as the distance between Zn and mutation site increased (red curve), while there was no significant change for Cu (blue curve). The distance information for these mutants was calculated from their solved structures. (b) The ALS disease severity in terms of average survival time after diagnosis has been plotted against the distance parameters of the mutation points from Zn centre for the disease mutants. (c) percentage populations of membrane bound alexa-labeled protein variants which were obtained from the two component diffusion model fitting of the FCS data for G37R and I113T were plotted against the concentrations of DPPC SUVs added to evaluate the binding affinities of the protein variants towards membranes. (d) FRET fluorescence spectra of G37R and I113T were plotted in the absence and presence of DPPC SUVs. The 3D AFM images of I113T in absence (e) and presence (f) of membranes. Error bar indicates the standard deviation for the triplicate experiments.

The online version of this article includes the following source data and figure supplement(s) for figure 5:

Source data 1. Conformational characterization, membrane binding, aggregation and toxicity of ALS disease mutants.

Figure supplement 1. Conformational changes in disease mutants.

Figure supplement 2. Effect of point mutations (here disease mutations) of the proteins flexibility, conformational stability and dynamics as predicted using DynaMut webserver (<http://biosig.unimelb.edu.au/dynamut/>).

Figure supplement 3. Aggregate morphology of G37R mutant.

Figure supplement 4. MTT assay to detect the cell viability of neuronal cells (SHSY5Y) when treated with different aggregates of SOD1 disease mutants.

Figure supplement 5. Effect of disease mutant aggregates on membrane deformation.

Figure supplement 6. Comparative study of membrane binding and aggregation of different disease mutants.

diagnosis) correlates nicely with the distance of the Zn sites (Figure 5b; Wang et al., 2008). For the experimental validation, we used two representative ALS disease mutants of varying distance between the mutation site and Zn. The mutations, namely G37R (mutation site-Zn distance 24 Å, less severe) and I113T (mutation site-Zn distance 16 Å, more severe) (Figure 5b) are well studied in literature (Milardi et al., 2010; Krishnan et al., 2006; Banci et al., 2009). Using FCS we also measured the K_d values of these two disease mutants which showed greater binding affinity for I113T (Figure 5c, Table 3). Structural characterization using FTIR showed greater extent of alpha helical content in I113T compared to G37R. On the other hand, further increase in the alpha helical structure in I113T was observed on interaction with model membrane. In contrast, we did not observe any membrane induced structural change for G37R (Figure 5—figure supplement 1). To understand the internal structural changes due to the disease mutations, we performed some in silico study using DynaMut webserver (<http://biosig.unimelb.edu.au/dynamut/>) to predict the effects of

mutational stress on the conformational dynamics, stability and flexibility of protein (Rodrigues *et al.*, 2018). The results suggested that G37R mutation increased the rigidity of different regions (6–16, 30–42, 80–86 aa) of the protein, whereas significant increase in flexibility of the loop IV and VII region (48–52, 130–150) was observed in case of I113T mutation (Figure 5—figure supplement 2). The predicted changes in folding free energy ($\Delta\Delta G$, kcal/mol) for I113T was found to be much more negative than G37R ($\Delta\Delta G(\Delta G_{WT} - \Delta G_{mutant})$) suggesting that mutation at 113th position destabilized the protein more in comparison to 37th position (Figure 5—figure supplement 2). The vibrational entropy change ($\Delta\Delta S$) in I113T was found to be $+0.188 \text{ kcal mol}^{-1} \text{ K}^{-1}$ while $-0.404 \text{ kcal mol}^{-1} \text{ K}^{-1}$ was found for G37R indicating the increase in flexibility for I113T and decrease in flexibility for G37R (Figure 5—figure supplement 2). Thus the increase in alpha helical content in I113T mutant arises due to the increase in flexibility in the membrane interacting loop regions as suggested by the DynaMut server. Subsequently, we used ThT fluorescence to probe the aggregation kinetics of G37R and I113T in the absence and presence of DPPC SUVs. Results in the absence of membrane showed significantly higher aggregation for I113T when compared to G37R. A notable increase in the rate and extent of aggregation was observed for I113T under membrane environment, whereas for G37R, the change was not significant (Figure 5d). AFM imaging showed linear fibrillar aggregate for I113T in the absence of membrane (average length is $\sim 1.5 \mu\text{m}$ and height is 26 nm), whereas fibrillar network was observed when aggregation occurred in the presence of DPPC SUVs (average height is 3.2 nm) (Figure 5e,f). In contrast, small nonfibrillar aggregates were found for G37R mutant both in the absence and in the presence of membranes (Figure 5—figure supplement 3). Finally, we studied the toxic effects of the aggregates of G37R and I113T, which formed in the absence and presence of membrane. Using MTT, we showed that I113T aggregates in the absence of membrane were less toxic than I113T aggregates in the presence of membrane (Figure 5—figure supplement 4). G37R exhibited minimal toxicity both in the absence or presence of membrane (Figure 5—figure supplement 4). We observed for these mutants a nice correlation between the extent of calcein release and the populations of nonplanar kink+gtg' conformers (Figure 5—figure supplement 5).

For further validation, we studied the membrane association and aggregation of a third disease mutant G85R. Earlier reports suggested that the survival time for G85R (6 years) remains between G37R (17 years) and I113T (4.3 years) (Wang *et al.*, 2008). Our computational and experimental binding study using FCS (Figure 5—figure supplement 6) showed that the binding affinity of G85R (-2 kcal mol^{-1}) is intermediate between that of G37R (-1 kcal mol^{-1}) and I113T ($-3.2 \text{ kcal mol}^{-1}$). In addition, AFM imaging (Figure 5—figure supplement 6) suggests that G85R aggregation behavior in membrane environment remains between mild G37R and severe I113T mutants.

Discussion

The cofactor-derived membrane association model

In this work, we effectively bring a large number of studies together in a coherent framework to address the different roles of two metal cofactors (Cu and Zn) and membrane binding on the aggregation and induced toxicity of SOD1. Based on steady-state fluorescence, acrylamide quenching, and FT-IR data, the investigated proteins could be classified as (1) WT and WT-like mutant, H121F and (2) apo and apo like mutant, H72F. The battery of experimental approaches clearly validates the prediction from the bWSME model that Zn is largely responsible for the conformational stability of SOD1. The insertion of Zn at the loop IV region stabilizes the loop while reducing the aggregation propensity of the apo protein. We believe that the stabilization of this long loop may play an important role in SOD1 aggregation biology and its relevance in ALS. It may be noted that shortening of the loop has been shown to increase the stability of the protein (Yang *et al.*, 2018). This is also important to point out that SOD1 variants from thermophiles (like SOD5 from *C. albicans* SOD5) have shorter electrostatic loops compared to human SOD1 (Gleason *et al.*, 2014).

In contrast, the absence of Cu does not seem to have any significant effect on the stability of the protein, and the Zn containing Cu-deficient protein behaves like WT. We derive a possible maturation/aggregation landscape of SOD1 in the presence of membrane employing data from the current work and available literature (Figure 6). Since all experiments presented here were carried out using the reduced protein, this scheme does not take dimerization into consideration. SOD1 in its metal

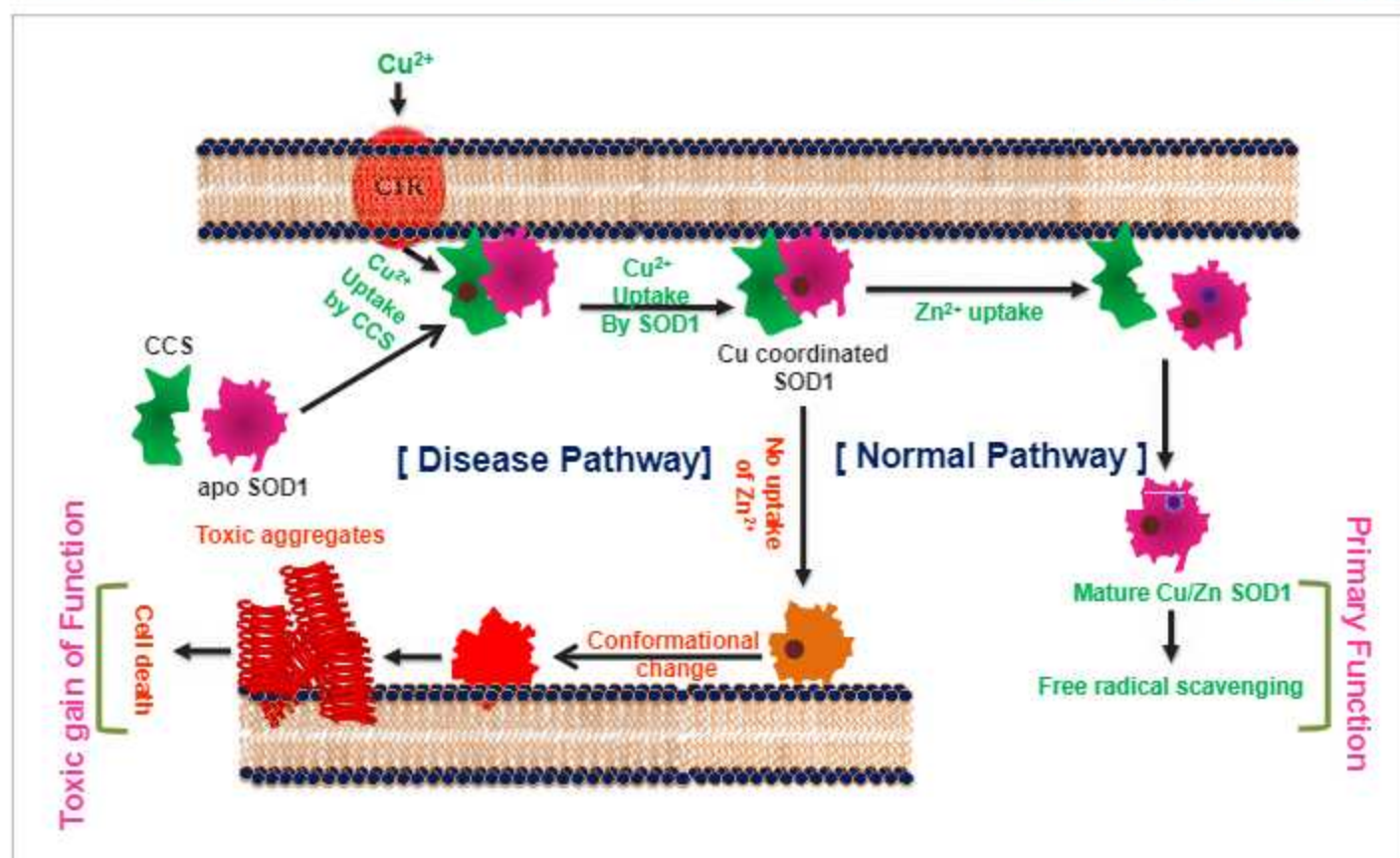


Figure 6. The cofactor-derived membrane association model of SOD1 primary and gain of function.

free state (apo protein) has been shown to be flexible and inherently dynamic. The sequence sites (48–80 and 120–140) of low folding probability predicted by bWSME calculation (Figure 1b) have significant overlap with the sequence sites (45–70 and 125–142) of high membrane binding as calculated by OPM (Figure 2e). It has been found that truncation at Leu126 of C-terminus resulted in a protein with several transmembrane helices (Lim et al., 2015). We found that the apo protein has high membrane binding possibility which is directly supported by membrane binding data (Figure 2i, Figure 2—figure supplement 7b,c). Membrane bound apoSOD1 with an optimized orientation is a requisite for the Cu insertion to take place. Since biological systems have very-low-free Cu salt (Rae et al., 1999), Cu coordination to SOD1 occurs through Cu chaperone protein (CCS) which transfers Cu to apo SOD1 using membrane as a scaffold (Pope et al., 2013). Membrane scaffolding decreases the directionality of metal transport compared to a three-dimensional search of the metal ions. The domain I of CCS binds Cu through two cysteine residues. Since Cu binding affinity of CCS is less than that of SOD1 (which recruits three or four cysteine residues), Cu transport occurs from CCS to SOD1, and not the other way (Banci et al., 2010). Zn binding, which occurs in the next step, stabilizes the loop regions. This event has a few important consequences. First, it has been shown that both CCS and SOD1 exhibit binding to Zn (Proescher, 2008). While the absence of Zn favors heterodimer formation with SOD1 (CCS-SOD1), the presence of Zn facilitates the homodimer (CCS-CCS) configuration. Second, as shown in this paper, Zn coordinated protein has little or minimum membrane binding and hence Zn bound SOD1 is removed from bi-layer. The third consequence comes from the reduced Zn affinity (which may come from a Zn compromised mutation or other reason for the sporadic forms of the disease), which would result in a misfolded membrane bound protein that is aggregation prone and potentially toxic.

As evident, the proposed scheme is somewhat Zn centric in which Cu coordination plays minimum role in the aggregation centric disease process. Partial support of this comes directly from the presented data of the distance dependence between ALS mutations sites and Cu. Also, the mutant

proteins without Cu (but with Zn site coordinated, e.g. H121F or G37R) do not show aggregation, neither they induce toxicity as studied by our assay systems. Earlier works have also shown that Cu binding has no effect on SOD1 folding (Bruns and Kopito, 2007). More importantly, it has been shown that CCS knock-out does not affect the onset of the disease or the life span in SOD1 transgenic mice (Subramaniam et al., 2002).

It may be important to consider that, although more than 140 SOD1 mutants are known in ALS, the disease is predominantly sporadic. Nevertheless, the disease initiation may still be done by a metal free apo (or Zn free) configuration, which can be generated from the WT protein as a result of a different trigger (and not by a genetic factor). The results obtained from two ALS mutants (I113T and G37R) can be discussed in this context. The present data show that I113T is similar to a zinc deficient protein, with high affinity toward membrane and higher aggregation propensity. In contrast, G37R behaves more like a WT protein. A comparison between the disease phenotype show that I113T is the second most common ALS mutant with average survival of 4.3 years, while for G37R, the average survival increases to 17 years. These results are in excellent correlation with the presented scheme.

Another interesting correlation of the presented scheme comes from a result that Zn supplement with a moderate dose of $60 \text{ mg kg}^{-1} \text{ day}^{-1}$ can increase the days of survival in a transgenic mouse experiment (Ermilova et al., 2005). Another approach could be using small molecules which would compete with the metal free protein towards membrane binding, an approach used recently in a Parkinson's disease model (Fonseca-Ornelas et al., 2014). While any drug development initiative targeting ALS and other neurodegenerative diseases suffer from the complications of diseases heterogeneity, poorly understood molecular mechanism and complex delivery avenues, a collaborative and integrative effort involving science and clinic, may be needed to find a successful solution.

The membrane connection

The molecular mechanism associated with ALS induced toxicity has been extensively studied and widely debated (Broom, 2012). SOD1 aggregates have been found in ALS patient samples (Gruzman et al., 2007; Guareschi et al., 2012). Mutant SOD1 aggregates have been shown to transfer from cell to cell using a prion like propagation mechanism (Münch et al., 2011). It has also been shown that the aggregation induced toxicity of SOD1 variants can occur through its attachment on mitochondrial membrane surface in transgenic ALS mice (Zhai et al., 2009). In parallel, pore formation at the membrane and abnormal ion mobility have been found with SOD1 aggregation (Ray et al., 2004). Although the above reports directly link a membrane connection with SOD1 aggregation (and presumably with ALS)-unlike other neurodegenerative diseases like AD and PD, membrane-induced aggregation studies with SOD1 have been limited (Choi et al., 2011).

Shahmoradian and colleagues reported that the structure of Lewy bodies in Parkinson's disease consists of α -synuclein and lipid vesicle clusters instead of the long-assumed amyloid fibril core (Shahmoradian et al., 2019). Using correlative light and electron microscopy (CLEM), they show that the vast majority of Lewy bodies actually consist of clusters of various membranous compartments, instead of amyloid fibrils as previously assumed. Assembly of synaptic vesicles has been shown recently by Fusco et al., 2016 in which two different regions of a protein molecule can be used as a 'double anchor' to induce the assembly. We think three particular finding can be discussed in this connection. First, the presented membrane deformation assay using GUV clearly shows the formation of vesicles assemblies (Figure 4f) induced by apo_{aggm} and H72F_{aggm}. Second, for both protein variants, relatively small aggregates of the proteins (formed in the presence of the membrane) and not the large fibrillar network (formed in the absence of membrane), favored vesicles assemblies. Third, the smaller sized aggregates formed in the presence of membrane seemed to induce more toxicity than the fibrils (formed in the absence). From the above three considerations, it is easy to envision that the anchoring ability of the aggregates toward vesicles assembly would be more efficient for a small-sized aggregates when compared to a fibril. There is an increased interest in the role of the number and nature of membrane lipids in shaping the aggregation landscape of different proteins in neurodegenerative diseases. Given the prion-like propagation in these diseases, our work underscores how characterization of protein-lipid interactions could enhance our molecular understanding of cellular toxicity and enable the identification of therapeutic molecules to mitigate the damage.